AGU ADVANCING EARTH AND SPACE SCIENCE

Reviews of Geophysics®

COMMISSIONED MANUSCRIPT
10.1029/2021RG000753

Key Points:

- Chemical and isotopic compositions of igneous rocks are sensitive to crustal thickness and paleoelevation of magmatic arcs
- Composition-Moho depth correlation models in modern arcs and collisional belts help estimate crustal thickness of ancient orogens
- Mantle melting and crustal differentiation contribute to composition-Moho depth correlations in arc magmas

Supporting Information:

Supporting Information may be found in the online version of this article.

Correspondence to:

P. Luffi and M. N. Ducea,
peter.luffi@gmail.com;
ducea@arizona.edu

Citation:

Luffi, P., & Ducea, M. N. (2022). Chemical mohometry: Assessing crustal thickness of ancient orogens using geochemical and isotopic data. *Reviews of Geophysics*, *60*, e2021RG000753. https://doi.org/10.1029/2021RG000753

Received 30 DEC 2021
Accepted 11 MAY 2022

Author Contributions:

Conceptualization: M. N. Ducea
Data curation: P. Luffi
Formal analysis: P. Luffi, M. N. Ducea
Funding acquisition: M. N. Ducea
Investigation: P. Luffi
Methodology: M. N. Ducea
Project Administration: M. N. Ducea
Software: P. Luffi
Supervision: M. N. Ducea
Validation: P. Luffi, M. N. Ducea
Writing – original draft: P. Luffi, M. N. Ducea

Chemical Mohometry: Assessing Crustal Thickness of Ancient Orogens Using Geochemical and Isotopic Data

P. Luffi[1,2] **and M. N. Ducea**[3,4]

[1]Sabba Stefanescu Institute of Geodynamics, Bucharest, Romania, [2]Geological Institute of Romania, Bucharest, Romania, [3]Faculty of Geology and Geophysics, University of Bucharest, Bucharest, Romania, [4]Department of Geosciences, University of Arizona, Tucson, AZ, USA

Abstract Convergent plate boundaries are key sites for continental crustal formation and recycling. Quantifying the evolution of crustal thickness and paleoelevation along ancient convergent margins represents a major goal in orogenic system analyses. Chemical and in some cases isotopic compositions of igneous rocks formed in modern supra-subduction arcs and collisional belts are sensitive to Moho depths at the location of magmatism, implying that igneous suites from fossil orogens carry information about crustal thickness from the time they formed. Several whole-rock chemical parameters correlate with crustal thickness, some of which were calibrated to serve as "mohometers," that is, quantitative proxies of paleo-Moho depths. Based on mineral-melt partition coefficients, this concept has been extended to detrital zircons, such that combined chemical and geochronological information extracted from these minerals allows us to reconstruct the crustal thickness evolution using the detrital archive. We discuss here the mohometric potential of a variety of chemical and isotopic parameters and show that their combined usage improves paleocrustal thickness estimates. Using a MATLAB® app developed for the underlying computations, we present examples from the modern and the deeper time geologic record to illustrate the promises and pitfalls of the technique. Since arcs are in isostatic equilibrium, mohometers are useful in reconstructing orogenic paleoelevation as well. Our analysis suggests that many global-scale correlations between magma composition and crustal thickness used in mohometry originate in the sub-arc mantle; additional effects resulting from intracrustal igneous differentiation depend on the compatible or incompatible behavior of the involved parameters.

Plain Language Summary Understanding how continental crust formed and evolved is one of the major goals of geology. Chemical composition of igneous rocks formed at modern convergent plate margins correlates with crustal thickness and elevation at the time of magmatism. Therefore, when averaged over local and regional scales, a series of chemical parameters act as excellent tracers of crustal thickness. These parameters or parameterscan in turn be used on ancient igneous rocks in order to determine crustal thickness and elevation of mountain ranges during magmatism; they are referred to as chemical mohometers and paleo-altimeters. Here, we review several proposed parameters and recommend new ones. We provide a MATLAB® app that ingests a variety of geochemical parameters and calculate paleocrustal thickness and elevation of diverse possible geologic applications.

1. Introduction

Present-day thickness of the continental crust, one of the most distinctive geochemical reservoirs that is unique to the Earth among rocky planets, is relatively well known at regional and global scales and ranges from just a few kilometers thicker than the oceanic crust (~6–8 km) to over 80 km in orogenic regions (Figure 1). Measured between the surface and the crust-mantle transition known as the Mohorovicic discontinuity or "Moho" (Mohorovičić, 1910), the thickness of crust, such as its composition, is intimately linked to mountain building processes and the distribution of magmatic and metamorphic rocks at depth at convergent plate margins and influences the stability and evolution of continents, climate, and life on our planet. It is therefore not surprising that one of the most important parameters that needs to be quantified is the thickness of orogenic crust. Yet, due to substantial modifications owed to various post-orogenic processes and erosion, the paleocrustal thickness of ancient orogens is difficult to determine. As orogens age and stabilize, their thicknesses converge to ~40–43 km as commonly seen in Precambrian and Paleozoic shields and platforms (Mooney, 2015).

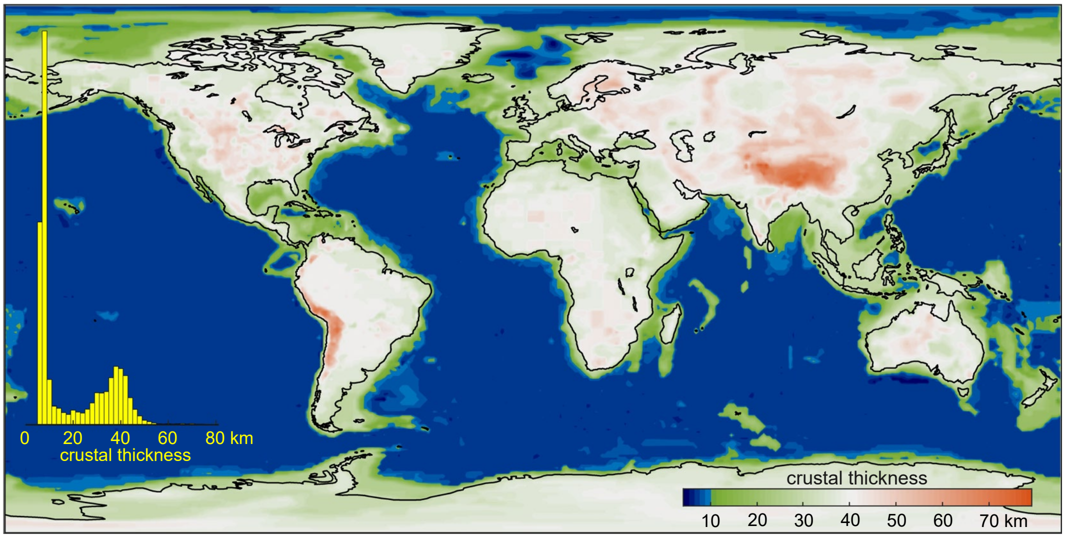

Figure 1. Present-day crustal thickness map of Earth based on the CRUST 1.0 model (Laske et al., 2013). Inset histogram shows the relative areal proportions of crustal thicknesses.

It has been long suggested that the chemistry of magmatic arcs—the distinctive features of convergent margins and fundamental building blocks of continents (e.g., Stern, 2002; Taylor & McLennan, 1985)—may be influenced by the thickness of the underlying crust. Certain major and trace elements, their ratios, as well as isotopic ratios have long been found to correlate with crustal thickness in arcs at regional and global scales (e.g., Coulon & Thorpe, 1981; Hildreth & Moorbath, 1988; Leeman, 1983; Plank & Langmuir, 1988). For decades, the interest in such correlations was largely motivated by their relevance to understanding arc magma generation and differentiation. Back when these ideas were put forward, the global inventory of geochemical analyses was limited, unevenly distributed, and required considerable efforts to be gathered. Quantifying correlations between some chemical parameters and crustal thickness in modern arcs and then using these as proxies to constrain the thickness of ancient orogens were not developed until relatively recently (Mantle & Collins, 2008), when it found crucial support in online geochemical databases aggregating tens of thousands of analyses from around the world, such as EarthChem (http://portal.earthchem.org) and GEOROC (http://georoc.mpch-mainz.gwdg.de). Today, large linkable geochemical and geophysical databases exist and are ready to be used.

What sort of crustal thickness proxies were identified and quantified owing to these unprecedented opportunities? How did these findings influence our thinking over the past decades about composition–crustal thickness correlations in arcs? Can we formulate new, better proxies? What types of data are the most appropriate and how can we maximize their utility? Are globally validated correlations useful to estimate crustal thickness at regional or even smaller scales? Can we test tectonic models of continental evolution using large geochemical data sets archived in rocks or minerals? In this review, we discuss recently proposed as well as new chemical and isotopic proxies for crustal thickness, hereafter coined “chemical Moho parameters” or “chemical mohometers,” at a time when the number of studies published on the topic has been growing significantly. We discuss various applications at whole-rock and mineral scales of investigation and explore their promises and limitations. Mineral-scale investigations represent a new avenue in mohometry and promise to reveal changes in crustal composition and thickness as well as evolutionary processes in the earlier Earth, provided that detrital phases, zircon in particular, of old age are the most common (and in the case of Hadean, exclusive) preserved archive. Some mohometers are thought to be sensitive to intracrustal differentiation processes (melt–crystal segregation and assimilation of local basement); others are argued to record mantle melting regimes and thus only indirectly constrain crustal thickness; intriguingly, it has been shown that the two processes tend to work in sync on whole-rock chemistry (Turner & Langmuir, 2015a). We will evaluate the contribution of mantle and crustal processes to the correlations observed between the composition of igneous rocks and the thickness of arc crust from a novel perspective.

2. The Moho Discontinuity

Crustal thickness is relatively easy to determine where a sharp Moho is marked by an abrupt jump of P-seismic wave velocities from typically less than 7 km/s in the crust to 7.6–8.1 km/s in the mantle (e.g., James & Steinhart, 1966; Mooney, 2015). A different definition of crustal thickness is sometimes given by the depth to the "petrologic Moho" (Griffin & O'Reilly, 1987), which is referred to as the transition between olivine-poor lithologies (including felsic and mafic rocks, as well as ultramafic cumulates dominated by pyroxenes, garnet, amphibole, or a combination of them) and mantle peridotites. In areas where the seismic Moho is sharp, it tends to coincide with the petrologic Moho. Hereafter, we refer to Moho as the seismically defined boundary between crust and mantle unless we explicitly refer to its petrologic or seismic definition.

The Moho is a much more elusive feature in overriding plates of subduction systems where transitions from lower crust to upper mantle velocities can be diffused and take place over large depth ranges (Beck et al., 1996; González-Vidal et al., 2018; Koch et al., 2021) or even be subject of duplication due to shortening-related faulting (A. D. Chapman et al., 2015). Resolving Moho depth may be particularly problematic in orogenic areas with the thick continental crust, such as the modern Central Andes both under the magmatic arcs and under the thick plateaus (e.g., Altiplano-Puna), that forms in some cases on the rear side of the arcs. Yuan et al. (2002) showed that Moho can range from 35 to over 80 km deep in nearby areas of the Central Andes although in detail several surfaces can be identified as potential Moho discontinuities (Assumpção et al., 2013). The petrology of lower crustal domains under magmatic arcs is such that sizable masses of residual/cumulate pyroxenites are both required by models (Bowman et al., 2021) and observed in the few areas where old lower crustal sub-arc domains are exposed at the surface (Kidder et al., 2003; Walker et al., 2015) as well as in the xenolith record (Ducea & Saleeby, 1998). These pyroxenites, with or without amphibole, garnet, magnetite/ilmenite, or plagioclase, cover a range of seismic velocities that can straddle the boundary between lower crust and upper mantle from granulite to arclogite (Ducea et al., 2021 and references therein). To complicate the issue even more, sub-arc domains are likely to contain partial melt in the crust and lithospheric mantle at different depths (Delph et al., 2017; McGlashan et al., 2008; Ward et al., 2017), rendering most seismic interpretations below these partially molten domains difficult. It is likely that in such environments, the seismic and petrologic Moho differ by several or tens of kilometers (Saleeby et al., 2003). In other words, the presence of dense arc cumulates that are crustal from a petrologic perspective but have mantle-like seismic velocities makes the seismic Moho potentially much shallower than the petrologic Moho beneath active arc regions. Conversely, the presence of melt in the uppermost mantle might make the seismic Moho appear deeper and less clear. There is currently no established relationship between crustal thickness and offset between seismic and petrologic Moho in arcs. Foundering of arc roots over time, while the arc is active (Jull & Kelemen, 2001) or after its demise (Ducea & Saleeby, 1998), makes it such that arc crust transitions to a sharper and shallower Moho after their activity terminates.

A different way to estimate Moho depths in arc regions is to evaluate gravity signals, which are highly model dependent and need to be constrained by local seismic data in order to minimize uncertainties where possible (e.g., Tassara & Echaurren, 2012). Bouguer gravity anomalies along the volcanic front of the Andean arc correlate with the average elevation of arc volcanoes (e.g., Hildreth & Moorbath, 1988). Thus, while it is difficult to provide a better estimate of the depth to Moho with gravity data, given the uncertainties in density and thermal structure of the magmatic arc crust, they suggest that most active arcs are in isostatic equilibrium. This justifies using elevation as a proxy for crustal thickness in arc regions, especially because geochemistry also correlates well with the elevation in arcs (Farner & Lee, 2017).

While most recent studies investigating connections between composition and crustal thickness of arcs rely on CRUST 1.0, a $1° \times 1°$ resolution global-scale seismically constrained model (Laske et al., 2013), or its coarser-resolution predecessors ($2° \times 2°$ and before that, $5° \times 5°$ global Moho models, Bassin et al. (2000) and Mooney et al. (1998)), some have opted to work with local or regional crustal thickness estimates from various sources (Mantle & Collins, 2008; Turner & Langmuir, 2015a). Though in geophysical usage, including the abovementioned global models, Moho depth is typically referenced to sea level, many studies focusing on the connections between the composition and thickness of arcs use the terms "Moho depth" and "crustal thickness" interchangeably, implying either that the difference between the two is insignificant in most cases, given the uncertainties associated with the various geophysical models, or that depth to Moho is measured from the topographic surface. Since in thick orogenic areas, such as the Andes, there is a systematic difference of up to 10% between the two, in

10.1029/2021RG000753

the following, we strive to distinguish these terms whenever we refer to them quantitatively, that is, $H^{\mathrm{tot}} = H + h$, where H^{tot} is the crustal thickness, H is the Moho depth relative to sea level, and h is the elevation.

3. Thickness–Composition Relationships in Arcs—A Brief History of Observations and Interpretations

Chemical and isotopic proxies for geologic and/or tectonic processes at regional scales are not new. At global scales, chemical averages of igneous rocks have been found to be good tracers of various subduction parameters. Global trends typically imply that average chemical data are pooled for one arc or large arc segment and are then viewed against plate kinematic indicators, crustal thickness, or other tectonic parameters of interest. Since the early days of plate tectonics, it became clear that major element chemistry of arcs, their average silica content and calc-alkaline affinity in particular, varies with the thickness of the upper plate's crust (e.g., Miyashiro, 1974). To explain major component variations in arc magmas, such as K_2O, some invoked the depth to subducting slabs (e.g., Dickinson, 1975). In contrast, studies of Coulon and Thorpe (1981) and Leeman (1983) suggested that the crustal thickness of the overriding plate must have a globally important control on K_2O and K_2O/Na_2O in major segments of arcs (Figure 2).

These studies found evidence that other fundamental chemical characteristics of arcs, such as the mean SiO_2 as well as Sr isotopic ratios increase, while the FeO_t/MgO ratio ($FeO_t = FeO + 0.9Fe_2O_3$) decreases with crustal thickness (Figure 2). Coulon and Thorpe (1981) also showed that for the limited data at the time (both on global arc chemistry as well as "tectonic" elements, such as plate parameters or regional Moho depth), these chemical parameters do not correlate with convergence rate, depth to slab, mantle wedge thickness, etc.

On a shorter length scale, by investigating the main stratovolcanoes making up the volcanic front of the Andean Southern Volcanic Zone (SVZ), Hildreth and Moorbath (1988) found that a series of chemical components and their ratios of the dominantly intermediate (andesitic and dacitic) rocks covary with the thickness of crust. They showed that at constant $SiO_2 = 57.5$ wt%, some components, such as K_2O, Hf, Ba, Rb, Cs, and Th, as well as ratios Ce/Yb, Rb/Cs, and Hf/Lu, tend to increase, whereas FeO_t/MgO and Ba/La decline as crustal thickness increases along strike toward the north. In addition, they also established that Sr and Nd isotopic ratios, respectively, increase and decrease in the same direction. Similarly, positive correlations have been found between crustal thickness and La/Yb, La/Sm, and Sm/Yb in the Andes and elsewhere (Kay & Mahlburg-Kay, 1991; Mahlburg-Kay & Mpodozis, 2001; Mahlburg-Kay et al., 2005). In their 1988 paper, Hildreth and Moorbath proposed that all these trends mirror the depth of intracrustal differentiation near the Moho, which they defined as the melting, assimilation, storage, and homogenization (MASH) zone of arcs, where the composition of melts are largely influenced by the pressure-dependent nature of the separating residual mineral assemblages. This model, sometimes also referred to as the "crustal filter," was viewed as a natural consequence of the fact that the modification of mantle-derived melts, melting of lower crust, magma mixing, and assimilation are most efficient in the deepest and hottest zones of magmatic arcs (DePaolo, 1981; DePaolo et al., 1992; Dufek & Bergantz, 2005). In this view, igneous processes occurring at 20–60 km beneath the surface result in huge differences in magma diversification pathways. Therefore, the expectation that a series of geochemical parameters can map out crustal thicknesses is realistic.

Since its formulation, the model of Hildreth and Moorbath has served as a broadly accepted reference frame for explaining the behavior of various chemical parameters that are sensitive to Moho depth variations. As an example, Sr/Y has been suggested as an empirical qualitative pseudo-barometer of magmatic differentiation in intermediate to felsic rocks (e.g., Best et al., 2009; Lee et al., 2007; Tulloch et al., 2003), which are common in many arc igneous systems. This ratio has been used to loosely distinguish shallow versus deep fractionation processes due to pressure-dependent differences in the partitioning behavior of Sr and Y between various residual phases and melts with intermediate compositions. During partial melting of lower crustal gabbros or magmatic fractionation of mantle-derived mafic magmas, Sr is compatible at low pressures ($<\sim 10$ kbar) where it strongly partitions into plagioclase. However, at high pressures (>12 kbar), where plagioclase is unstable, Sr is incompatible and preferentially enters the liquid phase. Conversely, Y is incompatible at low pressures, but readily partitions into garnet and amphibole at high pressure. As a result, higher Sr/Y is taken to indicate greater average pressure, or crustal depth, at which igneous differentiation occurred (Paterson & Ducea, 2015). This inference is consistent

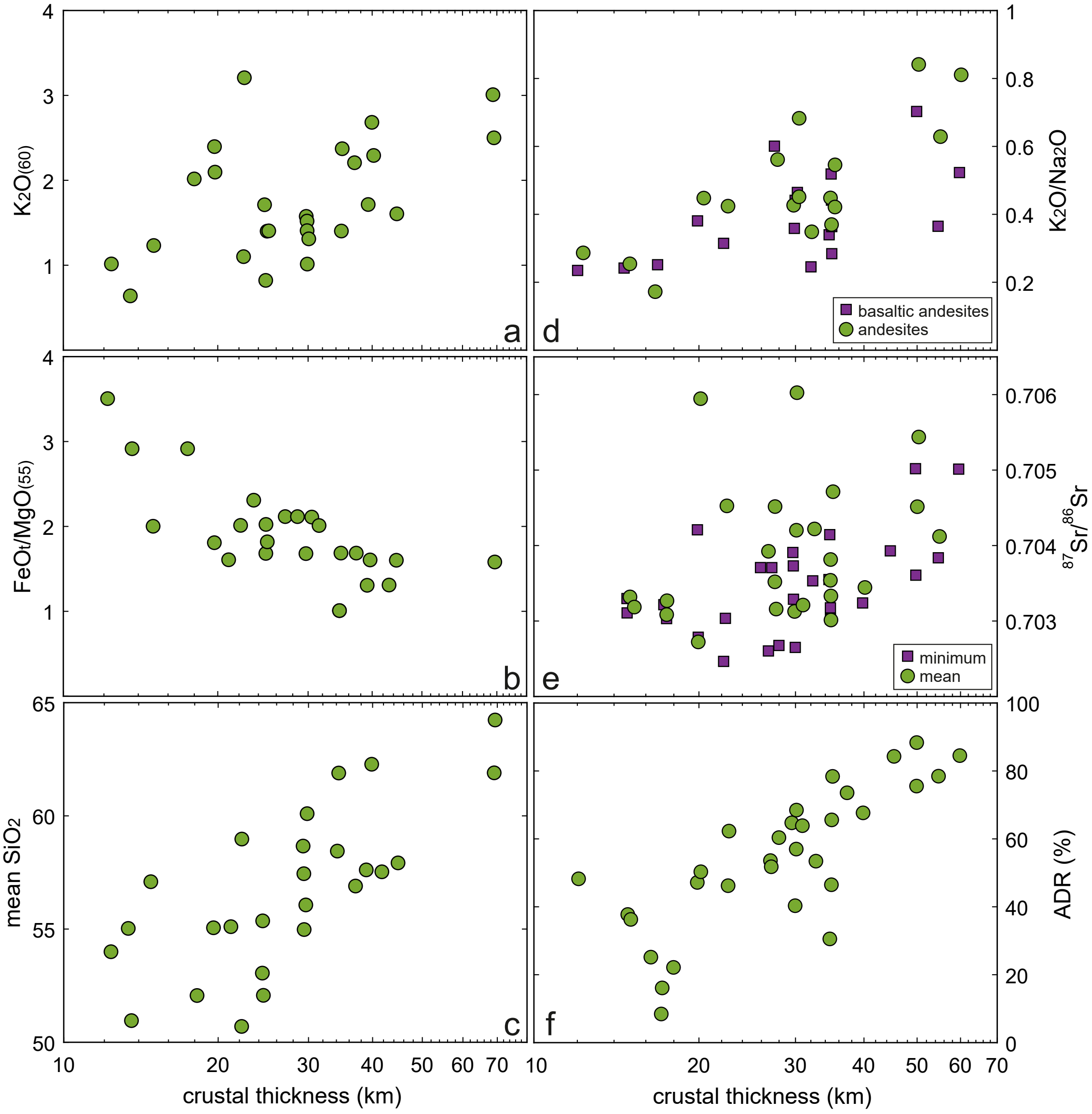

Figure 2. Correlations between crustal thickness and composition in arcs: (a–c) Coulon and Thorpe (1981); (d)–f) Leeman (1983); datapoints represent individual arc segments. Chemical parameters plotted against crustal thickness are (a) K_2O at 60 wt% SiO_2; (b) FeO_t/MgO at 55 wt% SiO_2; (c) mean SiO_2; (d) mean K_2O/Na_2O in basaltic andesites and andesites, respectively; (e) mean and minimum $^{87}Sr/^{86}Sr$; and (f) percent of ADR (andesite-dacite-rhyolite series rocks).

with the correlation observed between Sr/Y and Moho depth for intermediate compositions when averages of multiple arcs are compared (Chiaradia, 2015; J. B. Chapman et al., 2015; Profeta et al., 2015).

In a similar fashion, Chiaradia (2014) found that the behavior of Fe and Cu in differentiating arc magmas is controlled by the thickness of crust, suggesting that the rate of depletion or enrichment of these elements in the evolving liquids is modulated by the interplay between plagioclase, magnetite, and sulfide fractionation: thicker arcs tend to be depleted in Fe and Cu because they are dominated by deeper differentiation of more hydrous and oxidized melts, which hinder plagioclase crystallization but promote coupled magnetite and sulfide removal. By the same token, crustal thickness control on the behavior of Zn during arc magma differentiation was ascribed to modifications of the crystallizing assemblage at the bottom of crust from plagioclase-dominated cumulates in thin arcs to hornblende- and garnet-dominated cumulates in arcs built on thick crust (Chiaradia, 2021).

Plank and Langmuir (1988) found that major oxides CaO and Na_2O in arc basalts at 6 wt% MgO display strong correlations with crustal thickness (Figures 3a and 3b). In contrast with the above-outlined view focusing on

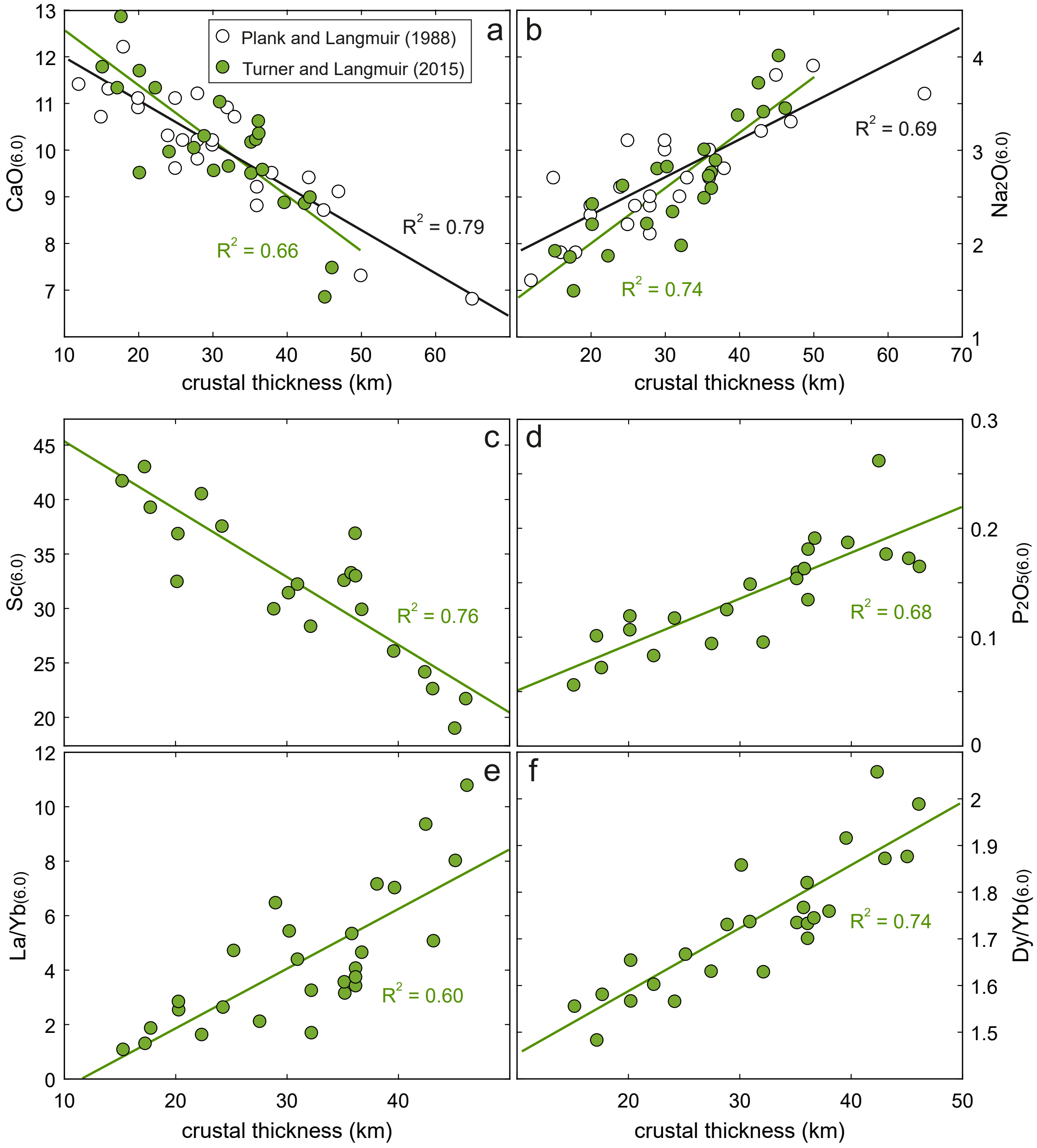

Figure 3. Correlations between crustal thickness and composition of arc basalts with 6 wt% MgO: (a and b) Plank and Langmuir (1988); (a–f) Turner and Langmuir (2015a). Datapoints represent individual arc segments. Chemical parameters compatible during mantle melting (CaO and Sc) correlate negatively, whereas those incompatible (Na_2O, P_2O_5, La/Yb, and Dy/Yb) correlate positively with crustal thickness. Note the different crustal thickness intervals evaluated in the two studies.

intermediate and felsic magmas, these authors argued that the crustal filter of MASH zones plays no significant role in shaping the composition of arc basalts; instead, in their view, the correlations observed in mafic magmas are largely inherited from their mantle source, being controlled by the extent of melting in the sub-arc wedge, which in turn is constrained in part by the thickness of the overriding plate. This view has been developed further and corroborated by a recent analysis of Turner and Langmuir (2015a, 2015b), which used a considerably larger set of global data including trace elemental chemistry as well. Focusing on arc basalts with MgO >4 wt% and on lithologies with 6 wt% MgO in particular, they found that similar to Na_2O, a variety of other incompatible chemical components and ratios (i.e., preferentially partitioning into the liquid phase), such as K_2O, P_2O_5, Sr, Ba, Ce, Zr, Dy/Yb, and La/Yb, correlate with crustal thickness, whereas compatible components (preferentially

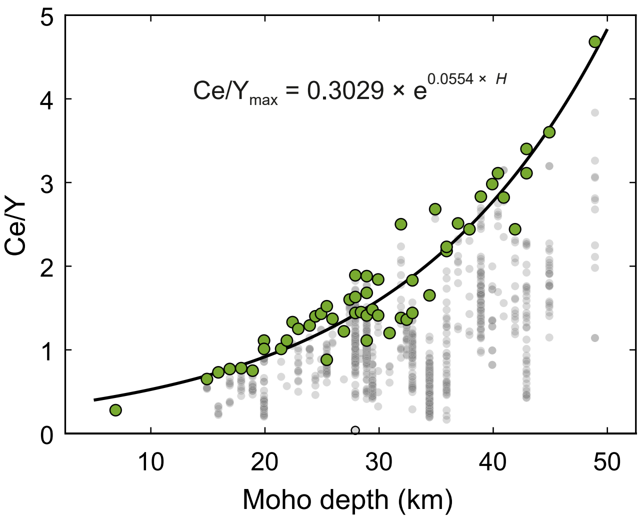

Figure 4. Ce/Y_{max} correlation with Moho depth (Mantle & Collins, 2008). Small gray symbols show the complete Moho depth-dependent Ce/Y variability in basalts with MgO >4 wt% from the examined volcanic suites. Regression was obtained using the maximum Ce/Y from each volcanic suite (large green symbols).

partitioning into minerals) CaO, Sc, and V display negative correlation with crustal thickness (representative examples shown in Figure 3). They argued that these global-scale covariations cannot be ascribed to commonly invoked intracrustal differentiation mechanisms, such as pressure-controlled fractional crystallization or magma mixing, but are readily explicable by magma generation processes in the mantle. Building on this concept, Turner et al. (2016) showed that the correlation between the composition of basalts erupted along the volcanic front of the Andean SVZ and Moho depth can be explained by variations in the melting degree of the underlying mantle wedge controlled by thermal structure, which changes with thickness of the overriding plate.

Basalts are underrepresented in most continental arcs and thus in most orogens, the chemical parameters evaluated by Turner and Langmuir have a limited potential as mohometers; however, the correlations they identified do suggest that the sensitivity of chemical parameters to crustal thickness variations even in more felsic melts of arc regions is not the consequence solely of the crustal filter but may be at least partly inherited from the mantle. That is, intracrustal differentiation can be expected to be the exclusive cause only of those composition–crustal thickness trends that are observable in evolved rocks, but largely absent in primitive ones. The possible contributions of mantle and crustal processes to different composition versus Moho depth correlations will be analyzed at the end of Section 5 of this paper.

4. Mohometers

4.1. Whole-Rock Mohometers

Mantle and Collins (2008) were the first to specifically calibrate a mohometer, that is, quantify a relationship between the composition of igneous rocks and Moho depth with the purpose of reconstructing paleocrustal thickness using geochemical data. Based on a survey of global volcanic data representing more than 50 volcanic suites, extracted from the modern GEOROC whole-rock database, they found that maximum Ce/Y ratios in arc basalts from active volcanoes strongly correlate with Moho depth (Figure 4) and can serve as mohometer:

$$H = 18.0505 \times \ln(\mathrm{Ce/Y_{max}}) + 21.5587, \qquad R^2 = 0.8979 \tag{1}$$

where H represents the Moho depths (km) beneath the involved volcanic centers relative to sea level as constrained by seismic refraction measurements. The estimated calibration error is ±3 km for the 95% confidence level. This formula was then used to reconstruct the paleocrustal thickness evolution of New Zealand, a part of eastern Gondwanaland throughout the Phanerozoic. To obtain meaningful Moho depth estimates, the recommended ratio to be used in Equation 1 is the maximum of at least 10 individual analyses of calc-alkaline basalts, assuming that they are not among the anomalously high-Ce/Y lithologies found in some areas where the lithospheric mantle is thought to be the source of arc basalts (e.g., the Aeolian arc). The New Zealand case study showed episodes of crustal thickening and thinning over the Phanerozoic consistent with regional geology. The most important limitation of this tool is that arc basalts are relatively rare in thicker continental arcs.

Chiaradia (2015) used data from 22 Pliocene-Quaternary arc segments extracted from GEOROC to show coherent global correlations between Sr/Y and crustal thickness, recognizing that specific correlations are influenced by differentiation as measured by MgO (wt%). Because of that, no direct correlation was quantified as it would depend on whether analyzed rocks are basaltic, intermediate, or silicic. A. D. Chapman et al. (2015), J. B. Chapman et al. (2015) and Profeta et al. (2015) calibrated an Sr/Y as well as a La/Yb mohometer using the same database as Chiaradia (2015) but zooming into an intermediate compositional window (55%–68% SiO_2) in order to provide expressions specific to volcanic rocks that dominate arcs. The resulting mohometric equations are:

$$H^{\mathrm{tot}} = 1.11 \times \mathrm{Sr/Y} + 8.05, \qquad R^2 = 0.90 \tag{2}$$

$$H^{\mathrm{tot}} = 21.277 \times \ln(1.0204 \times \mathrm{La/Yb_{(n)}}), \qquad R^2 = 0.72 \tag{3}$$

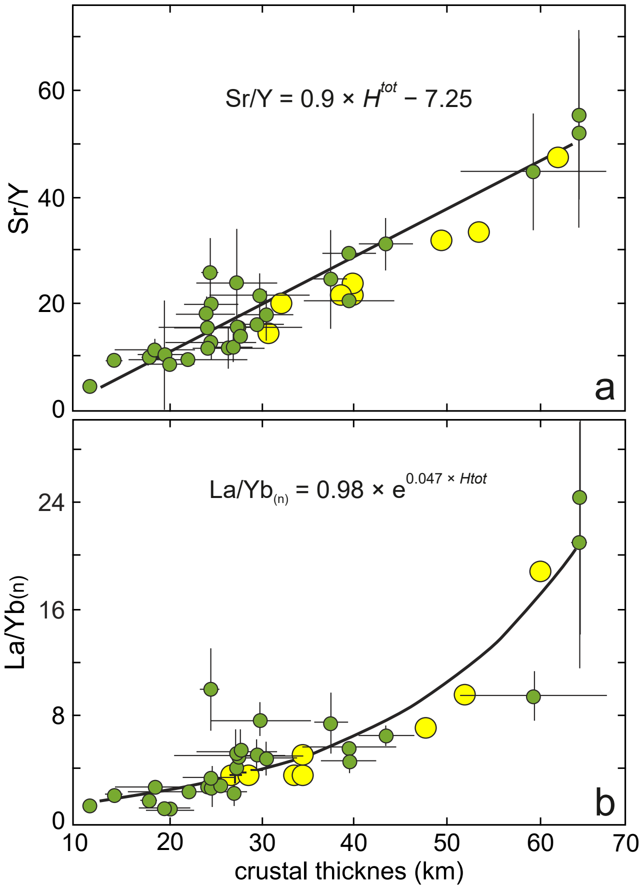

Figure 5. Correlations of (a) Sr/Y and (b) La/$Yb_{(n)}$ with crustal thickness (J. B. Chapman et al., 2015; Profeta et al., 2015). The regressions were obtained using median values calculated for individual arc segments (green symbols); error bars represent 1σ standard deviations. Crustal thicknesses attributed to the investigated arc segments mainly rely on the CRUST 1.0 (Laske et al., 2013) and CRUST 2.0 (Bassin et al., 2000) models, which were locally substituted by estimates obtained by various regional studies. Large yellow symbols represent individual stratovolcanoes from the Andean Southern Volcanic Zone, where large differences of crustal thickness occur over a relatively short distance along the strike of the arc (Hildreth & Moorbath, 1988). Their alignment with the global trend suggests that composition-crustal thickness correlations may be detectable within individual arc segments at lengthscales of tens to few hundreds of km.

where H^{tot} indicates crustal thickness, that is, depth to Moho measured from the topographic surface in km and subscript "(n)" for La/Yb indicates that the ratio is normalized to chondritic values. The resulting correlations (Figure 5) were performed on individual arc segments similar to Chiaradia (2015). The global and regional data sets produced similar trends lending credence to the application of this tool at the individual volcano (or intrusive suit equivalent) scale. This would be an average of some 30–50 km diameter footprint in the geologic record and an average duration of 3–8 Ma (Ducea, Paterson, et al., 2015), which are typical arc volcanoes time-space dimensions. There is some evidence that the Sr/Y and La/Yb ratios of arc volcanoes are rather similar to their intrusive equivalents as are the overall major elemental concentrations compositions in general (Ducea, Saleeby, et al., 2015; Keller et al., 2015). In a small fraction of samples (<1% of the evaluated population), Sr/Y and La/Yb are significantly higher and outside of the normal range commonly expected for igneous rocks based on mineral–melt partition coefficients (e.g., Sr/Y of 150–200 instead of the normal range of 10–50); such values cannot be used in mohometry and indicate unusual origin for those magmatic rocks (partial melts of subducting slabs, the presence of a carbonate component in the melt, etc.).

Lieu and Stern (2019) considered data for lavas from the modern central Andean volcanic arc, the arc of Central America, and the Aleutians-Alaskan arc to test the robustness of the Sr/Y and La/Yb mohometers when applied at smaller scales and in regions where crustal thickness is better known that the average global 1° × 1° seismic data of Laske et al. (2013). They concluded that statistically treated geochemistry-based proxies can provide useful constraints on crustal thickness when estimates from Sr/Y and La/Yb agree. The most likely proxy to diverge from geophysically constrained Moho depths in the analyzed regions is Sr/Y, in particular in regions of thin crust. An additional conclusion of that study is that care needs to be taken when dealing with the Moho in arc regions because the crust-mantle interface is dynamic due to episodes of delamination as well as additions of cumulates that are seismically mantle-like (see discussion in Section 2). All the complexities aside, these mohometers were validated in most places investigated.

Sundell et al. (2021) reassessed the Sr/Y and La/Yb mohometers of J. B. Chapman et al. (2015) and Profeta et al. (2015) and proposed an expression that combines the two via multiple linear regressions (Figure 6):

$$H^{\mathrm{tot}} = 19.6 \times \ln(\mathrm{Sr/Y}) - 24.0, \qquad R^2 = 0.811 \tag{4}$$

$$H^{\mathrm{tot}} = 17.0 \times \ln(\mathrm{La/Yb}) + 6.9, \qquad R^2 = 0.810 \tag{5}$$

$$H^{\mathrm{tot}} = 10.3 \times \ln(\mathrm{Sr/Y}) + 8.8 \times \ln(\mathrm{La/Yb}) - 10.6, \qquad R^2 = 0.892 \tag{6}$$

Uncertainties associated with the new models are ~11 km for Equations 4 and 5 and ~8 km for Equation 6 (95% confidence interval of the calibration residuals). Whereas Moho estimates produced with Equation 5 are within error undistinguishable from those obtained with the previous La/Yb model (Equation 3), predictions of the new Sr/Y formulation deviate from those produced by the linear expression of Equation 2, particularly at high Sr/Y values, for which the old calibration predicted excessively thick crust. The paired Sr/Y–La/Yb model was then used to unravel crustal thickness evolution of the eastern Gangdese Mountains in southern Tibet since the Jurassic. The advantage of this model is that it eliminates the discrepant estimates produced by the older Sr/Y and La/Yb calibrations in some cases (e.g., Lieu & Stern, 2019, discussed above). Its disadvantage is that its utilization is limited by the simultaneous availability of all involved chemical components, which in some cases reduce the

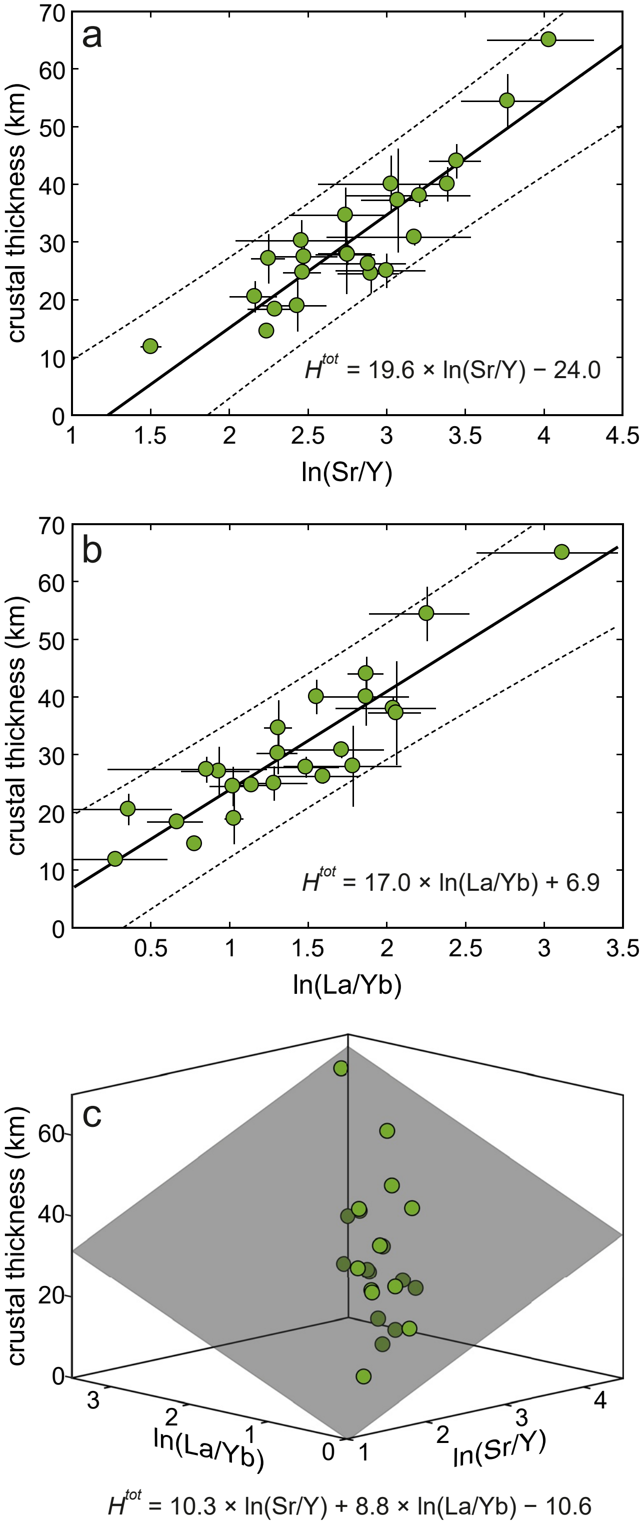

Figure 6. The Sr/Y and La/Yb mohometers of J. B. Chapman et al. (2015) and Profeta et al. (2015) recalibrated by Sundell et al. (2021): (a) simple linear regression of ln(Sr/Y) and crustal thickness; (b) simple linear regression of ln(La/Yb) and crustal thickness; and (c) multiple linear regression of ln(Sr/Y), ln(La/Yb), and crustal thickness. Green symbols and error bars defined as in Figure 5. Dotted lines in panels (a and b) delimit the 95% prediction intervals of the regressions.

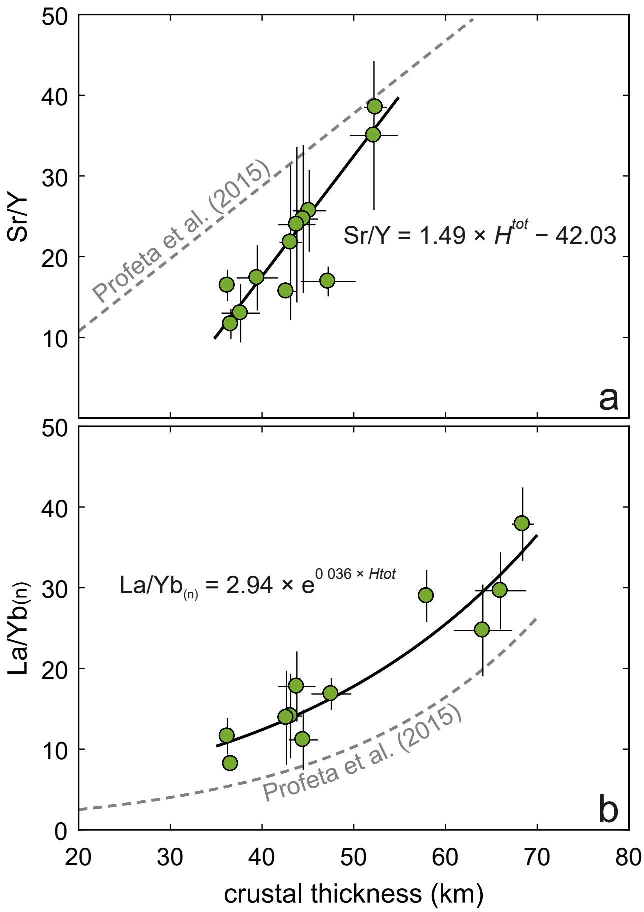

Figure 7. Correlations of (a) Sr/Y and (b) La/Yb$_{(n)}$ with crustal thickness of collisional belts (Hu et al., 2017). The regressions were obtained using median values calculated for individual collisional belt segments (green symbols); error bars represent 1σ standard deviations. The models of Profeta et al. (2015) derived for supra-subduction arcs (gray-dashed lines) are shown for reference.

size of data set to which it is applicable (e.g., the commonly performed X-ray fluorescence analyses typically include La, Sr, and Y, but not Yb).

Hu et al. (2017) found that the covariation of Sr/Y and La/Yb with crustal thickness in intermediate rocks from volcanic belts formed in collisional settings, such as the Caucasus, Anatolia, Tibet, or the Carpathians, is not reproduced satisfactorily by the models developed for active subduction zones. When applied to these belts, the Sr/Y and La/Yb models of J. B. Chapman et al. (2015) and Profeta et al. (2015) predict crustal thicknesses that are smaller and greater, respectively, than constrained by geophysical observations. (Figure 7). These discrepancies caution that the two models developed for arcs should not be applied to collisional orogens. Therefore, Hu et al. (2017) formulated a new set of equations dedicated to this type of tectonic environment:

$$H^{\mathrm{tot}} = 0.67 \times \mathrm{Sr/Y} + 28.21, \qquad R^2 = 0.91 \tag{7}$$

$$H^{\mathrm{tot}} = 27.78 \times \ln(0.34 \times \mathrm{La/Yb}_{(n)}), \qquad R^2 = 0.89 \tag{8}$$

These equations were then used in a case study tracking crustal thickness variations in the Quinling Orogenic Belt during the Triassic and Jurassic.

Interesting additions to the proxies are the Rb/Sr parameter of Dhuime et al. (2015) and the silica–elevation correlation of Farner and Lee (2017). Dhuime et al. (2015) showed that the Rb/Sr ratios of magmatic rocks in the Americas correlate with crustal thickness (Figure 8). This should not be surprising, however, since Rb/Sr is known to correlate with the silica content of igneous rocks, which has long been found to covariate with the thickness of arc crust (Coulon & Thorpe, 1981, discussed above). The proposed relationships applicable to intermediate compositions are:

$$H^{\mathrm{tot}} = 426.8 \times \mathrm{Rb/Sr} + 4.1, \qquad R^2 = 0.93 \tag{9}$$

$$H^{\mathrm{tot}} = 3.5 \times \mathrm{SiO_2}\,(\mathrm{wt\%}) - 157.8, \qquad R^2 = 0.88 \tag{10}$$

Dhuime et al. (2015) used this observation to argue that the continental crust overall became thicker and more silicic (i.e., more differentiated) starting ~3 Ga ago, coincident with the onset of plate tectonics and development of subduction zones; prior to that, the continents were rather mafic.

Farner and Lee (2017) showed that magmatic silica concentrations—and thereby, a series of other whole-rock chemical components that covariate with SiO$_2$ during differentiation—correlate well with elevation in modern arcs, for example:

$$h = 0.81 \times \mathrm{SiO_2} - 45.82, \qquad R^2 = 0.62 \tag{11}$$

$$h = -1.70 \times \mathrm{FeO_t} + 12.78, \qquad R^2 = 0.79 \tag{12}$$

$$h = -1.57 \times \mathrm{CaO} + 12.18, \qquad R^2 = 0.70 \tag{13}$$

$$h = 3.27 \times \mathrm{K_2O} - 4.54, \qquad R^2 = 0.68 \tag{14}$$

where h is elevation above sea level (km), and the components are expressed as wt% (Figure 9).

Elevation correlates with crustal thickness because most modern orogens are in isostatic equilibrium (e.g., Lee et al., 2015). This is one of the first studies that identifies the advantage of using modern elevation as a proxy for crustal thickness and indirectly suggests that these chemical parameters can be used as paleoelevation proxies as well. Also, the approach of Farner and Lee (2017) is innovative in that the involved chemical components are not calculated at the scale of entire arc segments, but rather as the mean compositions of small crustal volumes

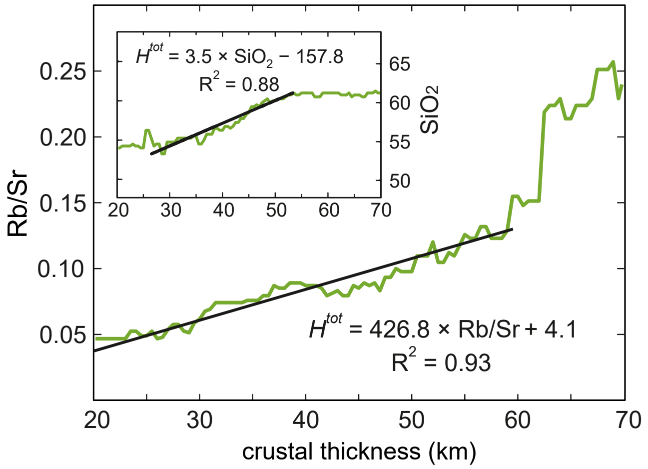

Figure 8. Covariation of Rb/Sr (and SiO_2, inset) with crustal thickness of modern arcs of Central and South America (green curves) calculated as the maximum probability function of the available data using a sliding window of 10 km (Dhuime et al., 2015). Crustal thickness is based on CRUST 1.0 (Laske et al., 2013). Regressions are limited to the intervals encompassed by the black regression line.

(10 × 10 km horizontally, 0.1 km vertically) estimated from the samples contained within these volumes, which then are distributed into 0.1-km-wide elevation brackets defined globally. Obtaining in this way results that are consistent with previous approaches indicates that the composition-thickness correlations seen in arcs at a global scale are method-independent and robust. Being formulated with the help of representative (i.e., maximum probability or mean) compositions of the volcanic level of modern arcs, the equations of Dhuime et al. (2015) and Farner and Lee (2017) may not be adequate for estimating the thickness of paleoarc segments exposing deeper crustal levels, such as the Kohistan arc (Jagoutz, 2014) and the Sierra Nevada (Ducea, Saleeby, et al., 2015), where the equivalent representative compositions may be skewed toward more mafic and thus, the obtained crust may appear as thinner.

In summary, a series of chemical parameters—major and trace element concentrations and their ratios—in arc magmas correlate with the thickness of crust and can be employed with variable success to approximate the thickness of ancient arcs and collisional orogens even if there is no consensus regarding the causes underlying these relationships.

Similar to the mohometer calibration process itself, in which correlations between composition and Moho depth or crustal thickness are rooted in the statistical treatment of large sample populations representing modern arcs,

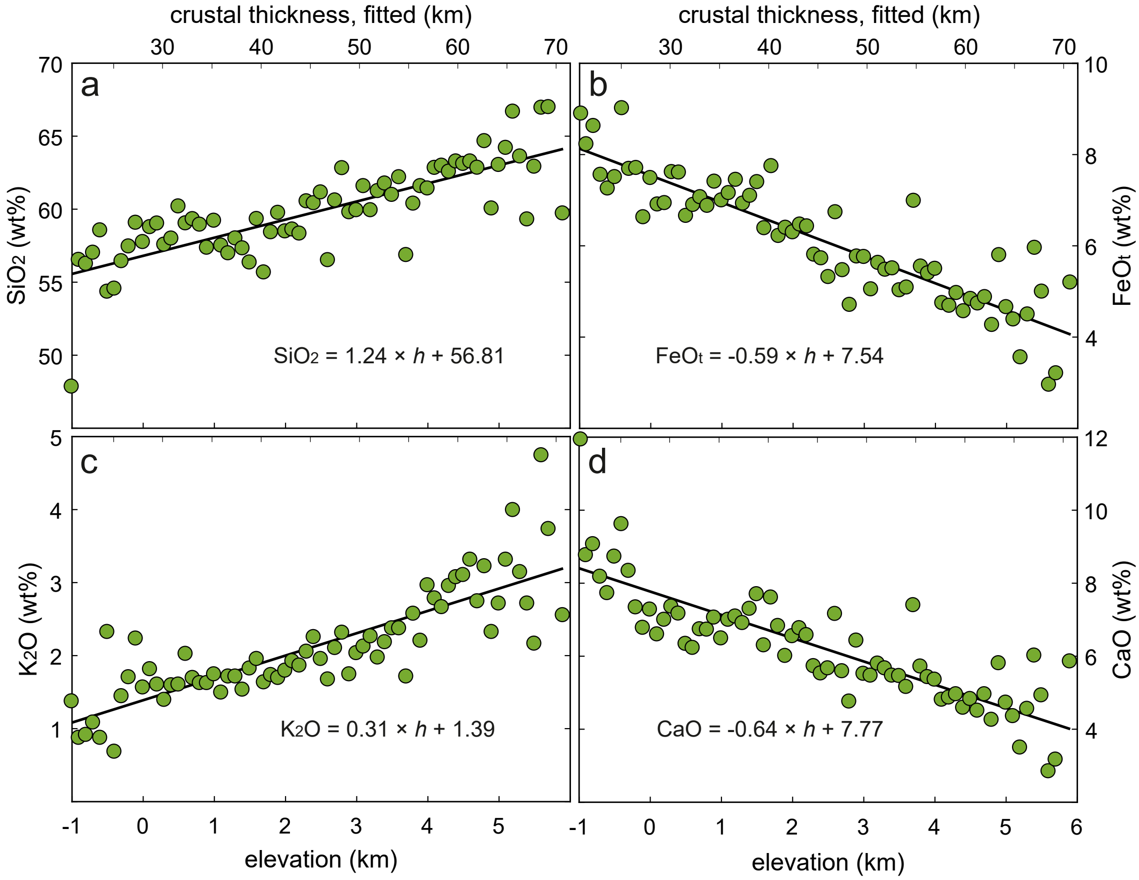

Figure 9. Correlations between major element contents of arc lavas (averaged globally over 10 × 10 × 0.1 km volumes) and elevation (Farner & Lee, 2017). Crustal thickness is fitted to elevation assuming isostatic equilibrium, densities of 2.87 g/cm^3 (crust) and 3.33 g/cm^3 (mantle), and a Moho depth of 28 km for sea-level elevations.

the quality of estimates obtained for ancient arcs with the aid of these mohometers is primarily conditioned by the size of the available data sets. Since establishing a sampling protocol that makes small data sets useful in such an endeavor is very difficult and because gathering the required large amount of chemical data may be challenging and expensive, thickness calculations for paleoarcs typically rely on data from multiple publications, are obtained with different analytical methods in different labs, and thus are qualitatively heterogeneous. Obtaining meaningful first-order estimates based on few tens of samples is possible; however, depending on the size of the investigated area, robust results in general require larger data sets capable of "seeing" through the noise caused by competing petrogenetic processes that affect the composition of magmas. Therefore, crustal thickness estimates can be expected to be generally more realistic in the case of well-sampled arc segments at lengthscales of several tens to hundreds of kilometers. At shorter scales, such as individual stratovolcanoes or volcanic fields, results may be ambiguous due to limited data availability or peculiarities of the local magma differentiation pathways (Lieu & Stern, 2019).

4.2. Zircon-Based Mohometers

Out-of-context minerals, such as zircons, from the detrital archive are of great significance for testing evolutionary models for the continental crust (Kohn, 2017). Since erosion affects disproportionately more high-elevation orogens developed along active margins than low-elevation continental interiors, zircons in detrital deposits are much more likely to be sourced in arcs and collisional belts than in rocks from intraplate settings. Not only are zircons exceptionally well preserved in sedimentary rocks and carry age information for the original (usually) magmatic source, but analyses of multiple zircons can average out large segments of the continental crust, including areas that are not well exposed or crustal domains that have been eroded away (Gehrels, 2014). Additionally, a variety of trace elements and isotopes can be measured on these crystals, adding a petrologic/geochemical dimension to the age information; measuring and interpreting these on the same zircon are the object of the new field of petrochronology (e.g., Engi, 2017; Harrison et al., 2017; Kohn, 2017; Kylander-Clark et al., 2013; Schaltegger & Davies, 2017). For a long time, zircon ages and trace element measurements were obtained on SIMS (secondary ion mass spectrometer) instruments or by split stream setups in two ICP-MS instruments. Today, zircon trace elements are most straightforwardly measured on single-collector high-resolution ICP-MS instruments simultaneously with ages (Balica et al., 2020) without requiring a split stream setup. Principal trace elements routinely analyzed in zircons are Ti, P, Y, U, Th, Hf, and the rare earth elements (REEs; Hoskin & Schaltegger, 2003). A large and growing data set of global detrital zircons analyzed for both ages and trace element chemistry exists (Paulsen et al., 2021), and that archive is expected to grow exponentially over the next decade. The great majority of zircons in the detrital archive (>98%, Balica et al., 2020) are igneous and have Ti-in-zircon crystallization temperatures (Ferry & Watson, 2007) consistent with derivation from felsic melts. Zircon-felsic melt partition coefficients determined experimentally (e.g., Burnham & Berry, 2012; Fujimaki, 1986; Watson, 1980) or empirically (e.g., Claiborne et al., 2018; J. B. Chapman et al., 2016) are used to calculate trace element concentrations of the host magma assuming zircon-melt equilibrium. Although individual zircon grains rarely reflect ideal equilibrium with their parental melt for all trace elements, zircon populations usually offer good statistical approximations of host magma compositions.

Two zircon chemistry-based mohometers have been quantified: La/Yb (Balica et al., 2020) and the Eu anomaly (Tang, Ji, et al., 2021), both being calibrated against the whole-rock La/Yb mohometer of Profeta et al. (2015).

The La/Yb$_{\text{zircon}}$ mohometer is a direct extension of the Profeta calibration but is hampered by the commonly low concentrations (<0.1 ppm) of La in igneous zircons, which can be subject to errors as large as 10% of the measurement in different instruments, and thus is limiting the applicability of this tool. In the Balica et al. (2020) study, the errors on La measurements (performed in the Laserchron facility at University of Arizona) are reported to be less than 10%, which make the quantitative estimate feasible. To calculate whole-rock La$_{\text{wr}}$ and Yb$_{\text{wr}}$ concentrations, their approach relies on the empirical partition coefficients of J. B. Chapman et al. (2016):

$$\mathrm{La_{wr}} = \mathrm{La_{zircon}} / \left(0.035 \times \mathrm{La_{zircon}}^{0.945}\right) \tag{15a}$$

$$\mathrm{Yb_{wr}} = \mathrm{Yb_{zircon}} / \left(20.18 \times \mathrm{Yb_{zircon}}^{0.433}\right) \tag{15b}$$

These values are then normalized to chondritic values and plugged into the formulation of Profeta et al. (Equation 3). Using this approach, Balica et al. (2020) showed that the calculated whole-rock La/Yb ratios

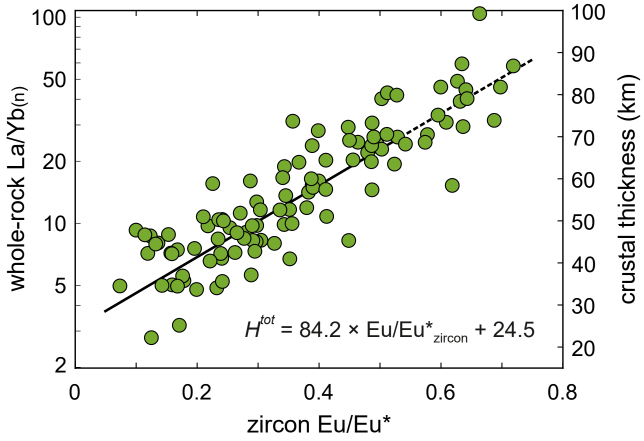

Figure 10. Correlations of whole-rock La/$\text{Yb}_{(n)}$ with Eu/Eu* in zircons and with crustal thickness (Profeta et al., 2015, Equation 3) allow directly using $\text{Eu/Eu}^*_{\text{zircon}}$ as mohometer (Tang, Ji, et al., 2021). $\text{Eu/Eu}^*_{\text{zircon}}$ of each datapoint used in the regression is the average of multiple zircon analyses from the same sample (error bars are omitted for clarity). Dashed section of the regression line indicates extrapolation beyond the La/$\text{Yb}_{(n)}$ range used to calibrate the Profeta et al. (2015) model, where predicted crustal thicknesses become unreasonably great.

deduced from the chemistry of almost 6,000 zircons of all ages from the Hadean to present are relatively constant over the course of Earth's history and would correspond to mean thicknesses of the continental crust in the 35–45 km range. This suggests that the depths of magmatic diversification and granitoid formation did not change much over time although more data with better geographic coverage are required to verify this hypothesis.

Relying on a data set of 120 samples of various ages (not modern-day volcanic rocks), Tang, Ji et al. (2021) have found that the amplitude of Eu anomalies, $\text{Eu/Eu}^* = \text{Eu}/(\text{Sm} \times \text{Gd})^{1/2}$ (chondrite-normalized), correlates with host-rock La/$\text{Yb}_{(n)}$ (Figure 10), which allowed them to formulate the $\text{Eu/Eu}^*_{\text{zircon}}$ mohometer:

$$H^{\text{tot}} = 84.2 \times \text{Eu/Eu}^*_{\text{zircon}} + 24.5 \tag{16}$$

Given the relatively high Eu, Sm, and Gd concentrations in zircons, $\text{Eu/Eu}^*_{\text{zircon}}$ has the advantage to be more precisely measured than La/$\text{Yb}_{\text{zircon}}$. It should be noted, however, that a significant fraction of the employed calibration data set involves whole-rock La/$\text{Yb}_{(n)}$ ratios considerably higher than the upper limit of the Profeta et al. (2015) model (compare Figures 5 and 10) and thus, crustal thickness estimates based on high $\text{Eu/Eu}^*_{\text{zircon}}$ values necessarily imply extrapolations of that model and must be treated with caution. As a case study, Tang, Ji et al. (2021) apply this model to the paleocrustal thickness evolution of the Tibetan plateau since the Mesozoic by measuring zircon age-Eu/Eu* pairs on detrital zircons from unnamed rivers in southern Tibet. Subsequently, the calibration was applied to a global set of zircon age-chemistry data set to generate an average “orogenic” crustal thickness evolution model from the Archean to present (Tang, Chu, et al., 2021). The zircon Eu/Eu* failed to provide a reasonable set of paleo crustal thickness estimates in a recent study of the southern Andes (Carrapa et al., 2022) but the La/Yb ratio in zircon did provide a coherent and reasonable set of values for the Cenozoic crustal thickness in the Aconcagua region.

The Sm/Yb, Gd/Yb, and Gd/Y ratios in zircon also correlate with crustal thickness (Balica et al., 2020; Paulsen et al., 2021) and hold promise because all of the involved elements are routinely measured with high precision in situ with ICP-MS or SIMS; a proper calibration of this proxy is, however, not yet available.

In conclusion, zircon petrochronology may be a quicker paleomohometric tool than the whole-rock approach and can extract information about orogen-wide patterns from just a few batches of carefully targeted zircon-bearing sediments or sedimentary rocks. One disadvantage of the method is that because current zircon-based models are tied to the La/Yb whole-rock mohometer, they not only carry over the errors associated with this particular calibration, but add further layers of uncertainty that are partly analytical and partly related to the quality of the used mineral-melt partition coefficients. Therefore, trace element data in zircons extracted from magmatic samples should be used for paleomohometry only in cases in which whole-rock chemistry is significantly affected by alterations that render whole-rock mohometers inapplicable. Another potential issue arises from the fact that there are no straightforward methods to distinguish zircons formed in arcs from those crystallized in collisional orogens or other tectonic environments and thus, the thickness of some ancient orogens may be overestimated if the Profeta et al. (2015) model is used instead of the formulation of Hu et al. (2017, see Figure 7). These shortcomings are partially counterbalanced by the ability to efficiently measure age and chemistry on large numbers of zircons by laser ablation with a single-collector high-resolution ICP-MS instrument (Balica et al., 2020) or even a quadrupole ICP-MS (Tang, Ji, et al., 2021), which not only helps reducing some of the uncertainties, but also ensures that all data used in a case study are obtained with the same method or even the same instrument, which is rarely the case with whole-rock measurements. This efficiency opens up a world of new applications for this approach.

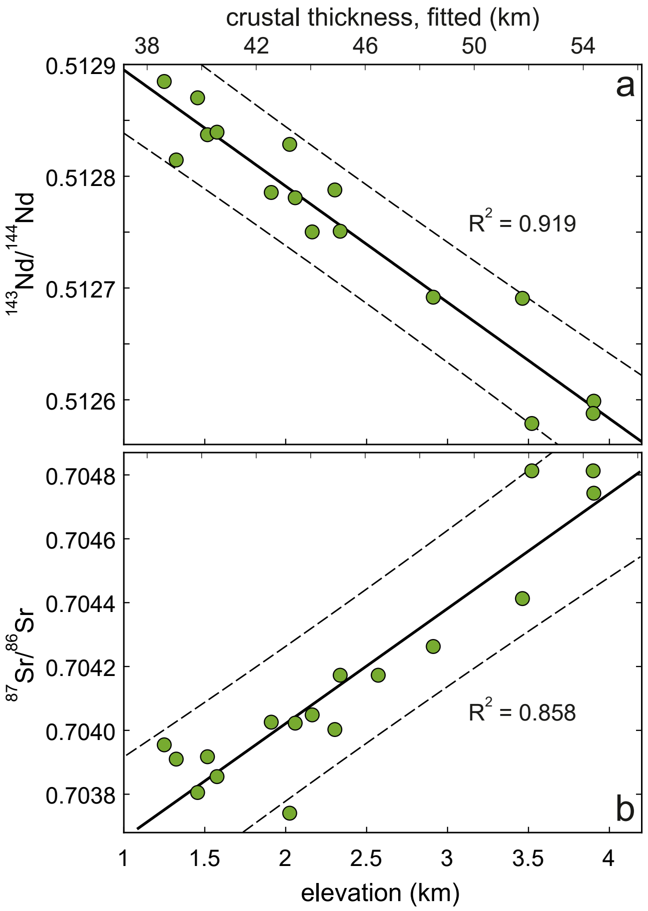

Figure 11. Correlations of (a) Nd and (b) Sr isotopic ratios with elevation in the Andean Southern Volcanic Zone (Scott et al., 2018). Elevation was smoothed to a radius of 37.5 km to filter out short-lengthscale non-isostatic variabilities. Dashed lines delimit the 90% prediction intervals of the regressions. Crustal thickness (Assumpção et al., 2013) is scaled to elevation assuming isostasy, using the data set of Scott et al. (2018).

4.3. Radiogenic Isotope Approaches

Radiogenic isotopes in arc rocks may correlate with crustal thickness and elevation in continental arcs, depending on the nature of the local basement. For example, the Coast Mountains batholith (Gehrels et al., 2009) comprises intrusions of a Mesozoic to early Cenozoic magmatic arc formed along the North American margin as a result of the subduction of various plates of the Pacific realm; the arc was emplaced into a collage of accreted terranes (Colpron et al., 2005), most of which are isotopically primitive. The batholith records change in crustal thickness over time in its trace elemental record but do not have much heterogeneity in its radiogenic isotopes (Girardi et al., 2012). In contrast, present-day and Quaternary volcanic rocks from arcs emplaced on complex and old(er) continental basement, such as the Andean SVZ, show good correlations of whole-rock radiogenic isotopic ratios (Sr and Nd) with elevations and crustal thickness (Hildreth & Moorbath, 1988; Scott et al., 2018; Figure 11), which were used to reconstruct the surface uplift of the Andean Western Cordillera since the Jurassic (Scott et al., 2018). In this interpretation, the correlation of isotopes with elevation and/or crustal thickness is region-specific, assuming that assimilation of the local basement plays a role in the diversity of isotopic ratios measured in volcanic rocks and their intrusive equivalents. Based on new Sr, Nd isotopic, and trace element data obtained on primitive end-members from the SVZ, Wieser et al. (2019) suggested that along-arc variations in isotopic enrichment of their mantle source (involving metasomatized subcontinental mantle lithosphere) superimposed on a variable headspace-limited melting have a fundamental contribution to the correlation between increasing crustal thickness and isotopic enrichment. One of their key arguments is that primitive rear-arc lavas emplaced parallel with the volcanic front share similar isotopic trends, which can be explained by a common enriched mantle source, but not by similar intracrustal processes.

DePaolo et al. (2019) applied the Neodymium Crustal Index (NCI; DePaolo et al., 1992) to volcanic rocks from Tibet to quantify paleocrustal thickness. NCI is calculated for igneous rocks as the fraction of crustal Nd assimilated in the deep crust as opposed to that derived from the underlying mantle. A baseline crustal and respectively mantle Nd isotopic ratios are chosen for a given area, and the proportion of each in a given volcanic rock is used to calculate NCI, which then can take values between 0 when the rock preserves the Nd isotopic ratio of the mantle, and 1 when the Nd isotopic ratio in the rock is equal with that of the crustal assimilant. Since the efficiency of assimilation increases with temperature and Moho temperatures increase with crustal thickness (adopting a geotherm model is required), NCI is expected to correlate with crustal thickness. The application of that study to southern Tibet shows major crustal thickening occurring between 45 and 32 Ma, consistent with other recent paleomohometric estimates (e.g., Sundell et al., 2021; Tang, Ji, et al., 2021; Zhu et al., 2017). NCI can be applied to other regions as long as there is an isotopic contrast between local basement and mantle-derived basalts.

5. New Whole-Rock Mohometers

5.1. Motivation

Our review of the literature focusing on the covariations between the composition of magmatic rocks and crustal thickness in orogenic areas leads us to three observations that may help formulate better Mohometers.

1. Though numerous correlations have been identified over the past decades between chemical parameters in magmatic rocks and crustal thickness of orogenic areas, most paleocrustal thickness calculations still rely only on a few ratios (La/Yb, Sr/Y and, to a lesser extent, Ce/Y) that often produce discrepant results. The problem

of such discrepancies can be mitigated by using mohometers in combination (Sundell et al., 2021, discussed above), which suggests that crustal thickness estimates could be further improved by increasing the number of simultaneously applicable mohometers. While other composition–crustal thickness correlations have been used to address questions related to arc petrogenesis and crustal evolution, they either were never quantified or were not designed—and thus are rather difficult to be employed—to estimate paleoarc thicknesses as is the case for Rb/Sr (Dhuime et al., 2015) or SiO_2, CaO, FeO_t, etc. (Farner & Lee, 2017). Hence, to reduce uncertainties and improve the accuracy of crustal thickness estimates, new mohometers based on these and other, so far ignored, chemical components and ratios with similar properties, need to be quantified and applied simultaneously. In addition, having available a large toolset of Moho parameters involving a variety of major and trace elements would unlock the mohometric potential of a large number of published analyses that include only major elements and few (if any) trace elements not appropriate for available approaches.

2. Chemical parameters displaying compatible or incompatible behavior tend to correlate negatively and respectively positively with crustal thickness (Turner & Langmuir, 2015a). At the same time, the more differentiated (i.e., more silicic and less magnesian) magmas are, the more enriched in incompatible components and depleted in compatible ones they tend to be. Therefore, the sensitivity of various chemical parameters to crustal thickness variations can be expected to change with magmatic differentiation in accordance with their more or less (in)compatible behavior, implying that mohometer models accounting for the effects of differentiation should be more accurate.
3. The standard approach of assessing global-scale covariations between the composition and thickness of modern arcs relies on representative (typically mean or median) values of the targeted chemical parameters and crustal thickness (or Moho depth), which are calculated from sample populations representing arc segments delimited based on geologic criteria, such as the transition from a continental to an oceanic upper plate or spatial discontinuities in the igneous activity caused by subducting aseismic ridges. To what extent does the quality of correlations (and thereby the accuracy and resolving power of the derived mohometers) depend on grouping criteria is not clear because most studies rely on arc segments delimited in the same way. The idea of Farner and Lee (2017) to evaluate global correlations by redistributing the global arc data set into artificially defined elevation bins is a noteworthy alternative to the standard approach not only because it minimizes the uncertainties associated with crustal thickness, which may be significant for many arc segments used in the standard approach, but also because the correlations obtained this way are less likely to be affected by local geochemical anomalies.

With these observations in mind, in the following, we first evaluate which of the alternative methods of defining global correlations between composition and crustal thickness is best for formulating new mohometer models for arcs, and then accounting for the possible effects of differentiation, we derive an expanded set of mohometers that involves a broad spectrum of major and trace elements. Used in combination, these may offer a better solution constraining the thickness of paleoarcs. Models derived for arcs may not be applicable to collisional orogens (Hu et al., 2017); these may require appropriate mohometers to be calibrated in a similar fashion in the future.

5.2. Calibration Data Set

5.2.1. Global Arc Data Selection and Filtering

Whole-rock major and trace element compositions of geolocated volcanic samples from arc segments were extracted from precompiled GEOROC data sets (http://georoc.mpch-mainz.gwdg.de, January 2019). The primary data were passed through a series of age and geochemical filters and screened for quality as follows.

Since crustal thickness may change over time, quantifying relationships between magma composition and geophysically determined Moho depth or elevation is meaningful only for young volcanic products. Thus, only Pliocene and younger (<5.3 Ma) samples were selected based on geographic coordinates combined with location metadata, which were checked against arc volcanoes known to be active during the Holocene and Pleistocene (https://volcano.si.edu). A total of 98% samples selected by this procedure are Holocene or Pleistocene, and the remaining 2% are Pliocene. Because GEOROC records may contain some errors, in a second step, the age-filtered data set was screened for outliers signaling such errors (e.g., mixed-up trace element concentrations, which are detectable in spidergrams; isolated data that expand the concentration range of an element in a data set by order(s) of magnitude). Where possible, the identified errors were corrected using the cited original data sources; data affected by uncorrectable errors were removed. Samples with major element totals falling outside the 97–101 wt% range or flagged in the database as significantly altered may impact the quality of calibration and were thus discarded. For the retained samples, major element concentrations were normalized to a dry 100 wt% sum. In both oceanic and continental arcs, the bulk of modern subduction zone magmatic rocks encompasses a broad differentiation spectrum dominated by subalkaline compositions (Irvine & Baragar, 1971), ranging from basalts to rhyolites. In comparison, alkaline volcanics are numerically subordinate, tend to be unevenly distributed among different arcs, and commonly feature exotic trace element signatures that are difficult to accommodate in a global-scale model like the one pursued here. Therefore, samples with total alkali content ($A = Na_2O + K_2O$) exceeding the alkaline–subalkaline boundary by more than 1.5 wt% at any given SiO_2 value were removed from the data set. For similar reasons, samples with extreme mafic (SiO_2 <45 wt%) and felsic (SiO_2 >80 wt%) compositions were also discarded. In order to identify potential new mohometers, for all remaining samples, a series of element/element ratios were computed (see discussion in Section 5.4).

5.2.2. Assigning Moho Depths and Elevations

Individual Moho depths and elevations were allocated to all samples. For each of these, a Moho depth relative to sea level was calculated based on its geographic coordinates and Moho depths of the 1° × 1° global-scale model CRUST 1.0 (Laske et al., 2013) using spline interpolation in MATLAB®. In a similar fashion, individual elevations relative to sea level were obtained for all samples from the 0.14° × 0.14° Global Multi-Resolution Topography model (GMRT; Ryan et al., 2009). Sensitivity tests indicate that among the available GMRT models (https://www.gmrt.org), this grid spacing produces the best elevation-composition correlations (see discussion below).

The resulting global arc data set (Figure 12a) contains 34,946 samples with assigned latitude, longitude, elevation, and Moho depths that are fully characterized in terms of major elements and to a lesser extent, trace elements (Table S1). The data set covers a broad interval of Moho depths and elevations (Figure 12b) and is dominated by volcanic rocks from low-elevation arcs built on oceanic and continental crust less than 40 km thick. Compositions representing arcs on thick crust with elevations exceeding 2 km above sea level are dominated by Andean samples and are thus necessarily skewed toward the geochemical particularities of the modern South American subduction magmatism. Spanning across the entire basalt–andesite–dacite–rhyolite differentiation spectrum, most of the data sets consist of intermediate compositions (52–63 wt% SiO_2 and 2–6 wt% MgO), regardless of elevations and Moho depths (Figures 12c and 12d). Felsic samples (SiO_2 >63 wt% and MgO <~2 wt%), although subordinate, are also well represented at all elevations. In comparison, mafic samples (SiO_2 <52 wt% and MgO >~6 wt%) are less abundant, being strongly underrepresented in the thickest, high-elevation arc segments.

5.2.3. Data Processing: A Global Arc Median Data Set

In order to obtain reliable, high-resolution models capable of predicting Moho depths or elevations from differentiation-dependent chemical compositions of arc samples, we need a practical solution to reduce the vast global arc data set into a computationally efficient calibration data set that consists of values representing data subsets grouped by a compositional and a crustal parameter. Three different methods were evaluated as follows. The global arc data set was divided into sample bins defined as 2D grid cells, in which one set of gridlines consists of equally spaced brackets of MgO, a chemical component taken as a differentiation indicator, whereas the other delimits either an array of 26 arc segments with different average crust thicknesses, like in previously published mohometer calibrations (e.g., J. B. Chapman et al., 2015; Profeta et al., 2015) (*method 1*) or a series of equally spaced Moho depth intervals (*method 2*) or elevation intervals (*method 3*). The sizes of MgO, Moho depth, and elevation brackets were determined by a trial-and-error approach meant to maximize the number of samples hosted in the bins while maintaining a practical and meaningful resolution along the dimensions defining these bins. Accordingly, in the different binning methods, samples were first pooled either into predefined arc segments, into 3.5-km-wide Moho depth brackets, or into 0.5-km-wide elevation brackets and were then further separated into partially overlapping 2 wt% wide MgO bins spaced at 1 wt% intervals. Data coverage of the resulting bins is highly heterogeneous regardless of the adopted method. Medium- and low-MgO bins comprising andesites, dacites, and rhyolites common in all arcs are typically populated by hundreds to thousands of data

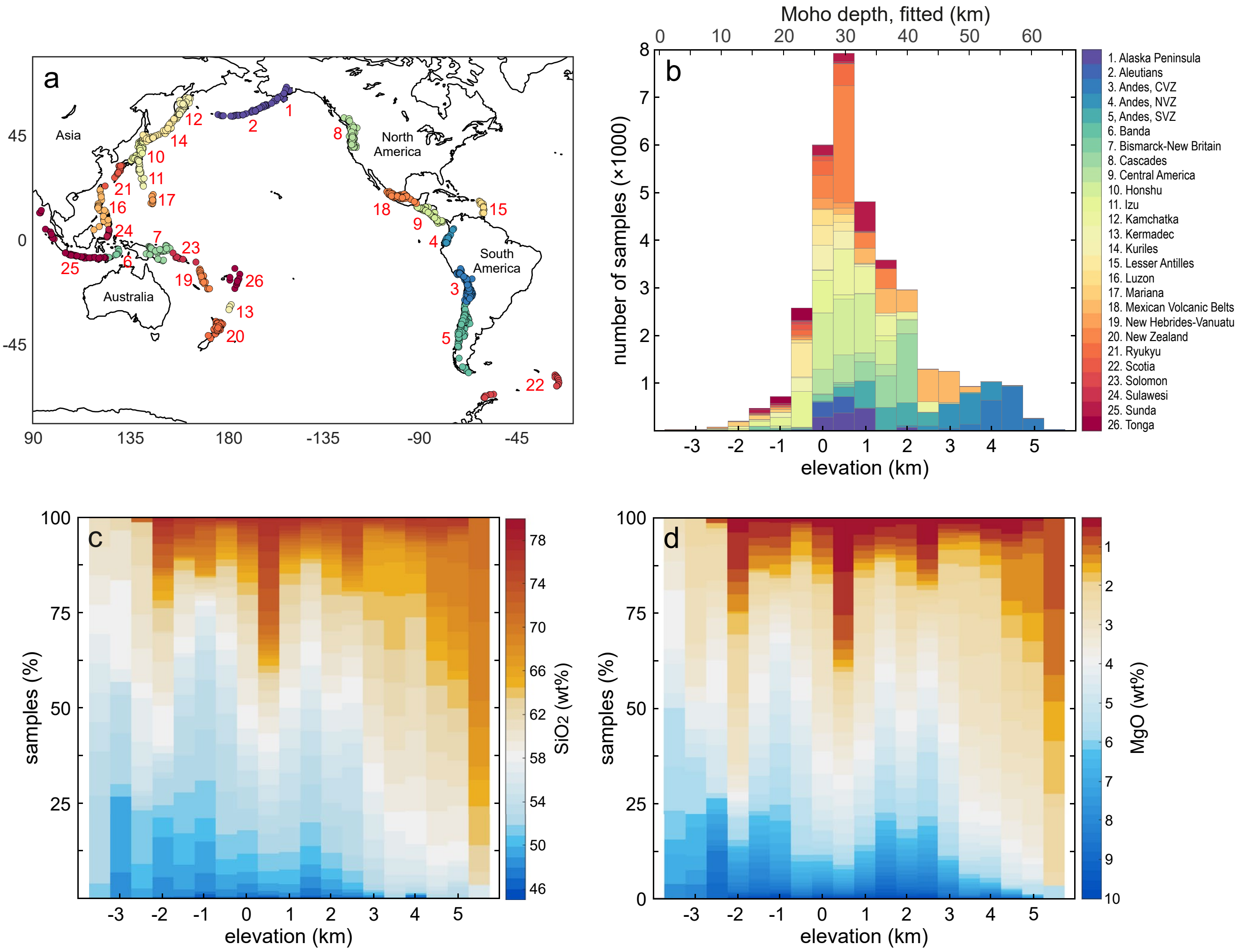

Figure 12. Global arc data set: (a) geographic distribution; (b–d) stacked histograms showing the distribution of sampled elevations as a function of arc segments (b), (c) SiO_2, and (d) MgO. Moho depth in panel (b) is fitted to elevation using Equation 17. Numbering of arc segments in panel (a) corresponds to list in panel (b). Abbreviations: CVZ—Central Volcanic Zone, NVZ—Northern Volcanic Zone, SVZ—Southern Volcanic Zone.

for major elements and tens to hundreds of data for trace elements. On the other hand, data counts in high-MgO bins corresponding to primitive basalts tend to be significantly lower or even zero in the case of less commonly analyzed trace elements. Finally, in all bins defined by the above-outlined methods, a representative median value was computed for each variable included in the global arc data set. (Using medians instead of means is preferable, provided that non-normal data distributions and outliers are common in the arbitrarily defined bins.)

A comparison of the resulting three global arc median data sets indicates that the examined binning methods strongly influence the distribution of median values in the composition versus Moho depth or elevation space and thus impact the ability of various geochemical parameters (i.e., elements and their ratios) to predict crust thicknesses. We found that medians calculated at the scale of arc segments produce very weak to moderate correlations between Moho depths and compositions. Binning arc data by Moho depths globally tend to enhance these correlations in some cases significantly. The most dramatic improvements, however, result from pooling the global data set into elevation bins. These differences are illustrated in Figure 13, in which the behavior of two potential mohometers, the total alkali content, A, and the Ce/Y ratio is shown for the 1–3 wt% MgO interval representative for the bulk of andesites and dacites.

To the first order, we ascribe such striking differences to a combination of factors. For instance, chemical peculiarities of magmas imposed by various local geological factors may distinguish a particular arc segment from

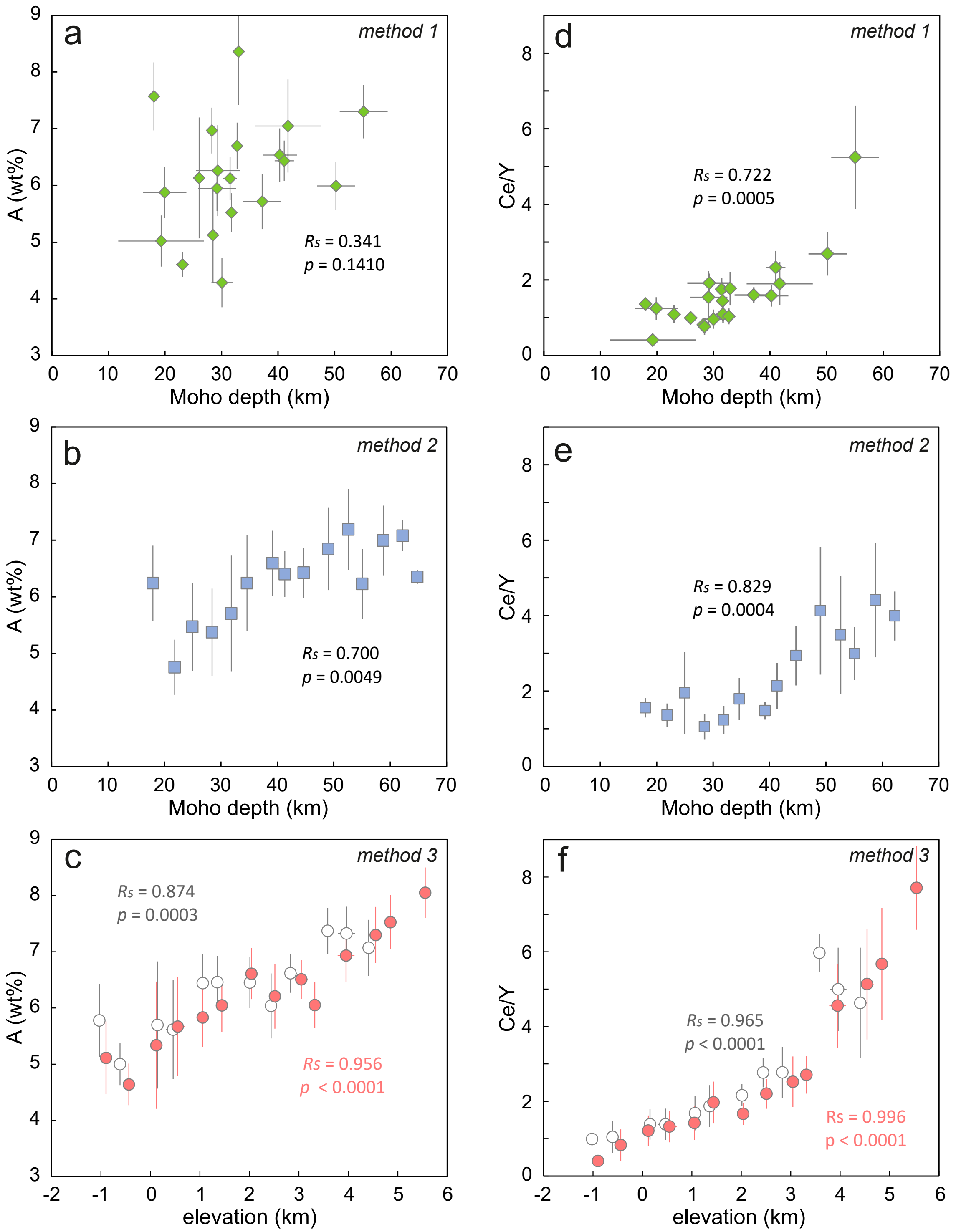

Figure 13. The effect of different data binning methods on the quality of correlation of global arc chemistry with Moho depth and elevation, illustrated for the 1–3 wt% MgO bin: (a–c) alkali content, A = $Na_2O + K_2O$; (d–f) Ce/Y ratio. Datapoints in panels (a and d) are median values calculated at the scale of individual arc segments (*method 1*). Datapoints in panels (b and e) are medians obtained by sorting samples into globally defined Moho depth intervals of 3.5 km (*method 2*). Datapoints in panels (c and f) are median values obtained by sorting samples into globally defined elevation intervals of 0.5 km (*method 3*) based on two Global Multi-Resolution Topography models with different resolutions: 0.14° × 0.14° (red) and 1.12° × 1.12° (white). Error bars in all diagrams represent median absolute deviations. The strength of correlations is quantified using Spearman's nonparametric rank correlation coefficient, R_s, which, unlike the commonly used Pearson formulation, is appropriate for evaluating both linear and nonlinear monotonic trends ($R_s = 0$ means no correlation, whereas $R_s = -1$ and $R_s = +1$ correspond to perfect negative and respectively positive correlation). Note the poorer correlation resulting for the coarser Global Multi-Resolution Topography model in panels (c and f). See text for discussion.

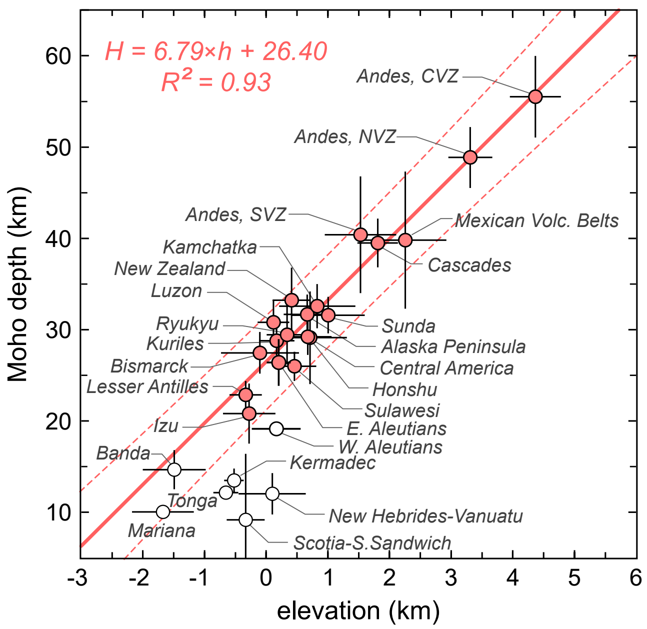

Figure 14. Global-scale elevation–Moho depth correlation in arcs. Datapoints represent arc-wide median values computed using the CRUST 1.0 model and sample locations; error bars are median absolute deviations. Regression is calculated from red-filled symbols only and is thus applicable to arcs thicker than ~20 km; dashed lines delimit the 95% prediction interval. Moho depths in thin oceanic arcs tend to be underestimated by CRUST 1.0 (empty symbols) and are thus not used in the regression. Further details are given in the text.

others with similar Moho depths when binning method 1 is employed but may have a negligible effect on the median compositions computed in globally defined narrow Moho depth bin(s) to which that segment contributes data when method 2 is used. This effect may be amplified in the case of arc segments characterized by significant variations in crustal thickness. Finally, if elevation–composition and Moho depth–composition trends are equivalent, the observation that a dense GMRT grid produces better correlations than the coarser grid underlying the CRUST 1.0 model not only reflects the fact that elevation is better constrained than Moho depth, but also suggests that crustal thickness in active arcs isostatically controls topography at length scales comparable to the grid spacing chosen for elevation. Indeed, employing a GMRT model with a lower spatial resolution (1.12° × 1.12°), which is similar to that used in CRUST 1.0, tends to result in a lower quality of such correlations (Figures 13c and 13f).

In summary, we expect the median data set obtained by binning global arc data by elevation and MgO (method 3) to produce the strongest correlations. Adopting this data set (Table S2) in mohometer calibration requires a formula converting elevations to Moho depths.

5.3. Global-Scale Elevation—Moho Depth Correlation in Arcs

Elevation is a good proxy for Moho depths at the scale of arc segments if a robust, globally validated correlation model linking these two parameters is established. For each arc segment included in the data set, a representative elevation (h, km) and Moho depth (H, km) were computed as median values of the elevations and Moho depths attributed to all samples available from that segment. Plotting median elevations and Moho depths against each other (Figure 14) reveals a strong linear correlation between the two parameters in the case of arc segments with H >20 km:

$$H = 6.79(\pm 0.95) \times h + 26.40(\pm 1.45), \qquad R^2 = 0.93 \tag{17}$$

A nearly identical relationship, $H = 6.77(\pm 0.07) \times h + 26.39(\pm 0.12)$, was produced by averaging 10,000 regression slopes and intercepts obtained using mean elevation and Moho depth values computed for variable-size random sample subsets, which were repeatedly extracted from each of the arc segments with H >20 km. The thickest arc segments, the Central and Northern Andes, represent isolated datapoints separated by a large gap from the thinner segments and may thus have an important leverage on Equation 17; however, in their absence, the equation would be very similar, $H = 6.96(\pm 1.86) \times h + 26.29(\pm 1.72)$, $R^2 = 0.81$. In a simple view assuming Airy isostatic equilibrium, the slope of Equation 17 can be expressed in terms of average densities of crust (ρ_c) and lithospheric mantle (ρ_m), $\mathrm{d}h/\mathrm{d}H = \rho_m/\rho_c - 1$, and requires $\rho_m/\rho_c = 1.15$, which is satisfied by a 2.83–2.87 g/cm^3 arc crust underlain by a 3.25–3.30 g/cm^3 lithospheric mantle. In this view, to maintain their elevation and Moho depth consistent with Equation 17 in the presence of significant amounts of ultramafic cumulates beneath the Moho (i.e., $\rho_m > 3.30$ g/cm^3), arcs would require proportionally denser crust.

In the case of thin arcs (H <20 km), such a correlation is apparently absent. This is at least in part an artifact of the CRUST 1.0 model that, given its rather coarse spatial resolution, underestimates Moho depths beneath narrow arcs emplaced on oceanic crust. For instance, regional geophysical studies indicate in comparison 1.6–2.3 times deeper Moho beneath island arcs Tonga (18–20 km, Contreras-Reyes et al., 2011), New Hebrides–Vanuatu (27 ± 2 km, Coudert et al., 1984), and Mariana (~18 km, Takahashi et al., 2007). Including these values in the global regression yields $H = 6.69(\pm 0.81) \times h + 26.44(\pm 1.20)$, $R^2 = 0.94$, which in practice is undistinguishable from Equation 17. Provided that the majority of segments making up the data set are more than 20 km thick and because many geochemical data cannot distinguish arcs thinner than 15–20 km (Figure 15); hereafter, we use Equation 17 to convert elevations to Moho depths. Equation 17 is open to amendments and revisions as the areal coverage of geochemical sampling improves and the global Moho model is refined by new geophysical data.

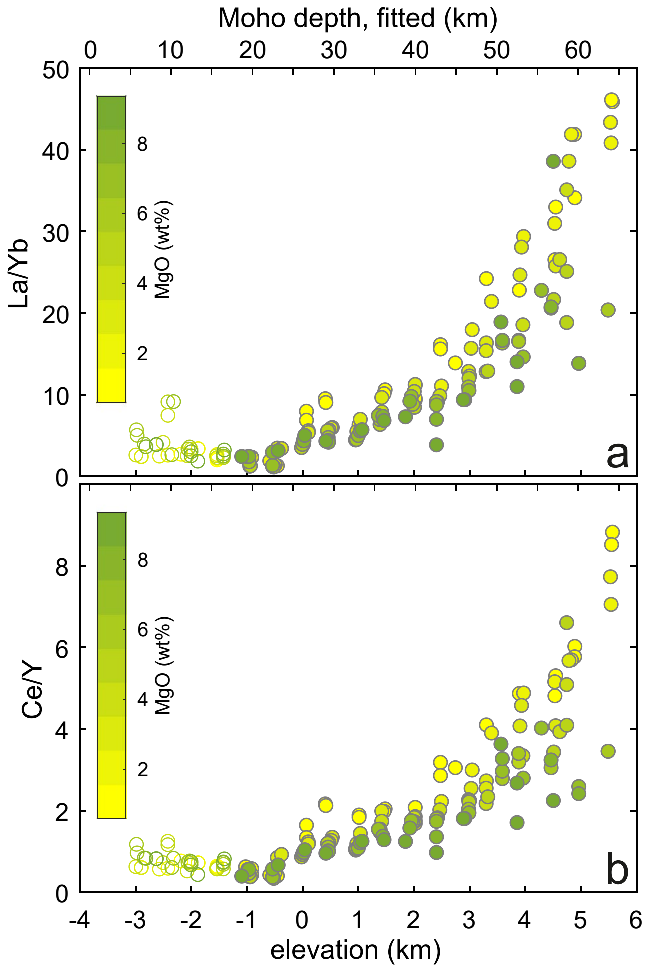

Figure 15. MgO-binned median La/Yb (a) and Ce/Y (b) versus elevation and Moho depth (fitted using Equation 17). The two ratios are representative of a series of chemical parameters of which sensitivity to crustal thickness variations is important in arcs thicker than 15–20 km but becomes insignificant in thinner arcs and thus cannot distinguish these (empty symbols) at any MgO.

5.4. Calibration of Differentiation-Dependent Mohometer Models

5.4.1. Methodology

The global arc median data set (Table S2) contains all the information required to formulate quantitative models predicting topographic elevations—and thereby Moho depths—with the help of mohometers (i.e., chemical parameters sensitive to changes in crustal thickness), that are sensitive to magmatic differentiation. We constructed a series of mohometer models, each consisting of a 3D surface fitted to datapoints defined by three coordinates: an elevation-sensitive chemical parameter X (major or trace element concentration, ratios of elements), MgO as an igneous differentiation indicator, and elevation h. To obtain $h = f(X, \text{MgO})$ model surfaces, we used the nonparametric method LOWESS (Locally Weighted Scatterplot Smoothing; Cleveland & Devlin, 1988) in MATLAB®, which is designed to smooth data via locally weighted linear regression. The term *locally weighted* indicates that the regression relies on a weight function applied to all datapoints contained within an arbitrarily defined *span*, the percentage of the total number of datapoints in the data set used in the neighborhood of each point on the model surface to determine its smoothed value. The weight function is the tricube function, $w_i = (1-|d_i|^3)^3$, where d_i is the distance in the X–MgO plane between datapoint i within the span and the point for which h is fitted, normalized to the maximum distance over all points within the span.

In the following, we present the concept and procedures underlying our mohometer modeling through the example of the Ce/Y parameter initially calibrated for basaltic compositions by Mantle and Collins (2008). Primary Ce/Y ratios were calculated for 17,420 GEOROC datapoints that include both Ce and Y data as described above. A first-order qualitative insight into the differentiation-dependent elevation sensitivity of this mohometer is provided in Figure 16a: plotting Ce/Y against MgO and elevation for individual samples reveals that an increase in this ratio with elevation is more pronounced toward the low-MgO end of the differentiation spectrum. Median Ce/Y–MgO–h datapoints obtained from the primary data, as described in Section 5.2.3, make this behavior more evident (Figure 16b). Next, a LOWESS surface is fitted to the median Ce/Y–MgO–h datapoints based on five or more samples (medians calculated from less than five samples are considered statistically unsubstantiated and excluded). The fitting procedure implies manually tuning the span and excluding outliers (isolated individual datapoints and datapoints associated with residuals greater than ca. 1 km) until a regression with acceptable accuracy metrics, R^2 (coefficient of determination) and RMSE (root mean square error, or the standard deviation of the residuals, i.e., prediction errors), and a reasonably smooth surface are obtained.

The overall aim is to obtain a LOWESS surface that predicts Moho depths strictly increasing or decreasing at given MgO, is as smooth as possible, and maintains the number of datapoints as well as the quality of regression as high as possible (i.e., high R^2 and low RMSE). We looked for mohometer models that reproduce the employed data set with an accuracy of $R^2 > 0.9$ and RMSE < 0.5 km in elevation ($<\sim 3.5$ km in Moho depth), which correspond to the size of binning intervals we used to define the global arc median data set. Using a meager span (<20%–25%) results in a high-accuracy regression (high R^2, low RMSE), but also in a convoluted, overfitted surface ruled by narrow neighborhoods around the individual datapoints, which renders the model ambiguous (featuring local maxima and minima), overly specific with respect to the used data, and useless beyond these. Conversely, a too generous span (>60%–65%) includes data from too broad neighborhoods and thus produces a smooth but underfitted surface with a poor accuracy of the regression (low R^2 and high RMSE) that weakens the predictive power of the model. The accepted reference elevation model (REM) resulting from the tuning procedure (Figure 16c) relies on 111 Ce/Y–MgO–h median datapoints. Finally, Equation 17 is used to convert REM

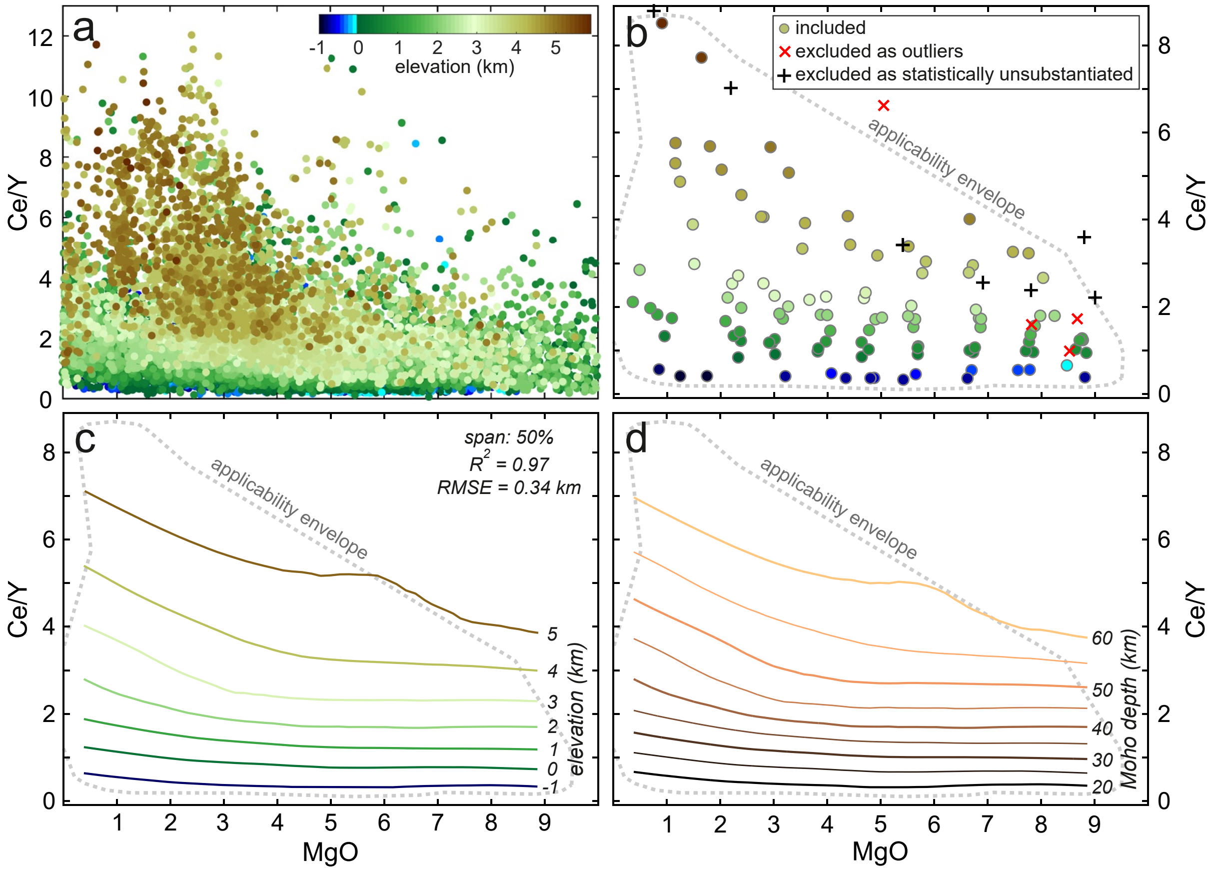

Figure 16. Mohometer calibration workflow illustrated for the Ce/Y parameter. (a) Individual Ce/Y-MgO datapoints of the global arc data set, colored by elevation; (b) elevation- and MgO-binned median Ce/Y–MgO–*h* datapoints (global arc median data set); datapoints marked as outliers or statistically unsubstantiated are excluded; (c) the Locally Weighted Scatterplot Smoothing reference elevation model (REM) surface fitted to median datapoints shown in panel (b); (d) the Moho depth model surface obtained by converting REM with the help of Equation 17. The applicability envelope (dotted gray line in panels (b–d), automatically determined by a MATLAB® boundary function applied to the median Ce/Y–MgO–*h* datapoint cloud in panel (b)) is imposed to prevent the model from being used outside its calibration range.

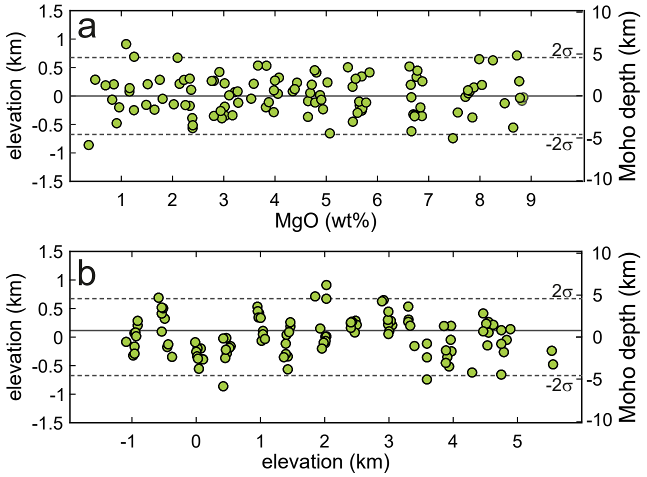

Figure 17. Distribution of model residuals in terms of elevation (on the left) and Moho depth (on the right) associated with the Ce/Y mohometer as a function of (a) MgO and (b) elevation. Dotted lines delimit the 2σ range of residuals.

into a Moho depth model (Figure 16d). The distribution of residuals associated with the model as a function of MgO and elevation along with their 95% confidence interval (2σ) is presented in Figure 17.

5.4.2. New Mohometers

Following the procedure outlined in the previous subsection, we evaluated a variety of *X*–MgO–*h* LOWESS surfaces, where Moho parameter *X* may be an individual chemical component (major element oxide or trace element) or a bivariate parameter (i.e., sum or ratio of individual chemical components). Properly chosen bivariate parameters have the advantage of better correlating with elevation and thus may serve as better mohometers than any of the individual components defining them. This difference is illustrated by the behavior of the above-presented Ce/Y ratio compared with Ce and Y (Figure 18).

By combining individual chemical components that display opposite correlations with elevation similar to Ce and Y, several other useful bivariate mohometers can be obtained. These often have the additional benefit of being applicable to MgO and elevation intervals in which models based on the chemical components defining them perform poorly and thus have limited utility.

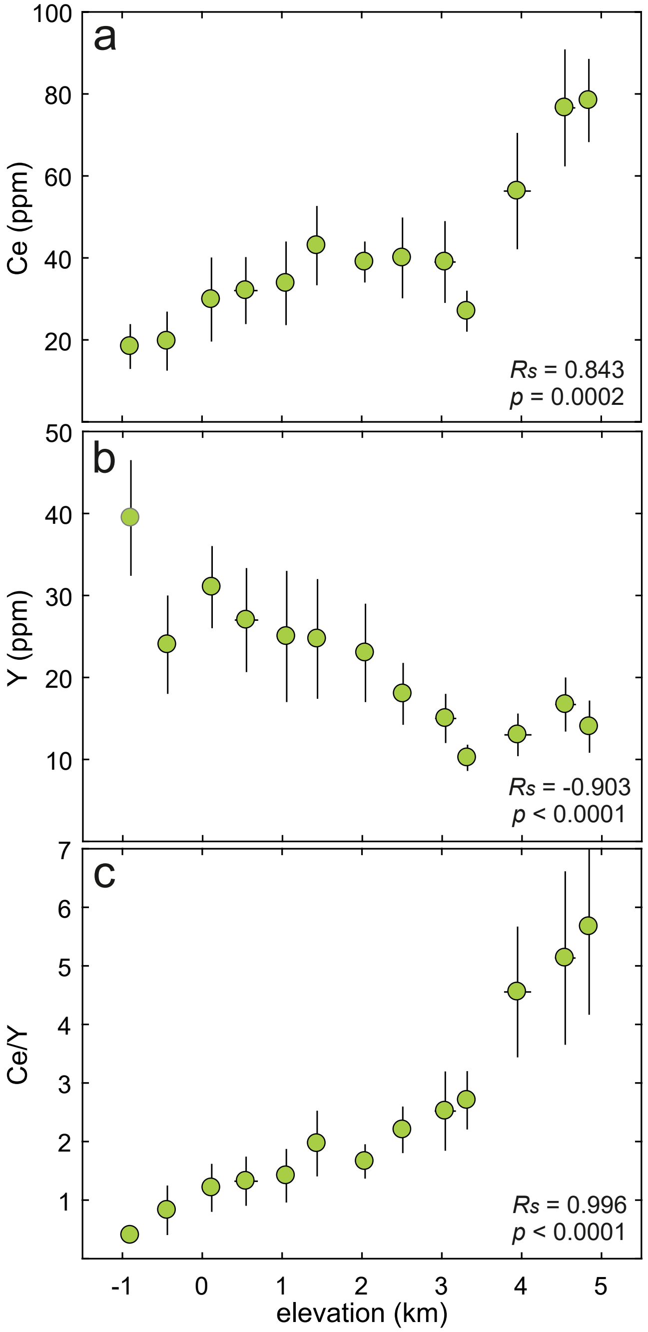

Figure 18. Correlation of median Ce (a), Y (b), and Ce/Y (c) with the elevation in the 1–3 wt% MgO bin, quantified by Spearman's rank correlation coefficient, R_s. Outlier Ce and Y values affecting the quality of Ce–*h* and Y–*h* correlations lose effect when using their ratio, which explains the stronger Ce/Y–*h* correlation. Excluding these outliers improves the Ce–*h* and Y–*h* correlations, but also results in lesser constrained models.

We calibrated 41 mohometer models, including Ce/Y; 15 involve individual elements and the other 26 rely on element ratios (Table 1). In addition to a series of newly identified Moho parameters, the list includes new formulations of the Sr/Y and La/Yb mohometers (J. B. Chapman et al., 2015; Profeta et al., 2015; Sundell et al., 2021) as well as mohometers based on elements and ratios recognized as sensitive to Moho depth variations, such as FeO (Chiaradia, 2014; Farner & Lee, 2017), CaO (Farner & Lee, 2017; Plank & Langmuir, 1988; Turner & Langmuir, 2015a), K_2O (Coulon & Thorpe, 1981; Farner & Lee, 2017; Hildreth & Moorbath, 1988; Turner & Langmuir, 2015a), Ba, Sr, Sc (Hildreth & Moorbath, 1988; Turner & Langmuir, 2015a), Ce/Yb (Hildreth & Moorbath, 1988), Zr/Y (Mantle & Collins, 2008), La/Sm, Dy/Yb, Zr/Ti (Turner & Langmuir, 2015a), Sm/Yb (Mahlburg-Kay & Mpodozis, 2001), etc. In the case of others, for example, SiO_2 (Farner & Lee, 2017), Na_2O, P_2O_5, Zr/Sm (Plank & Langmuir, 1988; Turner & Langmuir, 2015a), and Rb/Sr (Dhuime et al., 2015), we did not find the quality of correlation with elevation satisfactory; hence, these were not incorporated in our collection. While most mohometers are applicable to the 0–10 wt% MgO range, a series of calibrations had to be restricted to narrower intervals due to quality concerns related to excessive residuals and statistically unsubstantiated median datapoints affecting the low- and high-MgO ends of the investigated arc differentiation spectrum. In addition, most mohometer calibrations lack high-MgO data support at elevations exceeding 4.5 km. In order to avoid unrealistic Moho estimates resulting from extrapolations of the models, for each mohometer, we imposed an applicability envelope limited in terms of *X* and MgO, determined by an automatically drawn boundary line enveloping all datapoints that underpin the LOWESS surface (Figures 16b–16d). Outside the applicability envelope, the models are prone to predict spurious Moho depths and should be treated with caution.

All calibrated REM surfaces are included in Supporting Information S1 accessible via MATLAB® and are plotted in Figure S1 along with the corresponding *X*–MgO–*H* Moho depth models (obtained with Equation 17), applicability envelopes, as well as model residuals. Representative types of mohometer model surfaces are presented in Figure 19 and will be discussed below. To estimate the elevation and crustal thickness of paleoarcs, these mohometers can be employed individually or in combination, depending on their applicability to a given geochemical data set as discussed below.

5.5. Evaluation of New Models

5.5.1. Effects of Differentiation on Moho Estimates

The diversity of model *X*–MgO–*H* surfaces presented in Figures 16d and 19 and Figure S1 reveals that the ability of chemical parameters to accurately predict Moho depths is variably influenced by MgO, one of the several measures of igneous differentiation and the one that we use here. A series of parameters, such as Sr, Sr/Y, as well as ratios involving mid and heavy rare earth elements (MREE/HREE, i.e., Nd/Yb, Sm/Yb, Gd/Yb, and Dy/Yb), appear not to be significantly influenced by MgO, that is, a given value of *X* is expected to predict within error similar Moho depths across much of the differentiation spectrum. In the case of other mohometers, the effect of differentiation is mild but distinct and may depend on the value of MgO and in several cases, on the value of *X* itself as well. Parameters like MnO, K_2O, Ba, Ga, Sc, Zr/Y, and ratios of light to heavy rare earth elements (LREE/HREE, i.e., Ce/Y and La/Yb) belong to this group. For example, the effect of MgO content on the Sc–*H* and Zr/Y–*H* correlations is negligible in basaltic samples, but distinct in more evolved lithologies. Differentiation has

Table 1
Calibrated Mohometer Models, Sorted by Decreasing R^2

#	Mohometer	n[a]	LOWESS span (%)	R^2	RMSE (h, km)	RMSE (H, km)	2σ (h, km)	2σ (H, km)	MgO range[b] (wt%)
1	La/Yb	114	30	0.973	0.316	2.14	0.628	4.267	0–10
2	Ce/Yb	114	30	0.972	0.318	2.16	0.634	4.303	0–10
3	Lu/Hf	114	40	0.972	0.321	2.18	0.638	4.334	0–10
4	Nd/Yb	112	30	0.971	0.320	2.18	0.638	4.332	0–10
5	La/Y	110	30	0.970	0.319	2.17	0.636	4.319	0–10
6	Nb/Y	110	30	0.969	0.334	2.27	0.667	4.531	0–10
7	Sm/Yb	111	40	0.968	0.340	2.31	0.678	4.601	0–10
8	Ce/Y	111	50	0.968	0.341	2.32	0.679	4.610	0–10
9	Nd/Y	111	30	0.967	0.339	2.30	0.674	4.579	0–10
10	Th/Yb	89	40	0.966	0.366	2.48	0.727	4.940	0–8
11	Hf	95	35	0.965	0.357	2.42	0.710	4.824	1–10
12	La/Sm	111	30	0.965	0.362	2.46	0.720	4.889	0–10
13	Gd/Yb	103	35	0.962	0.361	2.45	0.718	4.873	0–10
14	Ba/V	92	30	0.962	0.349	2.37	0.694	4.714	1–10
15	MnO	112	35	0.961	0.381	2.58	0.754	5.123	0–10
16	K_2O	96	40	0.961	0.374	2.54	0.744	5.055	1–10
17	Zr/Y	108	30	0.960	0.357	2.42	0.710	4.821	0–10
18	Ba/Sc	95	30	0.959	0.373	2.53	0.742	5.035	1–10
19	A[c]	93	40	0.958	0.383	2.60	0.762	5.175	1–10
20	Nb/Yb	108	40	0.958	0.390	2.65	0.776	5.267	0–10
21	Dy/Yb	105	50	0.957	0.388	2.64	0.773	5.250	0–10
22	A/CaO	97	40	0.956	0.396	2.69	0.785	5.327	1–10
23	Th/Y	104	35	0.956	0.407	2.77	0.817	5.547	0–10
24	CaO	95	40	0.952	0.403	2.74	0.797	5.414	1–10
25	Rb	71	40	0.951	0.430	2.92	0.854	5.801	1–8
26	Ni/Sc	102	30	0.951	0.388	2.63	0.772	5.239	0–10
27	Sc	105	35	0.951	0.434	2.95	0.864	5.868	0–10
28	Ga	71	40	0.950	0.460	3.12	0.913	6.200	0–8
29	Pb	86	35	0.949	0.424	2.88	0.842	5.717	1–10
30	Ba	93	45	0.947	0.415	2.82	0.826	5.605	1–10
31	U	89	40	0.943	0.468	3.17	0.930	6.314	1–10
32	FeO_t	99	35	0.941	0.432	2.93	0.857	5.822	0–10
33	Cr/Sc	103	30	0.941	0.438	2.97	0.872	5.919	0–10
34	Ni	83	35	0.941	0.382	2.59	0.755	5.127	1–10
35	Sr/Y[d]	72	50	0.940	0.457	3.10	0.908	6.166	0–7
36	Sr	91	40	0.939	0.446	3.03	0.883	5.995	1–10
37	Zr/Ti	78	50	0.932	0.454	3.08	0.902	6.121	2–10
38	Ni/V	93	30	0.928	0.452	3.07	0.897	6.093	0–10
39	Cr/V	96	30	0.928	0.448	3.04	0.892	6.056	0–10

Table 1
Continued

#	Mohometer	n[a]	LOWESS span (%)	R^2	RMSE (h, km)	RMSE (H, km)	2σ (h, km)	2σ (H, km)	MgO range[b] (wt%)
40	Co	50	40	0.921	0.474	3.22	0.939	6.375	3–9
41	Cr	83	40	0.918	0.504	3.46	1.013	6.881	1–10

[a]Number of datapoints. [b]MgO range of calibrations, given as the lower and upper brackets of the minimum and maximum MgO bin, respectively, used in calibrations. [c]$A = Na_2O + K_2O$ (wt%). [d]Sr/Y calibration data set additionally filtered for samples with Rb/Sr < 0.05 or Rb/Sr > 0.2 following A. D. Chapman et al. (2015) and J. B. Chapman et al. (2015) to preserve consistency with previous calibrations.

no notable influence on crustal thickness estimates at low Zr/Y, Ce/Y, and La/Yb values representative for arc crusts thinner than average, but it does affect estimates at higher values of these ratios corresponding to thicker crusts. In the case of such parameters, a difference of 1 wt% MgO implies typically less than 5 km difference in Moho depth estimates for a given X value. On the other hand, several mohometers, including Ni, Co, Cr, Th/Yb, Ba/V, and A/CaO, are at least in some MgO intervals strongly controlled by differentiation. In their case, 1 wt% contrast in MgO commonly translates into differences in Moho depth estimates that may exceed 10 km for a given value of X. In some of these cases (e.g., Th/Yb and Th/Y), the effect of MgO on Moho estimates is significant at higher X values and negligible at their low values.

5.5.2. Accuracy, Precision, and Resolution of Mohometers

The 41 calibrated mohometer models involve a total of 3,975 median X–MgO–h datapoints, 95% of which elevations are reproduced within ±0.78 km and 68% within ±0.39 km. Because model residuals display a normal distribution around zero (Figure 20a), these values express the mean precision and accuracy (in terms of standard deviation and respectively RMSE) of the models in Table 1.

Residuals associated with individual mohometers also show normal distribution around zero as well as cumulative distribution functions (CDFs) that group tightly around the bulk CDF involving all residuals (Figure 20a). Residuals sorted by the MgO bins used in the calibration display similar CDFs (Figure 20b), indicating that differentiation has a limited effect on the accuracy and precision of the mohometers. Diagrams depicting the distribution of residuals of individual mohometers with MgO content (Figure 17a, Figure S1) support this observation. In contrast, residuals grouped by the elevation bins used in calibrations show less coherent systematics: non-normal distributions of the residuals are common, and CDFs obtained for these groups (Figure 20c) show more pronounced deviations from the bulk CDF, reflecting the fact that elevation affects both the accuracy and precision of mohometers. Such effects are most evident in the case of the −0.5 and 1 km bins in which the rightward displacement of the CDFs indicates that calibrations mostly underestimate the reference elevations. Albeit small, these errors locally degrade the resolving power of mohometers, particularly, if the neighboring elevation bins are affected by errors with opposite signs. Median values and probability density distribution of elevation-binned model estimates obtained for datapoints used in the calibrations plotted against medians of their binned reference elevations show this effect (Figure 21a). However, as suggested by the probability density curves in Figure 21a, all elevation bins contain subsets of model estimates, which alone or in combination can reproduce the reference elevations accurately and precisely. That is, the availability of a large set of mohometers permits high-quality estimates by allowing selection the best calibrations for a given range of elevations. For example, in comparison to the indiscriminate usage of all available calibrations (Figure 21a), employing a subset that includes only the 10 best mohometers (first 10 listed in Table 1) results in median Moho depth estimates that show significant improvements in resolution and precision for elevations exceeding 2.5 km (Figure 21b), but not at lower elevations, where using the same subset degrades both the accuracy and resolution of the estimates even if their precision is enhanced.

To provide a comprehensive quantitative overview of the elevation-dependent accuracy of individual Mohometers, an RMSE of calibration residuals specific to each predefined elevation bin is reported in Table 2. The most accurate mohometers featuring the lowest RMSE values in Table 1 are dominated by RMSE values lower than the average (0.37 km)—and thus are expected to offer better-than-average performances—in most of the elevation bins.

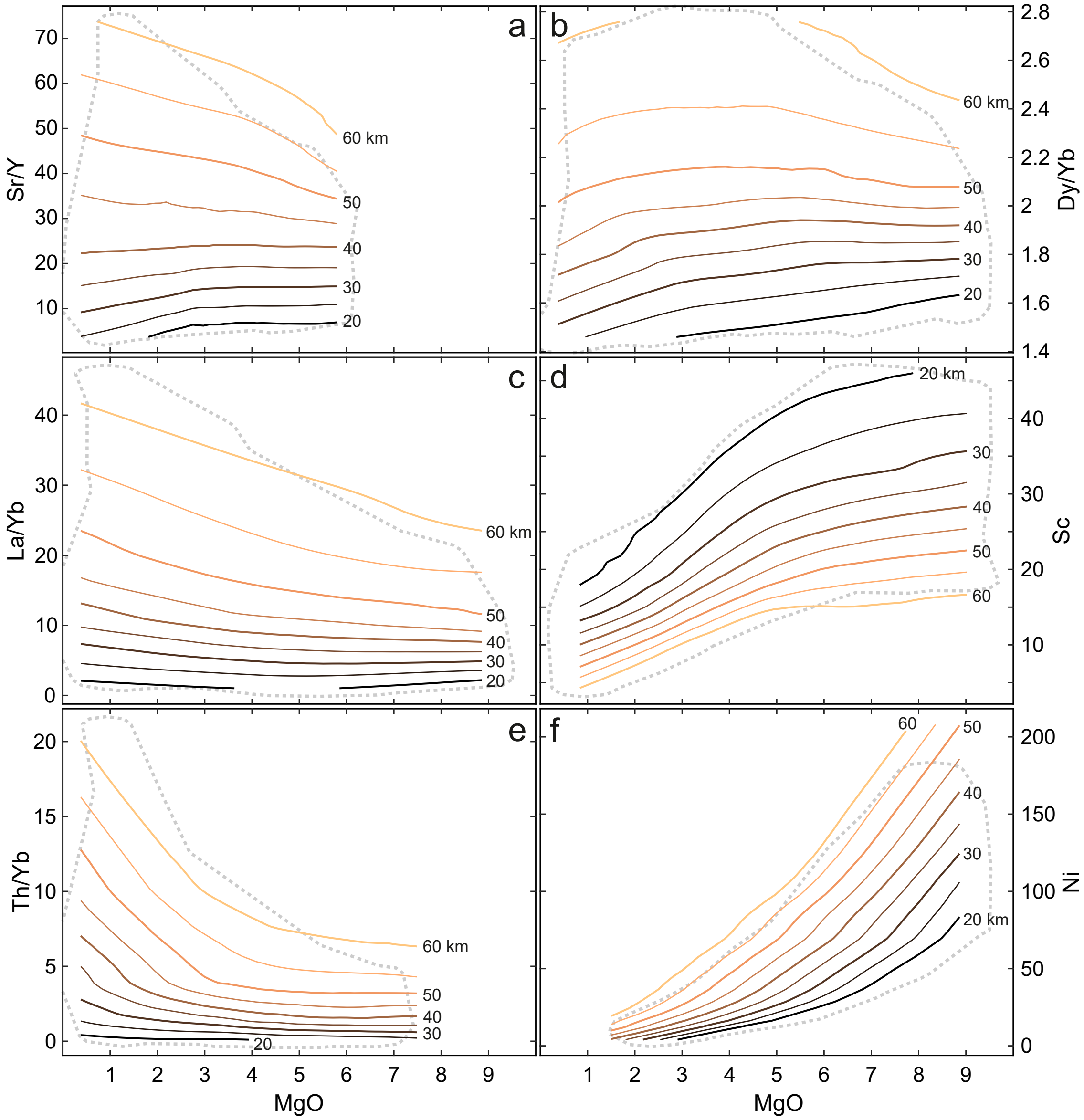

Figure 19. Representative mohometer model surfaces displaying effects of MgO content. Applicability envelopes of the models are shown as dotted lines (isolines extending beyond these are extrapolations). (a) Sr/Y and (b) Dy/Yb are examples of parameters insignificantly affected by differentiation; (c) La/Yb and (d) Sc show mild influences; MgO variations have most pronounced effects on the (e) Th/Yb and (f) Ni parameters. See text for details and further discussion.

5.5.3. La/Yb and Sr/Y Mohometer Models: A Comparison of New and Old Calibrations

Figure 22 compares the MgO-sensitive La/Yb and Sr/Y mohometer calibrations to models previously formulated for supra-subduction arcs (J. B. Chapman et al., 2015; Profeta et al., 2015; Sundell et al., 2021); the calibrations designed for collisional orogens (Hu et al., 2017) are also shown for reference. In spite of different approaches and number of datapoints involved in the calibrations, La/Yb-based arc mohometers generally agree (Figure 22a). In thinner crusts, where the effect of MgO variations is smaller, the differences between new and old calibrations are negligible. In thicker crusts, as the effect of MgO increases, predictions of the new calibrations for the primitive and evolved compositions diverge from the Profeta et al. (2015) and Sundell et al. (2021) estimates. For La/Yb = 25, for example, the new formulation predicts a clear increase in Moho depths from 52 to 58 km as MgO increases from 1 to 6 wt%, whereas both older models yield Moho depths of ca. 57 km. Compared to the ±10.8 km (2σ, residuals) calibration uncertainty of the Sundell et al. (2021) model, the overall uncertainty of new La/Yb model is only ±4.3 km.

In the case of Sr/Y, differences between models are greater (Figure 22b). In comparison to the linear A. D. Chapman et al. (2015) and J. B. Chapman et al. (2015) model, Moho depths predicted by the new formulation are greater at low Sr/Y and much shallower at high Sr/Y ratios; the crossover between the models occurs at Sr/Y = 35–40. Relative to the calibration of Sundell et al. (2021) aimed to improve the model of A. D. Chapman et al. (2015) and J. B. Chapman et al. (2015), the new model displays similar patterns, but predicts Moho depths that are variably greater, depending on both MgO and Sr/Y. In this case too, there is a notable difference between the uncertainties associated with the two models: ±10.8 km for the Sundell et al. (2021) model and ±6.2 km for the new Sr/Y model (2σ, residuals).

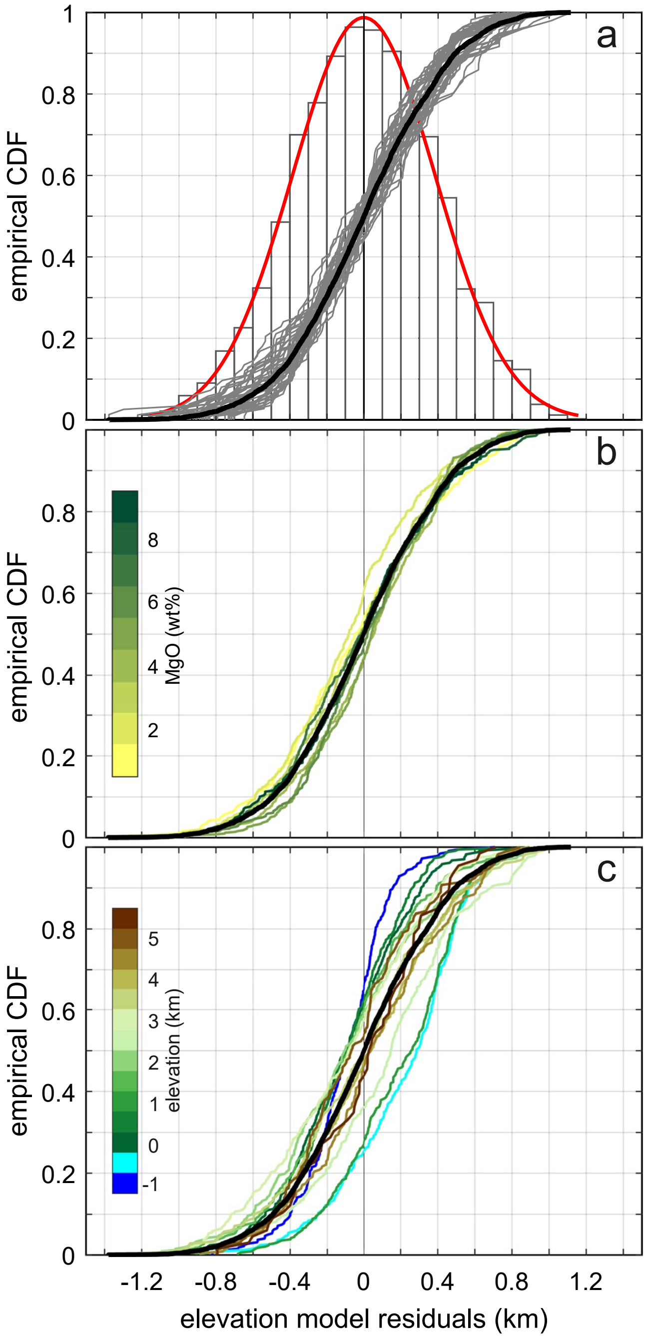

Figure 20. Distribution of elevation model residuals. (a) Histogram of residuals for all datapoints involved in the mohometer calibration indicates normal distribution around zero; normal density function (red curve) is given for reference. Empirical cumulative distribution function (CDF) curves are calculated for (a) residuals of individual mohometers shown in gray; (b) residuals sorted by the MgO bins used in calibrations; and (c) residuals sorted by the elevation bins used in calibrations. A CDF involving all residuals (bold black curve) is shown for reference in all diagrams.

5.6. Multielement Mohometry

There is no reason to consider that any particular mohometer can accurately reveal optimal Moho depth estimates when applied to unknown arc segments. One of the main reasons is that as shown in Section 5.5.2, the accuracy and resolving power of individual parameters may change with Moho depth. Another reason is that as discussed in Section 5.2.3 and illustrated in Figure 13, even though the global correlation between a chemical parameter and Moho depth is robust, arc segments with similar thicknesses may display notably different median (or mean) values for that parameter. The solution is to use multiple mohometers concomitantly to calculate a representative Moho depth as the median value of estimates predicted by individual Mohometers; the associated median absolute deviation is then a reliable measure of the pooled results' precision.

5.6.1. Data Processing: Selection and Combined Usage of Mohometers

Below, we present a five-step procedure (1–5) to obtain improved Moho depth estimates by combining results of the most suitable mohometers, given the available chemical data.

1. The first step in applying the new mohometers to an unknown arc segment consists of the statistical processing of the primary chemical data set that contains major and trace element analyses of samples assumed to represent similar crustal thicknesses from that segment. Using data sets spanning across too long time intervals of arc evolution or samples covering too long arc segments will poorly constrain Moho depths because crustal thickness varies over time and space. Following the protocols, including data filtering, used to derive the global arc median data set (Section 5.2), primary chemical data representing the unknown arc segment should be converted into a set of MgO-binned median values of the chemical parameters to be used in mohometry.
2. MgO-binned median parameters belonging to the arc segment of interest need to be filtered for outlier compositions that may affect the estimates. To eliminate such datapoints, two quantitative filters are simultaneously applied to each mohometer: its applicability envelope and the map of residuals associated with its REM, obtained by the inter- and extrapolation of the absolute value of individual residuals resulting from the model calibration (Figure 23a). The former filter is meant to discard data outside the calibration range as defined in Section 5.4.1, whereas the latter removes individual datapoints that fall in REM domains characterized by calibration residuals larger than an arbitrary cutoff value, $\varepsilon_{\max}$ (km). Imposing such a filter prevents datapoints associated with too large residuals from disqualifying a mohometer when evaluated in the next step (3).

3. A second filter excludes mohometer models that do not meet an arbitrary accuracy target defined in terms of elevation RMSE (km). To decide whether a mohometer is accurate enough to be considered further in the case of an unknown set processed through step 2, a virtual RMSE value is calculated from the remaining datapoints projected onto its map of residuals and compared to the minimum accuracy target, $rmse_{\max}$ (km), an arbitrary maximum limit; if the obtained virtual RMSE exceeds $rmse_{\max}$, the mohometer is rejected. This procedure is meant to preclude mohometers from being applied to those domains of their REM in which they are expected to be less accurate (see Table 2, Figure S1). Because even a single datapoint falling in a high-residual domain of the REM can elevate the virtual RMSE value above the cutoff value, tuning $e_{\max}$ and $rmse_{\max}$ iteratively may help use Mohometers otherwise compromised by such anomalous datapoints.
4. Using the REM of each parameter that passed the RMSE filter in step 3, first elevations, then with help of Equation 17, individual Moho depths are computed for each median datapoint that passed the filters in step 2. The dispersion of all individual Moho depth estimates resulting from mohometer X in different MgO bins, $H_{X(i)}$ ($i = 1\ldots9$), around their median value H_X, quantified as their median absolute deviation, MAD_X (km). This is taken to measure the uncertainty of that mohometer with respect to the involved data set and is used to assess the degree to which that data set is consistent with the employed REM and decide thereby whether the model is applicable. A small MAD_X value characterizing an unknown data set represents a near-ideal case in which included datapoints tightly align with an REM contour line, and thus the model can be successful, and the median Moho estimates robust (data set A in Figure 23b). A larger MAD_X value, on the other hand, may imply a variety of underlying causes. For instance, magmatic differentiation in arcs tends to produce similar differentiation trends in plutonic and volcanic suites at large scales (Keller et al., 2015) and thus, mohometer models relying on volcanic data are in principle applicable to plutonic samples as well. In practice, however, when applying these models at more limited scales, where data represent plutonic suites that include cumulates and lithologies affected by melt-rock reactions, various MgO–X trends may appear decoupled from their model equivalent, resulting in large MAD_X values. In such cases, it is possible that, for example, a dominantly tightly aligned set of datapoints also includes a few outliers degrading the applicability of the model (data set B in Figure 23b). Alternatively, a large MAD_X might be the effect of scattered datapoints loosely aligned with an REM contour (data set C in Figure 23b). Yet, another possibility is that the large MAD is caused by a datapoint trend oblique to all contour lines of the model (data set D in Figure 23b). Evaluating the degree of consistency between an REM and datapoint distribution patterns like those in Figure 23b and pinpointing the causes of mismatches may be important in some cases, particularly when the applicability of a mohometer is deemed essential (e.g., when the number of useful mohometers is limited by the available chemical data). In such cases, eliminating individual outlier datapoints or reconsidering the involved primary chemical data set (see step 1) may help improve the consistency of the examined median data set with the model. As illustrated by examples in Figure 23b, regardless of the patterns of datapoint distribution, a large MAD_X value associated with a set of individual Moho depths obtained with a mohometer across different MgO bins indicates inconsistency between data and model and warns against the application of that model to the examined case. Conversely, the smaller a MAD_X value is, the more appropriate the model is. Therefore, in order to exclude parameters associated with uncertainties considered too large, an arbitrary maximum MAD value, $mad_{\max}$ (km) (the accepted upper limit for individual mohometer uncertainty), is imposed; only parameters passing this filter (i.e., $MAD_X \leq mad_{\max}$) are used in the next step (5).

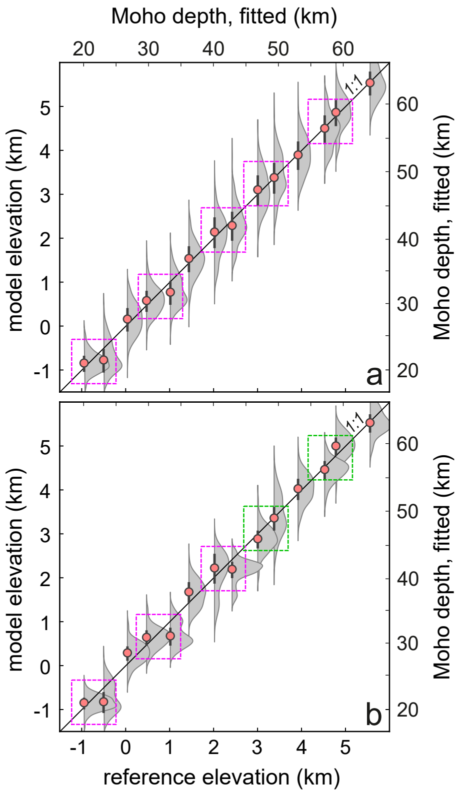

Figure 21. Median values and probability density distribution of elevation-binned model estimates of datapoints used in the calibrations versus medians of their binned reference elevations: (a) all mohometers and (b) 10 best mohometers (Table 1). Magenta boxes highlight elevation bins that are not resolved by the combined models; in these cases, error bars (median absolute deviations) associated with median estimates of the neighboring bins show significant overlap. Green boxes in panel (b) indicate elevation bins resolved by using only the 10 best mohometers. Note that the diagrams depict results computed for the complete MgO calibration ranges (Table 1). Restricted MgO ranges and/or applicable parameters, as would be the case of most arc segments targeted by mohometry (see discussion in Section 5.6), would result in different accuracies, precisions, and resolutions.

5. An overall Moho depth for the examined unknown arc, H_M, is computed as the median value of all individual Moho depth estimates obtained with mohometers with $MAD_X \leq mad_{\max}$. The smaller the median absolute deviation MAD_M associated with the overall Moho depth estimate H_M and larger the number of included mohometers is, the more robust is the final result.

Table 2

Elevation-Dependent Accuracy of Mohometers in Terms of RMSE (km) of Model Residues*

	midpoint of elevation bin (km)													
	–1	–0.5	0	0.5	1	1.5	2	2.5	3	3.5	4	4.5	5	5.5
La/Yb	0.19	0.33	0.29	0.29	0.46	0.23	0.44	0.37	0.13	0.30	0.27	0.21	0.44	0.14
Ce/Yb	0.19	0.31	0.28	0.33	0.41	0.35	0.45	0.44	0.15	0.29	0.24	0.19	0.33	0.16
Lu/Hf	0.14	0.44	0.18	0.14	0.34	0.51	0.46	0.27	0.27	0.35	0.16	0.31	0.25	0.19
Nd/Yb	0.21	0.34	0.26	0.21	0.42	0.38	0.43	0.40	0.25	0.25	0.31	0.21	0.40	0.17
La/Y	0.15	0.34	0.35	0.29	0.33	0.22	0.49	0.24	0.24	0.31	0.36	0.39	0.20	*0.31*
Nb/Y	0.12	0.31	0.24	0.26	0.37	0.36	0.48	0.45	0.20	0.65	0.28	0.20	0.09	*0.27*
Sm/Yb	0.26	0.36	0.25	0.28	0.29	0.34	0.43	0.50	0.51	0.14	0.19	0.21	0.42	0.07
Ce/Y	0.20	0.39	0.35	0.35	0.31	0.30	0.45	0.21	0.37	0.39	0.32	0.31	0.31	*0.39*
Nd/Y	0.20	0.42	0.37	0.29	0.35	0.36	0.37	0.40	0.24	0.32	0.40	0.31	0.25	*0.29*
Th/Yb	0.23	0.29	0.36	0.45	0.49	0.28	0.31	0.64	0.38	0.20	0.37	0.39	0.24	0.29
Hf	0.27	0.41	0.40	0.17	0.29	0.42	0.27	0.42	0.41	0.45	0.38	0.22	0.39	*0.44*
La/Sm	0.18	0.39	0.42	0.19	0.49	0.35	0.39	0.35	0.33	0.29	0.40	0.31	0.39	0.47
Gd/Yb	0.26	0.33	0.20	0.30	0.38	0.53	0.59	0.39	0.33	0.30	0.19	0.24	0.30	
Ba/V	0.17	0.29	0.40	0.26	0.36	0.21	0.34	0.33	0.50	0.27	0.33	0.58	0.41	*0.53*
MnO	0.17	0.38	0.34	0.38	0.15	0.27	0.29	0.43	0.55	0.38	0.38	0.47	0.55	0.42
K_2O	0.27	0.47	0.43	0.36	0.31	0.46	0.31	0.44	0.30	0.27	0.31	0.40	0.37	*0.17*
Zr/Y	0.19	0.39	0.26	0.13	0.37	0.17	0.45	0.46	0.32	0.39	0.48	0.48	0.22	
Ba/Sc	0.22	0.22	0.38	0.37	0.49	0.20	0.27	0.40	0.49	0.28	0.43	0.65	0.31	*0.39*
A	0.31	0.43	0.43	0.23	0.31	0.31	0.45	0.31	0.33	0.57	0.34	0.51	0.36	*0.48*
Nb/Yb	0.14	0.28	0.20	0.19	0.38	0.56	0.74	0.39	0.17	0.66	0.40	0.31	0.11	*0.28*
Dy/Yb	0.32	0.41	0.18	0.33	0.24	0.54	0.68	0.48	0.38	0.41	0.26	0.29	0.29	
A/CaO	0.23	0.39	0.37	0.14	0.25	0.33	0.37	0.46	0.58	0.47	0.33	0.54	0.31	*0.56*
Th/Y	0.22	0.42	0.43	0.36	0.50	0.43	0.49	0.35	0.37	0.40	0.40	0.50	0.21	*0.30*
CaO	0.26	0.38	0.47	0.36	0.30	0.26	0.46	0.46	0.70	0.17	0.36	0.45	0.36	*0.33*
Rb	0.15	0.49	0.32	0.52	0.13	0.41	0.42	0.64	0.31	*0.68*	0.44	0.50	0.35	*0.27*
Ni/Sc	0.37	0.29	0.27	0.25	0.45	0.31	0.35	0.41	0.52	0.41	0.42	0.38	0.57	
Sc	0.36	0.54	0.27	0.18	0.53	0.28	0.53	0.29	0.55	0.36	0.59	0.42	0.46	0.38
Ga	0.35	0.29	0.50	0.41	0.59	*0.04*	0.50	0.41	0.54	0.49	0.53	0.50	0.29	
Pb	0.15	0.38	0.38	0.34	0.28	0.51	0.49	0.77	0.54	0.38	0.27	0.35	0.49	
Ba	0.31	0.46	0.33	0.66	0.32	0.30	0.25	0.47	0.21	0.37	0.49	*0.22*	0.66	*0.53*
U	0.17	0.43	0.47	0.50	0.38	0.68	0.34	*0.56*	0.34	0.76	0.46	0.41	0.54	*0.32*
FeO_t	0.27	0.56	0.35	0.43	0.40	0.41	0.33	0.43	0.62	0.36	0.57	0.43	*0.11*	*0.11*
Cr/Sc	0.39	0.32	0.36	0.34	0.30	0.28	0.33	0.32	0.69	0.62	0.45	0.64	0.54	*0.43*
Ni	0.39	0.43	0.43	0.30	0.25	0.32	0.33	0.48	0.41	0.26	0.44	*0.47*		
Sr/Y	0.20	0.45	0.38	0.15	0.66	0.60	0.48	0.20	0.25	0.65	0.54	0.52	0.22	*0.31*
Sr	0.23	0.48	0.41	0.26	0.48	0.43	0.71	0.44	0.46	0.35	0.37	*0.58*	0.51	*0.25*
Zr/Ti	0.25	0.45	0.22	0.10	0.26	0.46	0.55	0.76	0.42	0.66	0.42	0.46		
Ni/V	0.41	0.32	0.28	0.31	0.51	0.36	0.27	0.69	0.68	0.55	0.15	*0.55*	*0.72*	
Cr/V	0.39	0.50	0.24	0.25	0.26	0.36	0.42	0.48	0.60	0.54	0.65	*0.54*	*0.42*	*0.42*
Co	0.26	0.41	0.58	0.43	0.21	0.60	0.56	0.35	0.61	0.53	*0.10*	*0.26*	*0.64*	
Cr	0.35	0.53	0.33	0.43	0.43	0.38	0.53	0.42	0.62	0.93	0.45	*0.35*	0.59	*0.41*

best
🟩
🟩
🟩
⬜
🟥
🟥
🟥
worst

**RMSE values obtained from less than three MgO bins are shown in italics. Gray bins indicate lack of data*

The above procedure is computationally intensive and refining the obtained results may require several iterations of steps 2–5. To facilitate these computations, we developed GAME (Geochemical Arc Moho Estimator), a user-friendly MATLAB® app, which is available at https://osf.io/bmn8y/, as well as Supporting Information S2 attached to this paper.

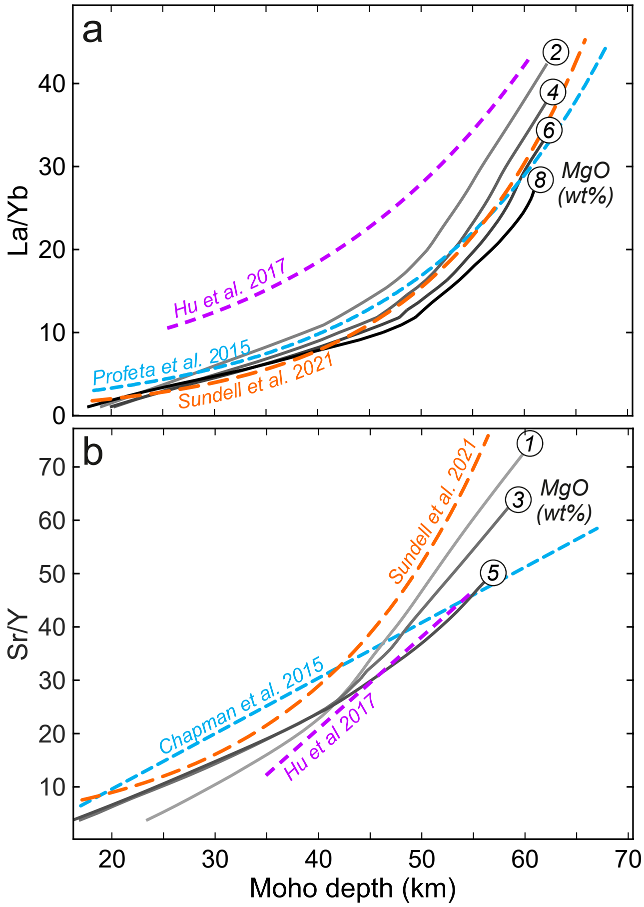

Figure 22. MgO-dependent mohometer models versus previous calibrations: (a) La/Yb and (b) Sr/Y. New models are shown as continuous lines labeled as a function of MgO (wt%); dashed lines represent previous models as labeled. Since the older models rely on total crustal thickness ($H^{tot} = H + h$) instead of Moho depth relative to sea level (H), used in the new approach, in order to allow a meaningful comparison, their expressions Equations (2–5, 7 and 8) were converted into La/Yb–H and Sr/Y–H formulas with Equation 17. See discussion in the text.

5.6.2. Testing Mohometry on Modern Arcs With Known Moho Depths

Extensively sampled modern arcs with well-constrained Moho depths represent a way to evaluate the capabilities and limitations of the above-presented multiparameter mohometry method and the newly calibrated mohometer models it relies on. Although the chemical data set underpinning these models was built using data from modern arcs, for testing purposes, the included arc segments can be treated as unknowns. The reason is that in contrast with previous approaches, in this case, the individual segments themselves do not represent datapoints on which all calibrations simultaneously rely on. Instead, each mohometer model was calibrated separately by fitting an elevation-binned global arc data set in which elevation bins are populated with data sourced in diverse arc segments, and data from individual arc segments are typically distributed into two or more elevation bins (Figure 12b). In order to assess the multiparameter mohometry method, here we examine two such arc segments with the help of GAME.

5.6.2.1. The New Hebrides–Vanuatu Arc

The New Hebrides–Vanuatu arc of the Southwestern Pacific developed in response to subduction of the Australian plate beneath the Fiji plateau. For the central segment of this arc, Coudert et al. (1984) obtained a Moho depth of 27 ± 2 km by applying two different methods (travel-time plots for remote earthquakes and time-term analysis on sets of earthquakes) to data obtained from a local seismograph network distributed along the arc. New Hebrides–Vanuatu belongs to a group of arc segments used for calibration, which has comparable crustal thicknesses (25–35 km) and elevations (0–1 km) (see Figures 12b and 14), but formed in diverse subduction settings and crustal conditions. Hence, we use the example of New Hebrides–Vanuatu to evaluate how well a "correct answer" constrained by seismic methods is obtained by the different mohometers.

We used 440 New Hebrides–Vanuatu samples from the global arc data set (Section 5.2.1) to compute MgO-binned median values of the chemical parameters relevant to mohometry (step 1, Section 5.6.1). In order to obtain estimates with all 41 parameters, we calculated the overall median Moho depth estimate H_M from chemical parameters that populate at least four different MgO bins containing five or more samples each. By setting $\varepsilon_{\max} = 1.5$ km (step 2), $rmse_{\max} = 1$ km (step 3), and a generous $mad_{\max} = 10$ km (step 4), we obtained $H_M \pm MAD_M = 27.4 \pm 3.7$ km based on all 41 parameters (299 median datapoints), which is in excellent agreement with the seismically constrained 27 ± 2 km of Coudert et al. (1984). In order to evaluate the sensitivity of H_M to parameters that yield the least robust estimates in the examined case, next we decreased $\varepsilon_{\max}$ to 0.75 km, $rmse_{\max}$ to 0.5 km, and $mad_{\max}$ to 3.5 km. Though 58 median datapoints representing 9 parameters including Sr/Y are filtered out this way, the overall median Moho depth estimate remains essentially the same, $H_M = 27.1$ (±3.2) km. The results of the exercise shown in Figure 24 reveal that the resistance of H_M to outliers is supported by a large number of mohometers yielding very similar estimates.

The peaks of the probability density distribution curves obtained for the employed median datapoints using the two different setups discussed above (right panel in Figure 24) nearly coincide with H_M, further corroborating the robustness of the estimate. Inset in Figure 24 depicts the extent to which H_M, MAD_M, and the peak of the probability density distribution curve are influenced by the number of applicable mohometers when limited by $mad_{\max}$ alone. In the case of the New Hebrides–Vanuatu arc, $mad_{\max}$ has negligible effect on H_M, MAD_M, and probability density distribution peak value, indicating that the obtained median Moho depth estimate is not significantly influenced by parameters less applicable to the evaluated data set (see step 4). We note that the geophysically constrained Moho depth is reasonably predicted by the La/Yb parameter (30.9 ± 1.8 km), but considerably overestimated by Sr/Y (39.8 ± 3.9 km).

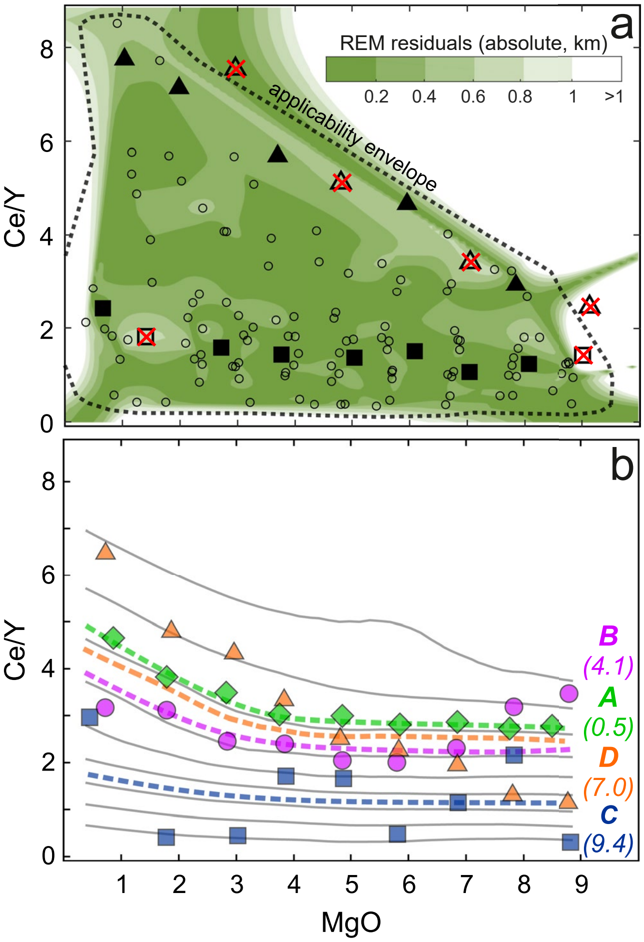

Figure 23. (a) Filtering Ce/Y-MgO median data sets using the applicability envelope and map of residuals associated with reference elevation model (REM) of the Ce/Y mohometer (calibration datapoints are shown as small empty circles). Crossed-out datapoints in the two example data sets (squares and triangles) are rejected because they fall either outside the applicability envelope or into Ce/Y–MgO regions in which the absolute values of REM residuals are larger than an arbitrary cutoff value, $\varepsilon_{\max}$ (here $\varepsilon_{\max} = 0.6$ km). A virtual RMSE is computed for each data set from REM residuals in the locations of the remaining datapoints (black-filled symbols); the mohometer is rejected if this value is larger than an arbitrary $rmse_{\max}$ value. (b) Evaluating the consistency of various unknown Ce/Y–MgO median data sets (A–D) with the corresponding REM (gray contour lines). $H_{Ce/Y}$ median Moho estimates calculated for the different data sets are plotted as correspondingly colored dashed lines; median absolute deviations ($MAD_{Ce/Y}$, km) are shown as bracketed values. Data set A (green diamonds) shows near-ideal consistency with the model (small $MAD_{Ce/Y}$ value); data sets B–D show various degrees of inconsistency with the model (large $MAD_{Ce/Y}$ values). The mohometer is rejected for data sets having $MAD_{Ce/Y}$ larger than arbitrarily set $mad_{\max}$. See text for further details and discussion.

5.6.2.2. *The Andean Southern Volcanic Zone*

The SVZ of the Andean arc is characterized by variable relief and crustal thicknesses beneath the volcanic front (Hildreth & Moorbath, 1988). Recent 3D density models of the Andean subduction zone obtained via forward modeling the Bouguer anomaly and constrained by receiver function and teleseismic reflection data (Tassara & Echaurren, 2012; Tassara et al., 2006) suggest that SVZ elevations and Moho depths progressively decrease from 5 to 50 km, respectively, in the north to less than 1 and 35 km in the south (Tassara & Echaurren, 2012; Tassara et al., 2006). Therefore, SVZ is useful for testing the resolving power of multi-parameter chemical mohometry. Here, we use 1498 SVZ samples extracted from the global arc data set (Section 5.2.1) to assess how variations in crustal thickness are captured by two different approaches.

In a first approach, we evaluate how well the median Moho depths of arbitrarily defined segments of SVZ can be distinguished. Because samples are unevenly distributed across the Northern, Transitional, Central, and Southern subzones of SVZ (e.g., Hickey-Vargas et al., 2016) (Figure 25a), using these segments as such is not appropriate. Instead, we divided SVZ at latitude 37°S into a northern segment (N) that comprises the Northern and Transitional subzones (734 samples) and a southern segment (S) that includes the Central and the northernmost Southern subzone (764 samples). Reference median Moho depths of the two segments, computed by applying Equation 17 to the elevation of individual sample locations, are 40.7 ± 1.8 km (N) and 34 ± 2.2 km (S).

Using chemical parameters that populate at least five different MgO bins containing five or more samples each, and applying $\varepsilon_{\max} = 0.5$ km and $rmse_{\max} = 0.5$ km, we obtained Moho depths that distinguish the two segments for all $mad_{\max} < 10$ km (Figure 25b). For example, using $mad_{\max} = 5$ km, 37 parameters involving 217 median datapoints produced $H_M = 41.6 \pm 3.5$ km in the northern segment, and 38 parameters (268 datapoints) yielded $H_M = 29.9 \pm 2.1$ km for the southern segment (Figure 25c). While the reference Moho depth is well reproduced in the north, most chemical mohometers underestimate it by ~4 km in the south.

In the second approach, we evaluate the ability of multiparameter mohometry to reproduce the continuous along-strike variation of Moho depths characterizing the SVZ. To do so, we computed an individual Moho depth for each sample as the median estimate of all applicable mohometers that pass the $\varepsilon_{\max} = 0.5$ km filter. Median Moho depths obtained on samples from the same locality display large differences (Figure 25d), which are not surprising, given that individual samples are not ideal for such purposes (Figure 16a). Nevertheless, they qualitatively reproduce the southward crustal thinning trend reflected in surface topography and constrained by geophysical means (Laske et al., 2013; Tassara & Echaurren, 2012; Tassara et al., 2006). A much clearer picture emerges, however, when a LOWESS smoothing similar to that used in mohometer calibration is applied to the individual estimates (Figure 26d). The smoothed median Moho trend is undistinguishable from the reference isostatic Moho depth (converted from arc elevations) over the entire SVZ except between 38°S and 40°S dominated by data from the Llaima and Villarrica stratovolcanoes. Here, multiparameter mohometry underestimates the reference by ~5 km and thus cannot distinguish Moho depths south of latitude 38°S.

In both approaches, discrepancies between mohometric estimates and the elevation-based isostatic Moho depth used as reference are likely related to accuracy and resolution issues discussed in Section 5.5.2, which

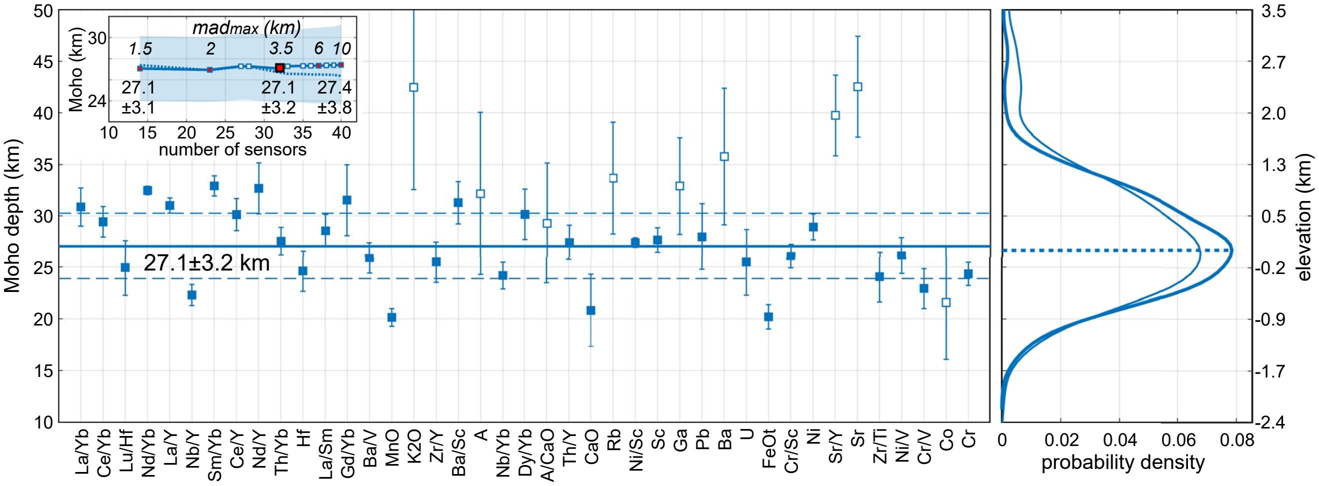

Figure 24. Chemical mohometry of the New Hebrides–Vanuatu arc. Left panel: $H_X \pm MAD_X$ estimates of individual mohometers. Estimates shown as filled symbols were obtained using $\varepsilon_{\max} = 0.75$ km, $rmse_{\max} = 0.5$ km, and $mad_{\max} = 3.5$ km; $H_M \pm MAD_M$ are shown as continuous and dashed horizontal lines, respectively. Empty symbols indicate additional estimates that are obtained by relaxing $\varepsilon_{\max}$, $rmse_{\max}$, and $mad_{\max}$ to 1.5, 1, and 10 km, respectively. Right panel: probability density distribution of individual estimates obtained in the two cases (thicker curve corresponds to the restricted setup); dotted line marks the peak of the curves. Inset in left panel shows the effect of $mad_{\max}$ on $H_M \pm MAD_M$ (continuous line and shaded band), and peak of probability density distribution (dotted line) at $\varepsilon_{\max} = 0.75$ km and $rmse_{\max} = 0.5$ km. Selected $mad_{\max}$ (in italics) and resulting $H_M \pm MAD_M$ values are shown for reference. For example, setting $mad_{\max}$ to 1.5 km retains 14 parameters, which yield $H_M \pm MAD_M = 27.1 \pm 3.1$ km. Further details and discussion in text.

lead to underestimated reference elevations by ~0.25–0.3 km (~1.7–2 km in Moho depth) in certain elevation/Moho depth intervals (Figure 21a). Whether such discrepancies are acceptable depends on the purpose of mohometry. We note that reference Moho depths tend to increasingly underestimate the geophysically constrained models toward the south of SVZ by up to 6–7 km, whereas the geophysical models themselves yield Moho estimates that differ by similar amounts in the north. Given the ~5 km uncertainty of the geophysically determined Moho depths (e.g., Tassara & Echaurren, 2012), the resolution of mohometric estimates is satisfactory for the SVZ.

5.6.3. Application to Paleoarcs: The Northern Peninsular Ranges Batholith

The Peninsular Ranges Batholith (PRB) represents the southernmost intrusive system of the arc magmatism that developed along the western margin of North America in response to the subduction of the Farallon oceanic plate during the Mesozoic. It is the southern continuation of the Sierra Nevada batholith (Ducea, 2001); its northernmost part is located in southern California (USA) and continues southward into Baja California (Mexico) all the way to the southern tip of the Baja peninsula. The mid- to late Cretaceous northern part of PRB in southern California, one of the world's most systematically sampled batholithic exposure (Baird et al., 1979; Kistler et al., 2003), is characterized by a pronounced East-West dichotomy: its eastern domain (E-PRB) formed on the Paleozoic North American continental margin, whereas its western domain (W-PRB) developed in island arc terranes accreted to the continent during the Jurassic (Busby, 2004; Kistler & Anderson, 1990). Mid- to late Cretaceous arc magmatism migrated eastward as the shallowing subduction angle of the Farallon plate led to the compression and thickening of the overriding North American continental margin (Busby, 2004; Silver & Chappell, 1988; V. R. Todd et al., 1988). The systematic differences between the two domains are recognized as contrasts in the composition and Sr, Nd, and O isotopic signature of their plutons and manifest in the composition, metamorphic grade, and age of host lithologies (e.g., Baird et al., 1979; Gastil, 1975; Gromet & Silver, 1987; Kistler et al., 2003; Lee et al., 2007; Tulloch et al., 2003; V. Todd et al., 1988; Wetmore et al., 2003). New major and trace element data (Lee et al., 2007) obtained on the sample collection of Baird et al. (1979) allow us to evaluate crustal thickness variations across the PRB. To calculate median Moho depths for E-PRB and W-PRB, we separated the 287 samples based on the E–W boundary of Kistler et al. (2003) that relies on O isotopic differences between the two domains (Figure 26a).

The W-PRB domain (127 samples after filtering) is characterized by a broad spectrum of lithologies from primitive gabbros to granitoids. Applying $\varepsilon_{\max} = 0.5$ km and $rmse_{\max} = 0.5$ km to chemical parameters that

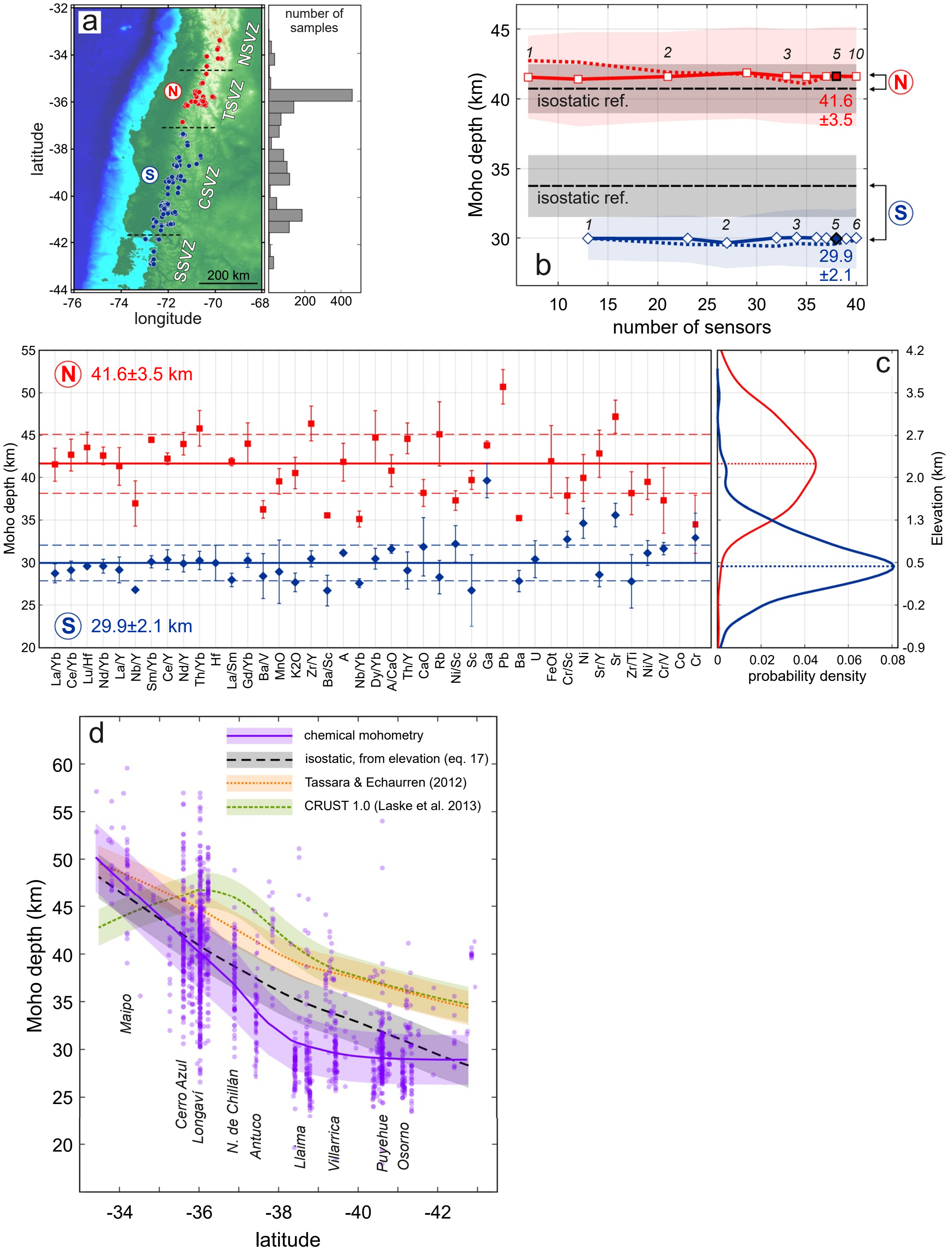
a
NSVZ
TSVZ
CSVZ
SSVZ
N
S
200 km
latitude
longitude
-32
-34
-36
-38
-40
-42
-44
-76
-74
-72
-70
-68
number of samples
200
400
b
Moho depth (km)
number of sensors
isostatic ref.
41.6
±3.5
29.9
±2.1
1
2
3
5
6
10
45
40
35
30
15
20
25
N
S
41.6±3.5 km
29.9±2.1 km
Moho depth (km)
La/Yb
Ce/Yb
Lu/Hf
Nd/Yb
La/Y
Nb/Y
Sm/Yb
Ce/Y
Nd/Y
Th/Yb
Hf
La/Sm
Gd/Yb
Ba/V
MnO
K2O
Zr/Y
Ba/Sc
A
Nb/Yb
Dy/Yb
A/CaO
Th/Y
CaO
Rb
Ni/Sc
Sc
Ga
Pb
Ba
U
FeOt
Cr/Sc
Ni
Sr/Y
Sr
Zr/Ti
Ni/V
Cr/V
Co
Cr
c
probability density
Elevation (km)
0
0.02
0.04
0.06
0.08
4.2
3.5
2.7
2.0
1.3
0.5
-0.2
-0.9
55
50
25
20
d
chemical mohometry
isostatic, from elevation (eq. 17)
Tassara & Echaurren (2012)
CRUST 1.0 (Laske et al. 2013)
Moho depth (km)
60
Maipo
Cerro Azul
Longaví
N. de Chillán
Antuco
Llaima
Villarrica
Puyehue
Osorno
-34
-36
-38
-40
-42
latitude

Figure 25.

populate at least five different MgO bins containing five or more samples each, we obtained H_M of ~30 km for all $mad_{\max}$ <10 km (Figure 26b); limiting $mad_{\max}$ to lower values decreases MAD_M, but does not affect H_M. For example, setting $mad_{\max} = 5$ km (Figure 26c) produced $H_M = 29.5 \pm 2.4$ km based on 24 mohometers involving 154 datapoints. In comparison, E-PRB (156 samples after filtering), is represented by granitoids (MgO <3 wt%). Because samples populate only three MgO bins, the $\varepsilon_{\max}$–$rmse_{\max}$–$mad_{\max}$-based mohometer selection is statistically less meaningful. Nevertheless, in order to eliminate outliers but still retain sufficient datapoints, we used chemical parameters that populate all three MgO bins containing two or more samples each and imposed $\varepsilon_{\max} = 0.55$ km and $rmse_{\max} = 0.5$ km. H_M resulting for E-PRB is ~49 km regardless of $mad_{\max}$ (Figure 26b); varying $\varepsilon_{\max}$ and $rmse_{\max}$ added or removed parameters but did not change the outcomes. Using $mad_{\max} = 5$ km, 19 parameters involving 57 datapoints yielded $H_M = 49.4 \pm 3.1$ km (Figure 26c), which is much deeper than for W-PRB. This difference is consistent with the scenario of significant crustal thickening accompanying the eastward migration of the volcanic front (Gromet & Silver, 1987) although our estimates cannot preclude the possibility that arc magmatism in the east affected an already thickened continental margin.

In order to gain further insight into the crustal thickness contrast between E-PRB and W- PRB, we adopted the same approach as for the Andean SVZ (Section 5.6.2.2): using Moho depth estimates obtained for all samples computed from all applicable mohometers satisfying $\varepsilon_{\max} = 0.5$ km, we constructed a LOWESS-smoothed model trend of the east-west Moho depth variations (Figure 26d). According to this, the W-PRB is characterized by constant ~30 km Moho depths, which increase eastward across the suture zone (116.8°–117°W) to ~45 km on the western margin of E-PRB and then continue to increase more gently to 55 km on its eastern part near the San Andreas Fault Zone. Remarkably, the east-west crustal thickness variation across PRB mimics the smoothed distribution of intrusion ages (Figure 26e) obtained on the same samples (Kistler et al., 2003).

Finally, the dense grid sampling of the PRB offers an unprecedented opportunity to use multiparameter mohometry for reconstructing the paleotopographic surface of the Cretaceous arc (Figure 27a) and compare it to modern topography (Figure 27b). This shows how the modern relief, although greatly reduced in elevation over the elapsed >80 Ma, inherits the main features of the isostatically balanced topography developed along the Cretaceous convergent margin.

5.7. Mantle and Crustal Contributions to the Observed Composition–Moho Depth Correlations

As discussed in Section 3, explanations regarding the correlation between Moho depth and arc magma chemistry can be ascribed to two opposing views. One is that magma composition is controlled by the pressure of differentiation at the bottom of crust, thereby reflecting its thickness (most researchers take this view); the other suggests that magma composition is dictated by composition and melting degree of the mantle wedge modulated by the thickness of the overriding plate (Langmuir and collaborators). Since the two interpretations refer to different chemical parameters and imply different intervals of the differentiation spectrum, they are not necessarily mutually exclusive: both proposed models may be valid, yet have different weights in the various composition–Moho depth correlations. In fact, the diversity of effects differentiation has on the various mohometers (presented in Section 5.5.2) strongly suggests that no single petrogenetic mechanisms can account for the anatomy of all X–MgO–H surfaces. While a thorough analysis of the possible petrogenetic causes of the X–MgO–h correlations identified in the global arc median data set and the differentiation-dependent mohometer models they underpin is beyond the scope of this review, below we provide a first-order assessment of the relative

Figure 25. Chemical mohometry of the Andean Southern Volcanic Zone (SVZ). (a) Sample locations and grouping into northern (N) and southern (S) segments; NSVZ, TSVZ, CSVZ, and SSVZ stand for Northern, Transitional, Central, and Southern subzones; histogram shows along-axis sample distribution. (b) The effect of $mad_{\max}$ on H_M, MAD_M and peak probabilities using $\varepsilon_{\max} = 0.5$ km and $rmse_{\max} = 0.5$ km in both (N) and (S); median values and median absolute deviations of reference Moho depths are shown as gray-dashed lines and shaded bands, respectively; (c) $H_X \pm MAD_X$ estimates of individual mohometers and $H_M \pm MAD_M$ (left panel) and corresponding probability density distributions (right panel) obtained for $mad_{\max} = 5$ km [symbols and labeling in panels (b and c) same as in Figure 24]; (d) continuous along-strike Moho depth trend obtained by chemical mohometry compared to Moho depth variations determined by other means. All curves were generated by Locally Weighted Scatterplot Smoothing (LOWESS) smoothing; the mohometric curve relies on median Moho depths computed for individual samples as described in the text (purple dots); the other curves rely on the 0.14° × 0.14° Global Multi-Resolution Topography model, CRUST 1.0, and Tassara and Echaurren (2012) models, respectively, which were interpolated along a 100-km-wide swath covering the SVZ volcanic front using a horizontal grid spacing of 10 × 10 km. Uncertainty intervals represent median absolute deviations relative to the LOWESS smoothed curves.

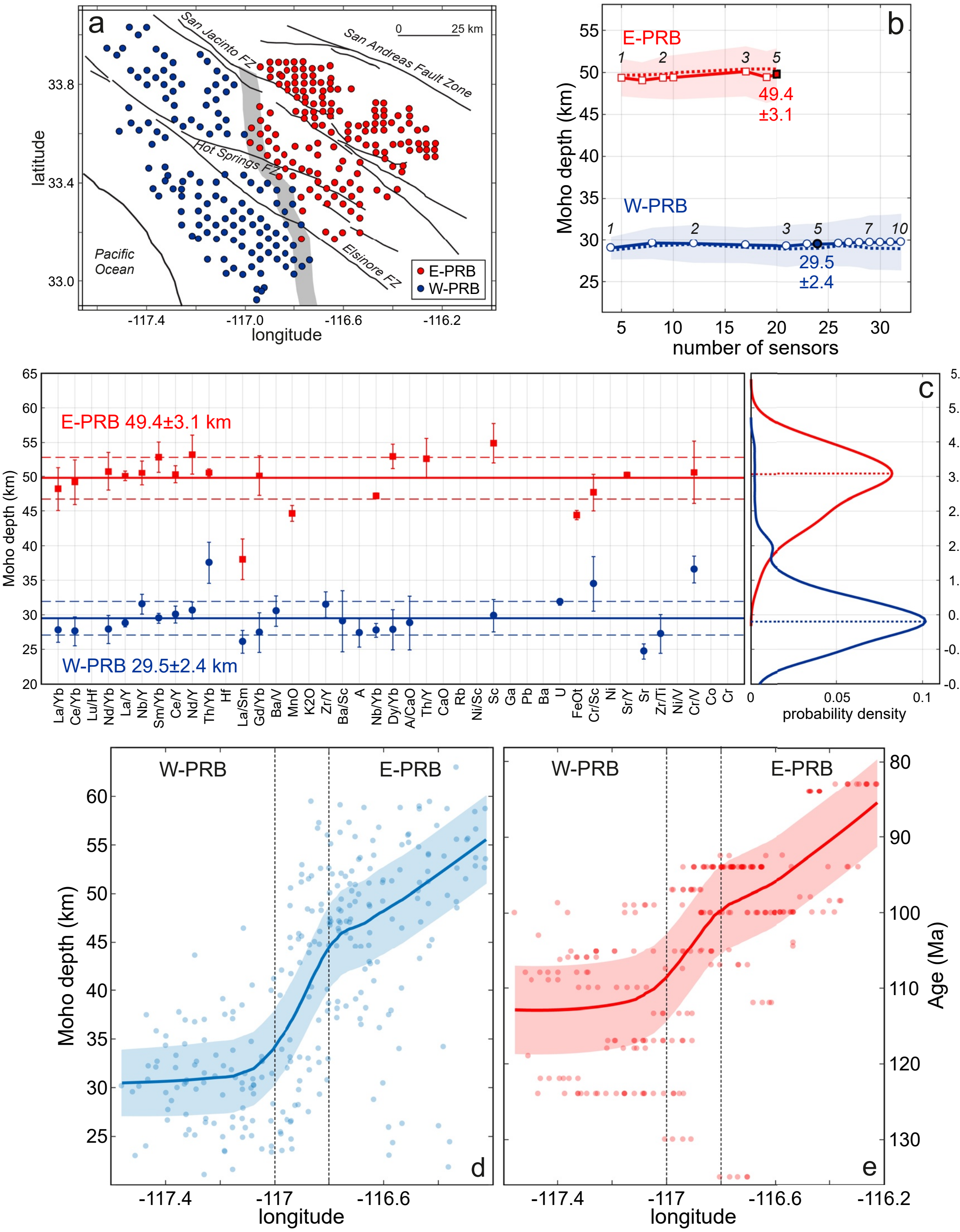

Figure 26. Chemical mohometry of the northern Peninsular Ranges Batholith (PRB). (a) Tectonic sketch with sample locations (modified after Kistler et al., 2003); suture zone delimiting E-PRB and W-PRB is shown as gray band; (b) the effect of $mad_{\max}$ on H_M, MAD_M, and peak probability (W-PRB: $\varepsilon_{\max} = 0.5$ km, $rmse_{\max} = 0.5$ km; E-PRB: $\varepsilon_{\max} = 0.55$ km, $rmse_{\max} = 0.5$ km); (c) $H_X \pm MAD_X$ estimates of individual mohometers and $H_M \pm MAD_M$ in E-PRB and W-PRB (left panel) and corresponding probability density distributions (right panel) obtained for $mad_{\max} = 5$ km [symbols and labeling in panels (b and c) same as in Figure 24]. (d) Continuous east-west Moho depth trend estimated by chemical mohometry: The Locally Weighted Scatterplot Smoothing (LOWESS)-smoothed curve is obtained using the median Moho depths computed for individual samples (blue dots) as described in the text. (e) LOWESS-smoothed east-west distribution of intrusion ages (red dots, Kistler et al., 2003). Uncertainty intervals associated with the curves in panels (d and e) represent median absolute deviations relative to the LOWESS smoothed curves; vertical dotted lines approximate the position of the suture zone shown in panel (a).

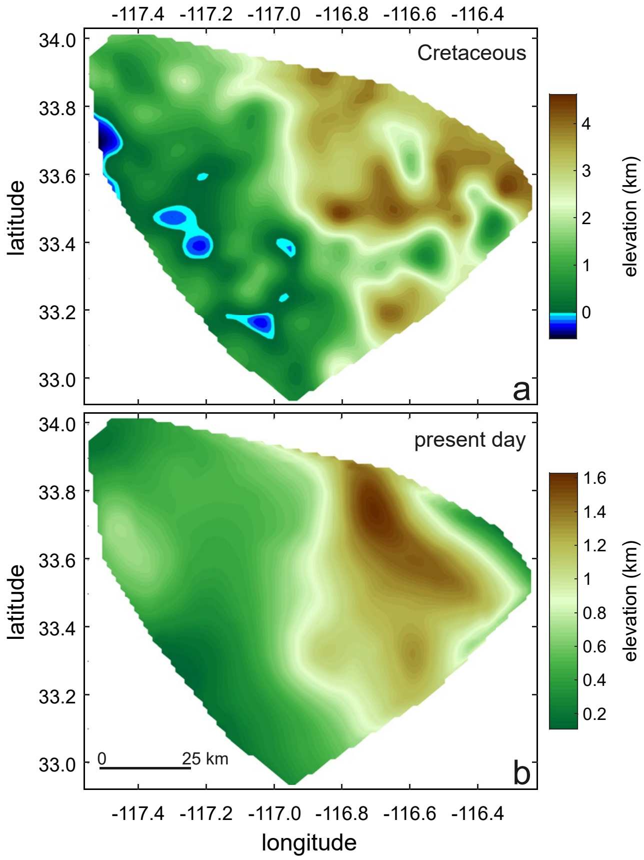

Figure 27. Comparison of (a) reconstructed Cretaceous paleotopography of the northern Peninsular Ranges in northern Baja California and southernmost California with (b) present-day topography of the same region. The Cretaceous paleosurface was obtained by a slightly smoothed interpolation of paleoelevations in each of the Peninsular Ranges Batholith sampling locations (Figure 26a) calculated as the median value of mohometric estimates passing the $\varepsilon_{\max} = 0.5$ km filter. Present-day surface was generated by interpolating the 0.14° × 0.14° Global Multi-Resolution Topography model over the sample locations used in (a). Note the different elevation scales for the two images.

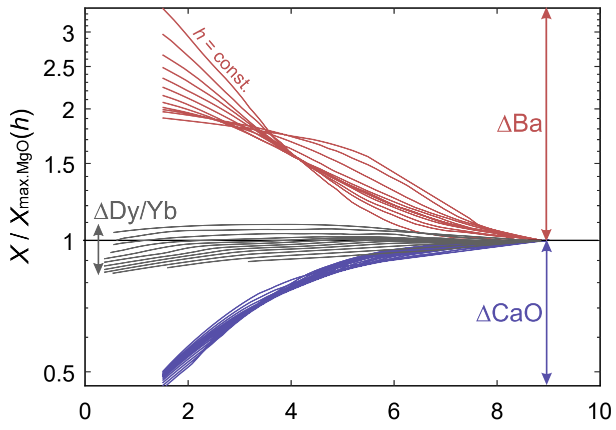

Figure 28. Definition of total variability interval ΔX of $X/X_{\mathrm{max.MgO}}(h)$, illustrated for compatible CaO, incompatible Ba, and neutral Dy/Yb. All quantities are defined in the text.

contribution of mantle and crustal processes to these correlations, which may aid future research.

First, we note that model residuals do not increase with MgO (Figure 17a, Figure S1), implying that composition–crustal thickness correlations defining that the mohometers do not degrade notably toward the primitive end of the differentiation spectrum. Due to strong correlations at MgO >~8 wt%, the majority of mohometers are applicable to primitive basalts not affected significantly by crustal processes (see Table 1 for applicability ranges). Therefore, it is reasonable to assume that in all these cases, correlations originate in the mantle wedge and reflect the effect of crustal thickness on the extent of mantle melting as argued by Turner and Langmuir (2015a, 2015b) and Turner et al. (2016). For a few mohometers (e.g., Ga, Rb, Th/Yb, and Sr/Y), correlations at MgO >7–8 wt% are either not strong enough or not supported by sufficient data to be used for model calibration. In these cases, the contribution of mantle processes to the strong *X*–*H* correlation developed at lower MgO values is uncertain, but probably small.

Next, we compare the contribution of crustal differentiation processes to the Moho depth-dependent variability of the chemical parameters supporting the mohometer models, expressed relative to their variability at high MgO. This means that for a given Moho depth, increasing or decreasing values of a chemical parameter with decreasing MgO indicates variable contributions of intracrustal differentiation, whereas a parameter remaining constant across its MgO range of applicability can be considered unaffected by magma differentiation. As a general rule, for a given Moho depth, the concentrations of elements compatible during magma differentiation are expected to decrease, whereas the concentrations of incompatible elements will increase with decreasing MgO (we note though that in the case of ratios, such a distinction is arbitrary in the sense that it depends on the relative compatibility of elements in the numerator and denominator, e.g., La/Yb is incompatible, while Yb/La is compatible). Accordingly, the more compatible or incompatible the overall behavior of a Moho parameter is, the more affected by magma differentiation the *X*–*h* correlations underlying it can be expected to be.

To obtain results that allow a more quantitative comparison of how crustal differentiation influences the different models, using the *X*–MgO–*h* model surfaces, we calculate $X/X_{\mathrm{max.MgO}}(h)$, the value of each chemical parameter *X* along various *h* contour lines within its applicability envelope, normalized to its value at maximum MgO concentration on these contour lines, and define ΔX as the total variability interval of $X/X_{\mathrm{max.MgO}}(h)$. As illustrated in Figure 28, the total variability interval obtained for compatible CaO is below unity, ΔCaO = [0.46, 1], while for incompatible Ba is above unity, ΔBa = [1, 3.40]. In comparison, the Dy/Yb ratio is approximately neutral (i.e., neither compatible nor incompatible), being characterized by a narrow variability interval around unity, ΔDy/Yb = [0.84, 1.10].

Total variability intervals obtained for the calibrated mohometers are compared in Figure 29. Mohometers based on highly incompatible elements and ratios having such elements in the numerator result in the largest $X/X_{\mathrm{max.MgO}}(h) > 1$ deviations and the widest ΔX intervals (e.g., ΔTh/Y = [0.85, 15.57], ΔBa/Sc = [0.94, 13.15]), which indicate that their Moho depth-dependent variability reflects intracrustal differentiation of magmas. In comparison, mohometers relying on moderately incompatible chemical parameters display narrower ΔX intervals (e.g., ΔCe/Y = [0.89, 1.84],

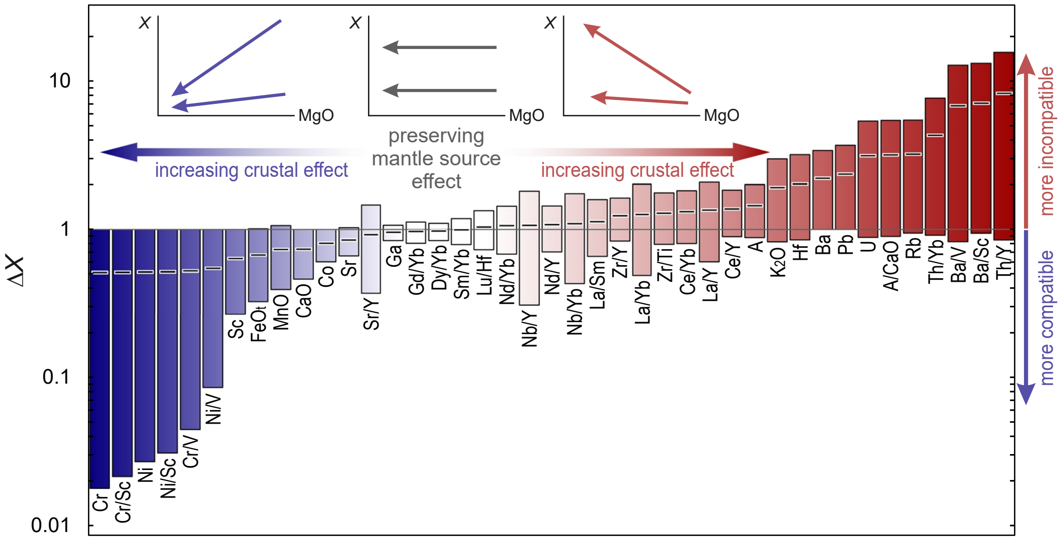

Figure 29. Total variability intervals of mohometers, Δ*X*, sorted by their midpoint value (marked on each bar). The resulting order mirrors the variable effect of crustal differentiation on the behavior of mohometers as shown. Inset diagrams schematically illustrate the different MgO–*X* trends of compatible, incompatible, and neutral parameters.

ΔZr/Y = [0.84, 1.63]), which reflect less crustal control; their Moho depth-dependent variability, which is distinct at the primitive end of the differentiation spectrum, is amplified as MgO decreases. Mohometers based on compatible chemical parameters are characterized by Δ*X* intervals below unity (e.g., ΔCr = [0.02, 1], ΔNi = [0.03, 1], ΔSc = [0.27, 1]) and their pronounced Moho depth-dependent variability observed in primitive compositions decreases with MgO, particularly in the case of parameters involving Cr and Ni. Finally, a series of Moho parameters, including Sr, Sr/Y, Lu/Hf, and MREE/HREE ratios, display narrow Δ*X* intervals near unity. Because MgO variation does not play a significant role in their variability, here they are coined “neutral” in comparison to parameters placed to their left (compatible) and right (incompatible) in Figure 29.

In summary, the majority of composition–crustal thickness correlations at high MgO likely are features inherited from the mantle wedge and reflect differences in its melting regime modulated by the thickness of the overriding plate. The role of intracrustal igneous differentiation processes in shaping the *X*–MgO–*h* surfaces, on the other hand, appears to depend on the geochemical behavior of the involved chemical parameter during magma differentiation: sensitivity to Moho depth variations tends to increase with decreasing MgO in the case of incompatible parameters and decrease in the case of compatible ones. In comparison, the behavior of approximately neutral mohometers does not change significantly across the differentiation spectrum. Any successful petrogenetic model aimed to elucidate that the causes underlying the correlations between chemical parameters and crustal thickness should therefore also factor in the effects of differentiation.

X–MgO–*h* model surfaces and the median data supporting them can be used to evaluate models proposed for various composition–crustal thickness correlations for arcs. For instance, it is broadly accepted that pressure-dependent garnet stability during intracrustal differentiation modulates MREE/HREE ratios, such as Gd/Yb or Dy/Yb, in magmas in arcs with different thicknesses. The reason is that garnet is the only mineral of which elevated HREE contents and affinity for HREE over MREE are thought capable to produce significant increase in Gd/Yb and especially Dy/Yb in a wide compositional range of liquids in equilibrium (e.g., Arth, 1976; Fujimaki et al., 1984; Hauri et al., 1994; Irving & Frey, 1978; Sisson & Bacon, 1992). Accordingly, Gd/Yb and Dy/Yb behave incompatibly during garnet fractionation and thus, both ratios are predicted to increase in magmas with increasing depth of differentiation, which favor residual garnet accumulation. Global arc data and the Gd/Yb–MgO–*h* and Dy/Yb–MgO–*h* models they support are, however, in dissonance with such an interpretation because the variability of Gd/Yb and Dy/Yb with crustal thickness does not appear to be significantly influenced by intracrustal magma differentiation, remaining close to the variability seen in the most primitive melts (Figures 19b, 28, 29, Figure S1). In particular, the very limited increase in Gd/Yb and Dy/Yb across the differentiation spectrum indicates that garnet fractionation in crustal magma reservoirs has no major role in the globally observed covariation of these ratios with arc Moho depths. Instead, the narrow ΔGd/Yb and ΔDy/Yb intervals suggest that much of their variability is inherited from the mantle wedge, where the mean pressure of melting and thereby the proportion of liquids generated in the garnet stability field increase with thickness of the overriding plate (Turner & Langmuir, 2015b).

6. Summary and Perspectives

Global-scale observations made over the past few decades indicate that the chemistry of magmas emplaced at convergent plate margins are influenced by the thickness of crust in which they differentiated and led to the idea that in a similar manner, igneous rocks formed in the geologic past may reflect the thickness of ancient orogens. Reconstructing crustal thickness using the composition of magmatic whole rocks or from detrital zircons originating in such rocks, a method we refer to as *chemical mohometry*, has found numerous applications in paleotectonics and regional geology. Although numerous chemical parameters (elements and their ratios) have been identified to be sensitive to Moho depth variations, the overwhelming majority of these applications directly or indirectly rely on only two whole-rock trace element ratios, La/Yb and Sr/Y, which not always yield coherent estimates. To improve the accuracy and flexibility of chemical mohometry and expand its applicability, we present 41 new whole-rock mohometer models based on major and trace element composition of subalkaline volcanic rocks dominating modern arcs. The newly calibrated parameters account for magma differentiation degree (as quantified by MgO) and use elevation as proxy for Moho depth. They are meant to be employed in combination, depending on their applicability to the available chemical data (a MATLAB® app facilitating the computations is provided). The collection of new parameters we provide here is not exhaustive; other useful mohometers (element ratios in particular) can be calibrated and added to the list in the future, thereby further increasing the accuracy and flexibility of the approach.

The petrogenetic foundation of the composition–crustal thickness correlations used in mohometry is matter of ongoing debate. Based on a quantitative analysis of our models, we show that some of these correlations originate in the sub-arc mantle; the amplitude of additional effects resulting from the intracrustal magma differentiation depends on the geochemical behavior of the parameters, that is, as a general rule, incompatible mohometers become more sensitive, while compatible ones become less sensitive to Moho depth variations as magma MgO decreases. Formulating a quantitative model explaining the globally identified differentiation-dependent composition versus crustal thickness trends will be essential for better understanding arc magma evolution.

Since the new mohometer calibrations do not include data from collisional orogens, their applicability to this tectonic environment is not verified. Estimating crustal thickness in collisional belts requires dedicated La/Yb and Sr/Y mohometers (Hu et al., 2017) because there the parameters previously developed for arcs (J. B. Chapman et al., 2015; Profeta et al., 2015) may not be applicable. Figure 22 indicates that whereas the new Sr/Y calibration may be slightly better than previous arc-based models in recovering Moho depths beneath collisional belts, the new La/Yb parameter will not bring significant improvements. To what extent are other new mohometer formulations applicable to this tectonic environment remains unclear as long as the chemical differences between the subalkaline magmas emplaced in collisional belts and subduction zones are not fully mapped out. Our first tests indicate that the new models reproduce geophysically constrained Moho depths in the Miocene-Pleistocene Călimani–Gurghiu–Harghita collisional magmatism of the East Carpathians in Romania (Vlăsceanu et al., 2021) although even here local misfits result for adakite-like rocks that are not included in the model calibrations. Elsewhere, for example, in Anatolia, our unpublished first estimates are ambiguous. Clearly, further evaluations are needed to decide which, if any, of the newly calibrated mohometers is systematically applicable to collisional orogens or whether different models are needed for this tectonic setting.

We expect the new calibrations to increase the accuracy and resolving power of zircon-based mohometry. Since available zircon-based models (Balica et al., 2020; Tang, Ji, et al., 2021) are modeled on the whole-rock La/Yb parameter, their efficiency is limited by the performance of this parameter and therefore, just like in the case of whole-rock mohometry, a multiparameter approach may be an important step toward improved zircon-based Moho estimates. The new parameters presented in this paper show good performance in felsic rocks in which zircon commonly saturates, involve trace elements that are readily measurable in zircon and are characterized by reasonably well-constrained zircon-melt partition coefficients, and thus offer a promising expansion of the mohometric toolset applicable to this mineral. Because Ti-in-zircon crystallization temperatures are not reliable indicators of the host magma's differentiation degree (Fu et al., 2008), the most promising mohometers applicable in zircon petrochronology are those which are least sensitive to MgO variations (Figure 29): Gd/Yb, Dy/Yb, Sm/Yb, Lu/Hf, Nd/Yb, and Nd/Y. Other parameters, such as La/Yb, La/Y, Nb/Yb, and Nb/Y, are slightly more sensitive to differentiation and thus should yield less accurate but still reasonable crustal thickness estimates, which can be improved by constraining the differentiation degree with the aid of zircon chemistry-based host-rock classification schemes (Belousova et al., 2002). On the other end, Hf, U, and particularly Th/Yb and Th/Y, show pronounced MgO sensitivity and thus, in the absence of accurate constraints on MgO, are not applicable to zircons.

Chemical mohometry has the potential of becoming a powerful tool for reconstructing the topography of ancient orogens. Several approaches are now used for estimating paleoelevation in continental areas, ranging from qualitative to semiquantitative geologic observations (e.g., beach deposits identified in a sedimentary sequence) to paleontological (flora and pollen), to empirical calibrations involving various geologic materials (e.g., abundance and size of vesicles in basalts), and to isotopic constraints. The latter approach primarily focuses on stable isotopes (deuterium and oxygen) and has blossomed over the past two decades (e.g., Huntington & Lechler, 2015; Quade et al., 2013). Despite their successful applications to orogenic evolution (e.g., Ghosh et al., 2006), stable isotope techniques, such as clumped oxygen isotopes on carbonates, are susceptible to post-depositional modifications (Quade et al., 2020) and are sensitive to climate change as much as they are to tectonics (Champagnac et al., 2012). Furthermore, these methods are limited to areas preserving evidence of major uplift in the Cenozoic or latest Mesozoic, such as the Cenozoic Andes, or the evolution of the Tibetan plateau; they are not applicable to Paleozoic and older eroded orogens commonly missing records of (near-)surface processes. Obtaining paleoelevation information from the chemical and isotopic composition of igneous rocks and their zircons is not complicated by inconveniences of the abovementioned methods and thus represents a viable alternative to these. Pioneering studies have demonstrated the potential of the new approach, for example, Zhu et al. (2017) approximated the mean topographic evolution of the Gangdese Mountains in southern Tibet using the La/Yb mohometer of Profeta et al. (2015), and Scott et al. (2018) used Sr and Nd isotopic ratios of Andean arc lavas to estimate the history of surface uplift of the Andean Western Cordillera. The new-generation mohometers primarily calibrated against elevation not only confirm the validity of the approach but also consolidate it with the aid of the proposed multiparameter method as illustrated by the Peninsular Ranges Batholith case study (Figure 27b).

Abbreviations

H (km)	Moho depth relative to sea level
h (km)	Elevation
H^{tot} (km)	Crustal thickness, $H^{\mathrm{tot}} = H + h$
X	Chemical parameter defining a mohometer, for example, CaO, Hf, La/Yb
REM	Reference elevation model, that is, X–MgO–h model surface
$H_{X(i)}$ (km)	Moho depth calculated using median value of X in MgO bin i ($i = 1\ldots9$)
H_X (km)	Median of validated $H_{X(i)}$ values obtained for X
MAD_X (km)	Median absolute deviation associated with H_X
$\varepsilon_{\mathrm{max}}$ (km)	Maximum absolute value of calibration residuals; used to filter $H_{X(i)}$ (arbitrary)
$rmse_{\mathrm{max}}$ (km)	Maximum root mean square error of $\varepsilon_{\mathrm{max}}$; used to filter H_X (arbitrary)
mad_{max} (km)	Maximum MAD_X value; used to filter H_X (arbitrary)
H_M (km)	Median of all $H_{X(i)}$ values obtained with validated mohometers
MAD_M (km)	Median absolute deviation associated with H_M
$X/X_{\mathrm{max.MgO}}(h)$	Value of X along elevation contour line h within the applicability envelope of X–MgO–h, normalized to its value at maximum MgO concentration along h
ΔX	Total variability interval of $X/X_{\mathrm{max.MgO}}(h)$

Data Availability Statement

Supporting Information accompanying the paper are also available at https://osf.io/bmn8y/.

Acknowledgments

The authors are grateful to Robert J. Stern, Chris Hawkesworth, and Allen Glazner for their constructive reviews and Fabio Florindo for editorial handling. The authors thank Scott Paterson for challenging discussions and insightful comments, Katie Ardill and Barbara Ratschbacher for providing paleoarc data for testing purposes, and Emilie Bowman and Sarah George for testing and suggesting improvements to GAME. M. N. Ducea acknowledges support from the U.S. NSF grants EAR1725002 and EAR2020935.

References

Arth, J. G. (1976). Behavior of trace elements during magmatic processes – A summary of theoretical models and their applications. *Journal of Research of the U.S. Geological Survey*, *4*(1), 41–47.

Assumpção, M., Feng, M., Tassara, A., & Julià, J. (2013). Models of crustal thickness for South America from seismic refraction, receiver functions and surface wave tomography. *Tectonophysics*, *609*, 82–96. https://doi.org/10.1016/j.tecto.2012.11.014

Baird, A. K., Baird, K. W., & Welday, E. E. (1979). Batholithic rocks of the northern Peninsular and Transverse Ranges, southern California: Chemical composition and variation. In P. L. Abbott & V. R. Todd (Eds.), *Mesozoic crystalline rocks: Peninsular range batholith and Pegmatites, Point Sal ophiolite* (pp. 111–132). Department of Geological Sciences, San Diego State University.

Balica, C., Ducea, M. N., Gehrels, G. E., Kirk, J., Roban, R. D., Luffi, P., et al. (2020). A zircon petrochronologic view on granitoids and continental evolution. *Earth and Planetary Science Letters*, *531*, 116005. https://doi.org/10.1016/j.epsl.2019.116005

Bassin, C., Laske, G., & Masters, G. (2000). The current limits of resolution for surface wave tomography in North America. *Paper presented at the EOS Trans AGU* (Vol. 81, p. F897).

Beck, S. L., Zandt, G., Myers, S. C., Wallace, T. C., Silver, P. G., & Drake, L. (1996). Crustal-thickness variations in the central Andes. *Geology*, *24*(5), 407–410. https://doi.org/10.1130/0091-7613(1996)024<0407:ctvitc>2.3.co;2

Belousova, E. A., Griffin, W. L., O'Reilly, S. Y., & Fisher, N. I. (2002). Igneous zircon: Trace element composition as an indicator of source rock type. *Contributions to Mineralogy and Petrology*, *143*(5), 602–622. https://doi.org/10.1007/s00410-002-0364-7

Best, M. G., Barr, D. L., Christiansen, E. H., Gromme, S., Deino, A. L., & Tingey, D. G. (2009). The great basin Altiplano during the middle Cenozoic ignimbrite flareup: Insights from volcanic rocks. *International Geology Review*, *51*(7–8), 589–633. https://doi.org/10.1080/00206810902867690

Bowman, E. E., Ducea, M. N., & Triantafyllou, A. (2021). Arclogites in the subarc lower crust: Effects of fractionation, partial melting, and retained melt on the foundering ability of residual roots. *Journal of Petrology*, *65*(12), egab094. https://doi.org/10.1093/petrology/egab094

Burnham, A. D., & Berry, A. J. (2012). An experimental study of trace element partitioning between zircon and melt as a function of oxygen fugacity. *Geochimica et Cosmochimica Acta*, *95*, 196–212. https://doi.org/10.1016/j.gca.2012.07.034

Busby, C. (2004). Continental growth at convergent margins facing large ocean basins: A case study from Mesozoic convergent-margin basins of Baja California, Mexico. *Tectonophysics*, *392*(1), 241–277. https://doi.org/10.1016/j.tecto.2004.04.017

Carrapa, B., DeCelles, P. G., Ducea, M. N., Jepson, G., Osakwe, A., Balgord, E., et al. (2022). Estimates of paleo-crustal thickness at Cerro Aconcagua (Southern Central Andes) from detrital proxy-records: Implications for models of continental arc evolution. *Earth and Planetary Science Letters*, *585*, 117526. https://doi.org/10.1016/j.epsl.2022.117526

Champagnac, J. D., Molnar, P., Sue, C., & Herman, F. (2012). Tectonics, climate, and mountain topography. *Journal of Geophysical Research*, *117*, B02403. https://doi.org/10.1029/2011jb008348

Chapman, A. D., Ducea, M. N., McQuarrie, N., Coble, M., Petrescu, L., & Hoffman, D. (2015). Constraints on plateau architecture and assembly from deep crustal xenoliths, northern Altiplano (SE Peru). *GSA Bulletin*, *127*(11–12), 1777–1797. https://doi.org/10.1130/b31206.1

Chapman, J. B., Ducea, M. N., DeCelles, P. G., & Profeta, L. (2015). Tracking changes in crustal thickness during orogenic evolution with Sr/Y: An example from the North American Cordillera. *Geology*, *43*(10), 919–922. https://doi.org/10.1130/g36996.1

Chapman, J. B., Gehrels, G. E., Ducea, M. N., Giesler, N., & Pullen, A. (2016). A new method for estimating parent rock trace element concentrations from zircon. *Chemical Geology*, *439*, 59–70. https://doi.org/10.1016/j.chemgeo.2016.06.014

Chiaradia, M. (2014). Copper enrichment in arc magmas controlled by overriding plate thickness. *Nature Geoscience*, *7*(1), 43–46. https://doi.org/10.1038/ngeo2028

Chiaradia, M. (2015). Crustal thickness control on Sr/Y signatures of recent arc magmas: An Earth scale perspective. *Scientific Reports*, *5*(1), 1–5. https://doi.org/10.1038/srep08115

Chiaradia, M. (2021). Zinc systematics quantify crustal thickness control on fractionating assemblages of arc magmas. *Scientific Reports*, *11*(1), 1–14. https://doi.org/10.1038/s41598-021-94290-6

Claiborne, L. L., Miller, C. F., Gualda, G. A. R., Carley, T. L., Covey, A. K., Wooden, J. L., & Fleming, M. A. (2018). Zircon as magma monitor. In *Microstructural geochronology* (pp. 1–33).

Cleveland, W. S., & Devlin, S. J. (1988). Locally weighted regression: An approach to regression analysis by local fitting. *Journal of the American Statistical Association*, *83*, 596–610. https://doi.org/10.1080/01621459.1988.10478639

Colpron, M., Gladwin, K., Johnston, S. T., Mortensen, J. K., & Gehrels, G. E. (2005). Geology and juxtaposition history of the Yukon-Tanana, Slide Mountain, and Cassiar terranes in the Glenlyon area of central Yukon. *Canadian Journal of Earth Sciences*, *42*(8), 1431–1448. https://doi.org/10.1139/e05-046

Contreras-Reyes, E., Grevemeyer, I., Watts, A. B., Flueh, E. R., Peirce, C., Moeller, S., & Papenberg, C. (2011). Deep seismic structure of the Tonga subduction zone: Implications for mantle hydration, tectonic erosion, and arc magmatism. *Journal of Geophysical Research*, *116*(B10), B10103. https://doi.org/10.1029/2011JB008434

Coudert, E., Cardwell, R. K., Isacks, B. L., & Chatelain, J.-L. (1984). P-wave velocity of the uppermost mantle and crustal thickness in the central Vanuatu Islands (New Hebrides Island arc). *Bulletin of the Seismological Society of America*, *74*(3), 913–924. https://doi.org/10.1785/BSSA0740030913

Coulon, C., & Thorpe, R. S. (1981). Role of continental-crust in petrogenesis of orogenic volcanic Associations. *Tectonophysics*, *77*(1–2), 79–93. https://doi.org/10.1016/0040-1951(81)90162-1

Delph, J. R., Ward, K. M., Zandt, G., Ducea, M. N., & Beck, S. L. (2017). Imaging a magma plumbing system from MASH zone to magma reservoir. *Earth and Planetary Science Letters*, *457*, 313–324. https://doi.org/10.1016/j.epsl.2016.10.008

DePaolo, D. J. (1981). Trace-element and isotopic effects of combined wallrock assimilation and fractional crystallization. *Earth and Planetary Science Letters*, *53*(2), 189–202. https://doi.org/10.1016/0012-821x(81)90153-9

DePaolo, D. J., Harrison, T. M., Wielicki, M., Zhao, Z., Zhu, D.-C., Zhang, H., & Mo, X. (2019). Geochemical evidence for thin syn-collision crust and major crustal thickening between 45 and 32 Ma at the southern margin of Tibet. *Gondwana Research*, *73*, 123–135. https://doi.org/10.1016/j.gr.2019.03.011

DePaolo, D. J., Perry, F. V., & Baldridge, W. S. (1992). Crustal versus mantle sources of granitic magmas: A two-parameter model based on Nd isotopic studies. *Transactions of the Royal Society of Edinburgh Earth Sciences*, *83*, 439–446. https://doi.org/10.1017/s0263593300008117

Dhuime, B., Wuestefeld, A., & Hawkesworth, C. J. (2015). Emergence of modern continental crust about 3 billion years ago. *Nature Geoscience*, *8*(7), 552–555. https://doi.org/10.1038/ngeo2466

Dickinson, W. R. (1975). Potash-depth (K-H) relations in continental-margin and intra-oceanic magmatic arcs. *Geology*, *3*(2), 53–56. https://doi.org/10.1130/0091-7613(1975)3<53:pkricm>2.0.co;2

Ducea, M. N. (2001). The California arc: Thick granitic batholiths, eclogitic residues, lithospheric-scale thrusting, and magmatic flare-ups. *Geological Society of America Today*, *11*(11), 4–10. https://doi.org/10.1130/1052-5173(2001)011<0004:tcatgb>2.0.co;2

Ducea, M. N., Chapman, A. D., Bowman, E. E., & Triantafyllou, A. (2021). Arclogites and their role in continental evolution; part 1: Background, locations, petrography, geochemistry, chronology and thermobarometry. *Earth-Science Reviews*, *214*, 103375. https://doi.org/10.1016/j.earscirev.2020.103375

Ducea, M. N., Paterson, S. R., & DeCelles, P. G. (2015). High-volume magmatic events in subduction systems. *Elements*, *11*(2), 99–104. https://doi.org/10.2113/gselements.11.2.99

Ducea, M. N., & Saleeby, J. B. (1998). A case for delamination of the deep batholithic crust beneath the Sierra Nevada, California. *International Geology Review*, *40*(1), 78–93. https://doi.org/10.1080/00206819809465199

Ducea, M. N., Saleeby, J. B., & Bergantz, G. (2015). The architecture, chemistry, and evolution of continental magmatic arcs. *Annual Review of Earth and Planetary Sciences*, *43*(1), 299–331. https://doi.org/10.1146/annurev-earth-060614-105049

Dufek, J., & Bergantz, G. W. (2005). Lower crustal magma genesis and preservation: A stochastic framework for the evaluation of basalt-crust interaction. *Journal of Petrology*, *46*(11), 2167–2195. https://doi.org/10.1093/petrology/egi049

Engi, M. (2017). Petrochronology based on REE-minerals: Monazite, allanite, xenotime, apatite. In M. J. Kohn, M. Engi, & P. Lanari (Eds.), *Petrochronology: Methods and Applications* (Vol. 83, pp. 365–418). https://doi.org/10.1515/9783110561890-013

Farner, M. J., & Lee, C.-T. A. (2017). Effects of crustal thickness on magmatic differentiation in subduction zone volcanism: A global study. *Earth and Planetary Science Letters*, *470*, 96–107. https://doi.org/10.1016/j.epsl.2017.04.025

Ferry, J. M., & Watson, E. B. (2007). New thermodynamic models and revised calibrations for the Ti-in-zircon and Zr-in-rutile thermometers. *Contributions to Mineralogy and Petrology*, *154*(4), 429–437. https://doi.org/10.1007/s00410-007-0201-0

Fu, B., Page, F. Z., Cavosie, A. J., Fournelle, J., Kita, N. T., Lackey, J. S., et al. (2008). Ti-in-zircon thermometry: Applications and limitations. *Contributions to Mineralogy and Petrology*, *156*(2), 197–215. https://doi.org/10.1007/s00410-008-0281-5

Fujimaki, H. (1986). Partition coefficients of Hf, Zr, and REE between zircon, apatite, and liquid. *Contributions to Mineralogy and Petrology*, *94*(1), 42–45. https://doi.org/10.1007/BF00371224

Fujimaki, H., Tatsumoto, M., & Aoki, K.-I. (1984). Partition coefficients of Hf, Zr, and REE between phenocrysts and groundmasses. *Journal of Geophysical Research*, *89*(S02), B662–B672. https://doi.org/10.1029/JB089iS02p0B662

Gastil, R. G. (1975). Plutonic zones in Peninsular ranges of southern-California and northern Baja-California. *Geology*, *3*(7), 361–363. https://doi.org/10.1130/0091-7613(1975)3<361:pzitpr>2.0.co;2

Gehrels, G. (2014). Detrital zircon U-Pb geochronology applied to tectonics. In R. Jeanloz (Ed.), *Annual Review of Earth and Planetary Sciences* (Vol. 42, pp. 127–149). https://doi.org/10.1146/annurev-earth-050212-124012

Gehrels, G., Rusmore, M., Woodsworth, G., Crawford, M., Andronicos, C., Hollister, L., et al. (2009). U-Th-Pb geochronology of the Coast Mountains batholith in north-coastal British Columbia: Constraints on age and tectonic evolution. *The Geological Society of America Bulletin*, *121*(9–10), 1341–1361. https://doi.org/10.1130/b26404.1

Ghosh, P., Garzione, C. N., & Eiler, J. M. (2006). Rapid uplift of the Altiplano revealed through C-13-O-18 bonds in paleosol carbonates. *Science*, *311*(5760), 511–515. https://doi.org/10.1126/science.1119365

Girardi, J. D., Patchett, P. J., Ducea, M. N., Gehrels, G. E., Cecil, M. R., Rusmore, M. E., et al. (2012). Elemental and isotopic evidence for granitoid genesis from deep-seated sources in the Coast Mountains Batholith, British Columbia. *Journal of Petrology*, *53*(7), 1505–1536. https://doi.org/10.1093/petrology/egs024

González-Vidal, D., Obermann, A., Tassara, A., Bataille, K., & Lupi, M. (2018). Crustal model of the Southern Central Andes derived from ambient seismic noise Rayleigh-wave tomography. *Tectonophysics*, *744*, 215–226. https://doi.org/10.1016/j.tecto.2018.07.004

Griffin, W. L., & O'Reilly, S. Y. (1987). The composition of the lower crust and the nature of the continental Moho – Xenolith evidence. In P. H. Nixon (Ed.), *Mantle xenoliths* (pp. 413–430). Wiley-Interscience.

Gromet, L. P., & Silver, L. T. (1987). Ree variations across the Peninsular ranges batholith – Implications for batholithic petrogenesis and crustal growth in magmatic arcs. *Journal of Petrology*, *28*(1), 75–125. https://doi.org/10.1093/petrology/28.1.75

Harrison, T. M., Bell, E. A., & Boehnke, P. (2017). Hadean zircon petrochronology. In M. J. Kohn, M. Engi, & P. Lanari (Eds.), *Petrochronology: Methods and Applications* (Vol. 83, pp. 329–364). https://doi.org/10.1515/9783110561890-012

Hauri, E. H., Wagner, T. P., & Grove, T. L. (1994). Experimental and natural partitioning of Th, U, Pb and other trace-elements between garnet, clinopyroxene and basaltic melts. *Chemical Geology*, *117*(1–4), 149–166. https://doi.org/10.1016/0009-2541(94)90126-0

Hickey-Vargas, R., Holbik, S., Tormey, D., Frey, F. A., & Moreno Roa, H. (2016). Basaltic rocks from the Andean Southern Volcanic Zone: Insights from the comparison of along-strike and small-scale geochemical variations and their sources. *Lithos*, *258–259*, 115–132. https://doi.org/10.1016/j.lithos.2016.04.014

Hildreth, W., & Moorbath, S. (1988). Crustal contributions to Arc magmatism in the Andes of central Chile. *Contributions to Mineralogy and Petrology*, *98*(4), 455–489. https://doi.org/10.1007/bf00372365

Hoskin, P. W. O., & Schaltegger, U. (2003). The composition of zircon and igneous and metamorphic petrogenesis. In J. M. Hanchar & P. W. O. Hoskin (Eds.), *Zircon* (Vol. 53, pp. 27–62). https://doi.org/10.1515/9781501509322-005

Hu, F., Ducea, M. N., Liu, S., & Chapman, J. B. (2017). Quantifying crustal thickness in continental collisional belts: Global perspective and a geologic application. *Scientific Reports*, *7*(1), 7058. https://doi.org/10.1038/s41598-017-07849-7

Huntington, K. W., & Lechler, A. R. (2015). Carbonate clumped isotope thermometry in continental tectonics. *Tectonophysics*, *647*, 1–20. https://doi.org/10.1016/j.tecto.2015.02.019

Irvine, T. N., & Baragar, W. R. A. (1971). A guide to chemical classification of common volcanic rocks. *Canadian Journal of Earth Sciences*, *8*(5), 523–548. https://doi.org/10.1139/e71-055

Irving, A. J., & Frey, F. A. (1978). Distribution of trace-elements between garnet megacrysts and host volcanic liquids of kimberlitic to rhyolitic composition. *Geochimica et Cosmochimica Acta*, *42*(Na6), 771–787. https://doi.org/10.1016/0016-7037(78)90092-3

Jagoutz, O. (2014). Arc crustal differentiation mechanisms. *Earth and Planetary Science Letters*, *396*, 267–277. https://doi.org/10.1016/j.epsl.2014.03.060

James, D. E., & Steinhart, J. S. (1966). Structure beneath continents: A critical review of explosion studies 1960-1965. In J. S. Steinhart & T. J. Smith (Eds.), *The Earth Beneath the Continents: A Volume of Geophysical Studies in Honor of Merle A. Tuve* (Vol. 10, pp. 293–333). AGU.

Jull, M., & Kelemen, P. B. (2001). On the conditions for lower crustal convective instability. *Journal of Geophysical Research*, *106*(B4), 6423–6446. https://doi.org/10.1029/2000jb900357

Kay, R. W., & Mahlburg-Kay, S. (1991). Creation and destruction of lower continental crust. *Geologische Rundschau*, *80*(2), 259–278. https://doi.org/10.1007/BF01829365

Keller, C. B., Schoene, B., Barboni, M., Samperton, K. M., & Husson, J. M. (2015). Volcanic-plutonic parity and the differentiation of the continental crust. *Nature*, *523*(7560), 301–307. https://doi.org/10.1038/nature14584

Kidder, S., Ducea, M. N., Gehrels, G., Patchett, P. J., & Vervoort, J. (2003). Tectonic and magmatic development of the Salinian Coast Ridge belt, California. *Tectonics*, *22*(5), 1058. https://doi.org/10.1029/2002tc001409

Kistler, R. W., & Anderson, J. L. (1990). Two different lithosphere types in the Sierra Nevada, California. In *The Nature and Origin of Cordilleran Magmatism* (Vol. 174, pp. 271–282). Geological Society of America. https://doi.org/10.1130/mem174-p271

Kistler, R. W., Wooden, J. L., & Morton, D. M. (2003). *Isotopes and ages in the northern Peninsular Ranges batholith, southern California*. US Geological Survey Open-File Report 03-489 45. https://doi.org/10.3133/ofr03489

Koch, C. D., Delph, J., Beck, S. L., Lynner, C., Ruiz, M., Hernandez, S., et al. (2021). Crustal thickness and magma storage beneath the Ecuadorian arc. *Journal of South American Earth Sciences*, *110*, 103331. https://doi.org/10.1016/j.jsames.2021.103331

Kohn, M. J. (2017). Titanite petrochronology. In M. J. Kohn, M. Engi, & P. Lanari (Eds.), *Petrochronology: Methods and Applications* (Vol. 83, pp. 419–442). https://doi.org/10.1515/9783110561890-014

Kylander-Clark, A. R. C., Hacker, B. R., & Cottle, J. M. (2013). Laser-ablation split-stream ICP petrochronology. *Chemical Geology*, *345*, 99–112. https://doi.org/10.1016/j.chemgeo.2013.02.019

Laske, G., Masters, G., Ma, Z., & Pasyanos, M. (2013). Update on CRUST1.0 – A 1-degree global model of Earth's crust. *Geophysical Research Abstracts*, *15*, EGU2013-2658.

Lee, C.-T. A., Morton, D. M., Kistler, R. W., & Baird, A. K. (2007). Petrology and tectonics of Phanerozoic continent formation: From island arcs to accretion and continental arc magmatism. *Earth and Planetary Science Letters*, *263*(3–4), 370–387. https://doi.org/10.1016/j.epsl.2007.09.025

Lee, C.-T. A., Thurner, S., Paterson, S. R., & Cao, W. (2015). The rise and fall of continental arcs: Interplays between magmatism, uplift, weathering, and climate. *Earth and Planetary Science Letters*, *425*, 105–119. https://doi.org/10.1016/j.epsl.2015.05.045

Leeman, W. P. (1983). The influence of crustal structure on compositions of subduction-related magmas. *Journal of Volcanology and Geothermal Research*, *18*(1–4), 561–588. https://doi.org/10.1016/0377-0273(83)90026-4

Lieu, W. K., & Stern, R. J. (2019). The robustness of Sr/Y and La/Yb as proxies for crust thickness in modern arcs. *Geosphere*, *15*(3), 621–641. https://doi.org/10.1130/ges01667.1

Mahlburg-Kay, S., Godoy, E., & Kurtz, A. (2005). Episodic arc migration, crustal thickening, subduction erosion, and magmatism in the south-central Andes. *GSA Bulletin*, *117*(1–2), 67–88. https://doi.org/10.1130/b25431.1

Mahlburg-Kay, S., & Mpodozis, C. (2001). Central Andean ore deposits linked to evolving shallow subduction systems and thickening crust. *Geological Society of America Today*, *11*, 4–9. https://doi.org/10.1130/1052-5173(2001)011<0004:caodlt>2.0.co;2

Mantle, G. W., & Collins, W. J. (2008). Quantifying crustal thickness variations in evolving orogens: Correlation between arc basalt composition and Moho depth. *Geology*, *36*(1), 87–90. https://doi.org/10.1130/g24095a.1

McGlashan, N., Brown, L., & Kay, S. (2008). Crustal thickness in the central Andes from teleseismically recorded depth phase precursors. *Geophysical Journal International*, *175*(3), 1013–1022. https://doi.org/10.1111/j.1365-246X.2008.03897.x

Miyashiro, A. (1974). Volcanic rock series in island arcs and active continental margins. *American Journal of Science*, *274*(4), 321–355. https://doi.org/10.2475/ajs.274.4.321

Mohorovičić, A. (1910). *Earthquake of 8 October 1909 (Potres od 8. X 1909; Das Beben vom 8. X. 1909.)*. Zagreb.

Mooney, W. D. (2015). 1.11 – Crust and lithospheric structure – Global crustal structure. In G. Schubert (Ed.), *Treatise on geophysics* (2nd ed., pp. 339–390). Elsevier. https://doi.org/10.1016/b978-0-444-53802-4.00010-5

Mooney, W. D., Laske, G., & Masters, T. G. (1998). CRUST 5.1: A global crustal model at 5° x 5°. *Journal of Geophysical Research*, *103*(B1), 727–747. https://doi.org/10.1029/97jb02122

Paterson, S. R., & Ducea, M. N. (2015). Arc magmatic tempos: Gathering the evidence. *Elements*, *11*(2), 91–98. https://doi.org/10.2113/gselements.11.2.91

Paulsen, T., Deering, C., Sliwinski, J., Chatterjee, S., Bachmann, O., & Guillong, M. (2021). Crustal thickness, rift-drift and potential links to key global events. *Terra Nova*, *33*(1), 12–20. https://doi.org/10.1111/ter.12485

Plank, T., & Langmuir, C. H. (1988). An evaluation of the global variations in the major element chemistry of Arc basalts. *Earth and Planetary Science Letters*, *90*(4), 349–370. https://doi.org/10.1016/0012-821x(88)90135-5

Profeta, L., Ducea, M. N., Chapman, J. B., Paterson, S. R., Gonzales, S. M. H., Kirsch, M., et al. (2015). Quantifying crustal thickness over time in magmatic arcs. *Scientific Reports*, *5*, 17786. https://doi.org/10.1038/srep17786

Quade, J., Eiler, J., Daëron, M., & Achyuthan, H. (2013). The clumped isotope geothermometer in soil and paleosol carbonate. *Geochimica et Cosmochimica Acta*, *105*, 92–107. https://doi.org/10.1016/j.gca.2012.11.031

Quade, J., Leary, R., Dettinger, M. P., Orme, D., Krupa, A., DeCelles, P. G., et al. (2020). Resetting Southern Tibet: The serious challenge of obtaining primary records of Paleoaltimetry. *Global and Planetary Change*, *191*, 103194. https://doi.org/10.1016/j.gloplacha.2020.103194

Ryan, W. B. F., Carbotte, S. M., Coplan, J. O., O'Hara, S., Melkonian, A., Arko, R., et al. (2009). Global multi-resolution topography synthesis. *Geochemistry, Geophysics, Geosystems*, *10*(3), Q03014. https://doi.org/10.1029/2008GC002332

Saleeby, J. B., Ducea, M. N., & Clemens-Knott, D. (2003). Production and loss of high-density batholithic root, southern Sierra Nevada, California. *Tectonics*, *22*(6), 1064. https://doi.org/10.1029/2002tc001374

Schaltegger, U., & Davies, J. (2017). Petrochronology of zircon and Baddeleyite in igneous rocks: Reconstructing magmatic processes at high temporal resolution. In M. J. Kohn, M. Engi, & P. Lanari (Eds.), *Petrochronology: Methods and Applications* (Vol. 83, pp. 297–328). https://doi.org/10.1515/9783110561890-011

Scott, E. M., Allen, M. B., Macpherson, C. G., McCaffrey, K. J. W., Davidson, J. P., Saville, C., & Ducea, M. N. (2018). Andean surface uplift constrained by radiogenic isotopes of arc lavas. *Nature Communications*, *9*(1), 1–8. https://doi.org/10.1038/s41467-018-03173-4

Silver, L. T., & Chappell, B. W. (1988). The Peninsular ranges batholith: An insight into the evolution of the Cordilleran batholiths of southwestern North America. *Earth and Environmental Science Transactions of the Royal Society of Edinburgh*, *79*(2–3), 105–121. https://doi.org/10.1017/S0263593300014152

Sisson, T. W., & Bacon, C. R. (1992). Garnet high-silica rhyolite trace-element partition-coefficients measured by ion Microprobe. *Geochimica et Cosmochimica Acta*, *56*(5), 2133–2136. https://doi.org/10.1016/0016-7037(92)90336-h

Stern, R. J. (2002). Subduction zones. *Reviews of Geophysics*, *40*(4), 3–1. https://doi.org/10.1029/2001RG000108

Sundell, K. E., Laskowski, A. K., Kapp, P. A., Ducea, M. N., & Chapman, J. B. (2021). Jurassic to Neogene quantitative crustal thickness estimates in southern Tibet. *Geological Society of America Today*, *31*(6), 4–10. https://doi.org/10.1130/gsatg461a.1

Takahashi, N., Kodaira, S., Klemperer, S. L., Tatsumi, Y., Kaneda, Y., & Suyehiro, K. (2007). Crustal structure and evolution of the Mariana intra-oceanic island arc. *Geology*, *35*(3), 203–206. https://doi.org/10.1130/g23212a.1

Tang, M., Chu, X., Hao, J., & Shen, B. (2021). Orogenic quiescence in Earth's middle age. *Science*, *371*(6530), 728–731. https://doi.org/10.1126/science.abf1876

Tang, M., Ji, W.-Q., Chu, X., Wu, A., & Chen, C. (2021). Reconstructing crustal thickness evolution from europium anomalies in detrital zircons. *Geology*, *49*(1), 76–80. https://doi.org/10.1130/g47745.1

Tassara, A., & Echaurren, A. (2012). Anatomy of the Andean subduction zone: Three-dimensional density model upgraded and compared against global-scale models. *Geophysical Journal International*, *189*(1), 161–168. https://doi.org/10.1111/j.1365-246X.2012.05397.x

Tassara, A., Götze, H.-J., Schmidt, S., & Hackney, R. (2006). Three-dimensional density model of the Nazca plate and the Andean continental margin. *Journal of Geophysical Research*, *111*(B9), B09404. https://doi.org/10.1029/2005jb003976

Taylor, S. R., & McLennan, S. M. (1985). *The continental crust: Its composition and evolution*. Blackwell Scientific Publications.

Todd, V., Erskine, B., Morton, D., & Ernst, W. (1988). Metamorphic and tectonic evolution of the northern Peninsular Ranges batholith, southern California. *Metamorphism and crustal evolution of the western United States, Rubey*, *7*, 894–937.

Todd, V. R., Erskine, B. G., Morton, D. M., & Ernst, W. G. (1988). Metamorphic and tectonic evolution of the northern Peninsular Ranges batholith, southern California. In W. G. Ernst (Ed.), *Metamorphism and Crustal Evolution of the Western United States, Rubey* (Vol. 7, pp. 894–937). Prentice Hall.

Tulloch, A. J., Kimbrough, D. L., Johnson, S. E., Paterson, S. R., Fletcher, J. M., Girty, G. H., et al. (2003). Paired plutonic belts in convergent margins and the development of high Sr/Y magmatism: Peninsular Ranges Batholith of Baja California and Median Batholith of New Zealand. In *Tectonic Evolution of Northwestern Mexico and the Southwestern USA* (Vol. 374). Geological Society of America. https://doi.org/10.1130/0-8137-2374-4.275

Turner, S. J., & Langmuir, C. H. (2015a). The global chemical systematics of arc front stratovolcanoes: Evaluating the role of crustal processes. *Earth and Planetary Science Letters*, *422*, 182–193. https://doi.org/10.1016/j.epsl.2015.03.056

Turner, S. J., & Langmuir, C. H. (2015b). What processes control the chemical compositions of arc front stratovolcanoes? *Geochemistry, Geophysics, Geosystems*, *16*(6), 1865–1893. https://doi.org/10.1002/2014GC005633

Turner, S. J., Langmuir, C. H., Katz, R. F., Dungan, M. A., & Escrig, S. (2016). Parental arc magma compositions dominantly controlled by mantle-wedge thermal structure. *Nature Geoscience*, *9*(10), 772–776. https://doi.org/10.1038/ngeo2788

Vlăsceanu, M., Ducea, M. N., Luffi, P., Bârla, A., & Seghedi, I. (2021). Carpathian-pannonian magmatism database. *Geochemistry, Geophysics, Geosystems*, *22*(9), e2021GC009970. https://doi.org/10.1029/2021GC009970

Walker, B. A., Bergantz, G. W., Otamendi, J. E., Ducea, M. N., & Cristofolini, E. A. (2015). A MASH zone revealed: The mafic complex of the Sierra Valle Fértil. *Journal of Petrology*, *56*(9), 1863–1896. https://doi.org/10.1093/petrology/egv057

Ward, K. M., Delph, J. R., Zandt, G., Beck, S. L., & Ducea, M. N. (2017). Magmatic evolution of a Cordilleran flare-up and its role in the creation of silicic crust. *Scientific Reports*, *7*(1), 9047. https://doi.org/10.1038/s41598-017-09015-5

Watson, E. B. (1980). Some experimentally determined zircon/liquid partition coefficients for the rare Earth elements. *Geochimica et Cosmochimica Acta*, *44*(6), 895–897. https://doi.org/10.1016/0016-7037(80)90270-7

Wetmore, P. H., Herzig, C., Alsleben, H., Sutherland, M., Schmidt, K. L., Schultz, P. W., et al. (2003). Mesozoic tectonic evolution of the Peninsular ranges of southern and Baja California. In *Tectonic Evolution of Northwestern Mexico and the Southwestern USA* (Vol. 374). Geological Society of America. https://doi.org/10.1130/0-8137-2374-4.93

Wieser, P. E., Turner, S. J., Mather, T. A., Pyle, D. M., Savov, I. P., & Orozco, G. (2019). New constraints from Central Chile on the origins of enriched continental compositions in thick-crusted arc magmas. *Geochimica et Cosmochimica Acta*, *267*, 51–74. https://doi.org/10.1016/j.gca.2019.09.008

Yuan, X., Sobolev, S. V., & Kind, R. (2002). Moho topography in the central Andes and its geodynamic implications. *Earth and Planetary Science Letters*, *199*(3–4), 389–402. https://doi.org/10.1016/s0012-821x(02)00589-7

Zhu, D.-C., Wang, Q., Cawood, P. A., Zhao, Z.-D., & Mo, X.-X. (2017). Raising the Gangdese mountains in southern Tibet. *Journal of Geophysical Research: Solid Earth*, *122*(1), 214–223. https://doi.org/10.1002/2016JB013508